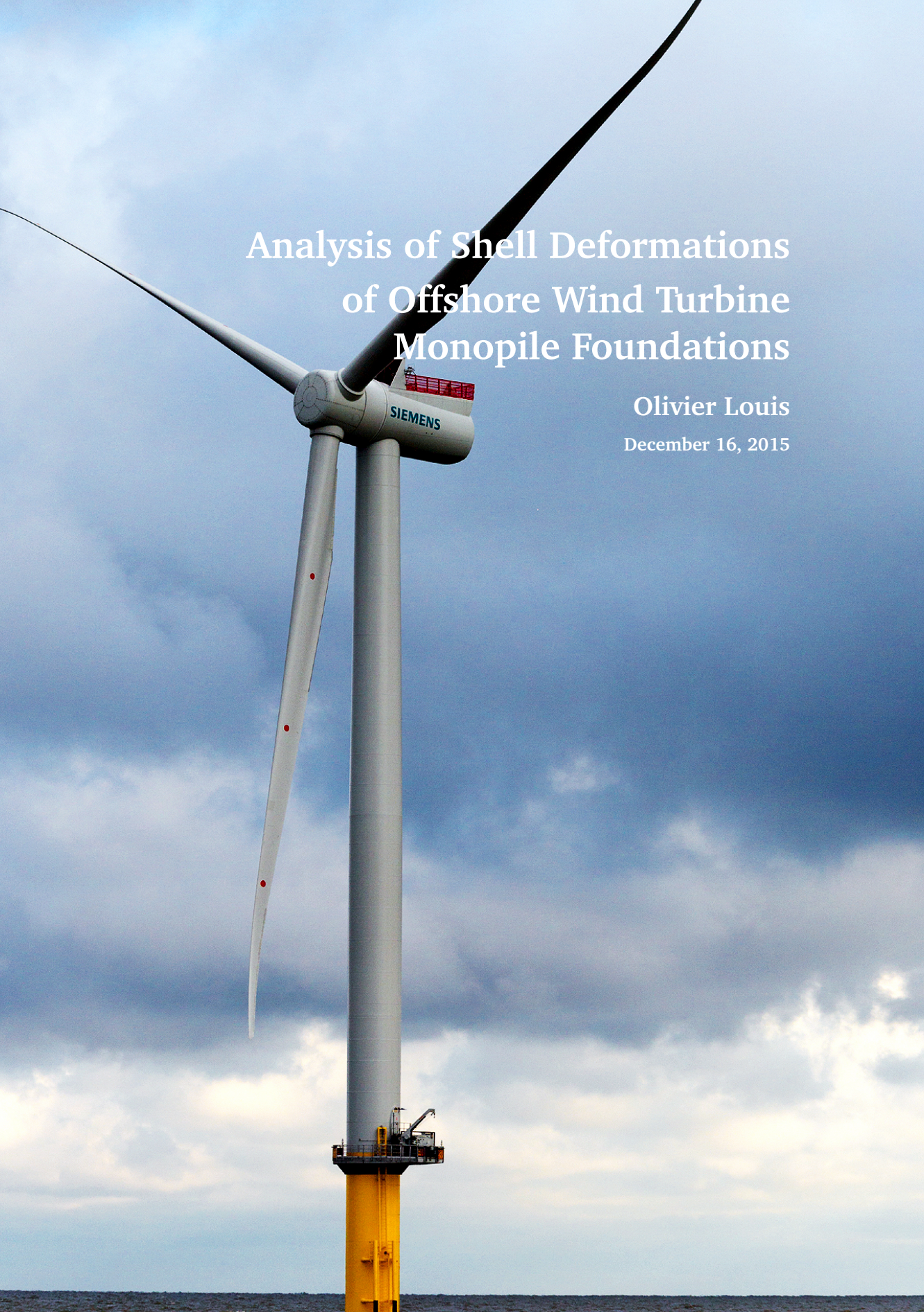

Analysis of Shell Deformations of Offshore Wind Turbine Monopile Foundations

Olivier Louis

December 16, 2015

Analysis of Shell Deformations of Offshore Wind Turbine Monopile Foundations

Master of Science Thesis

Author:	O. Louis	
Committee:	Prof. Dr. A.V. Metrikine	TU Delft - Chairman
	Ir. P. van der Male	TU Delft
	Dr. Ir. P.L.C. van der Valk	Siemens Wind Power
	Ir. W.G. Versteijlen	Siemens Wind Power, TU Delft
	Dr. Ir. K.N. van Dalen	TU Delft
	Ir. J.S. Hoving	TU Delft

December 16, 2015

TU Delft Delft University of Technology

- CONFIDENTIAL -

SIEMENS

Summary

A significant reduction in the levelized cost of electricity is necessary for offshore wind farms to become a competitive energy source. Amongst other methods, overall project cost reduction can be achieved by optimized support structure design. An upcoming trend is the use of 'XL monopiles', which provide a cost effective foundation solution for offshore wind farms in deeper water and are able to support larger turbines.

One of the most governing design criteria for offshore wind turbines is the fatigue limit state. Current practice is to check compliance of a structural design with this criterion by means of a large number of simulations. In these simulations a monopile is typically modelled using beam theory. For the large diameter monopiles, structural design has become less slender and more thin-walled. This implies that, in relation to the global bending deformations, shell deformations will have a more pronounced contribution to the total deformations in the structure as compared to smaller diameter piles. The goal of this study is to investigate if these shell deformations have a significant contribution to the stresses in these large diameter structures, during fatigue limit state design load cases. Beam theory is unable to capture this phenomena and thus a more advanced modelling method is required.

A semi-analytical structural model of a monopile is developed using coupled circular cylindrical shell segments. Soil-structure interaction characteristics are incorporated based on a translation from three dimensional finite element modelling. With a transformation to generalized coordinates it is shown how the structural model can be connected to a model of a wind turbine's tower and rotor nacelle assembly in a manner that allows for computationally effective numerical calculations. Making use of the continuous description of the model, internal stresses at any location in the monopile's shell can be obtained directly from the deformation behaviour. Additionally, following the shell equations, the monopile's shell deformations can be isolated from its global bending behaviour, which allows for a transparent analysis.

The dynamic behaviour of the monopile in various design load cases is analysed using time-domain simulations. These are performed using a state-of-the-art numerical code which accounts for structural-, aero- and controller dynamics. Wave loading is additionally incorporated as a distributed surface loading using diffraction theory. It is found that the shell deformations are sensitive to loading at high frequency bands where typically very little wave energy is present. Assuming Airy waves, as is the standard practice in the offshore industry, only a minor quasi-static contribution of the shell deformations on the monopile's internal stresses is found. The sensitivity to breaking waves, which excite the structure at a wide frequency range, and the sensitivity to the slenderness of the monopile are explored as well. It is found that an increase of the monopile's diameter induces additional shell deformation behaviour.

Acknowledgements

Over the course of almost a year I have had the privilege to envelop myself in this project at Siemens Wind Power. I consider myself very fortunate for the position I was granted and for all the help I received during the way.

First and foremost, I would like to thank my professor Andrei Metrikine for his cooperation and supervision on this project. You encouraged me to look at the physical meaning of all manners involved in this study and provided me with many great and clever insights. This helped me to elevate this work to a higher level.

Second, I would like to show my gratitude towards my team of daily supervisors which consisted of none other than Pim van der Male, Paul van der Valk and Pim Versteijlen. During many hours of discussion, guidance and amazing support, you all helped me to learn so much on a wide variety of subjects during the time I spend on this project. Additionally, you guys helped me to stay, somewhat, on track and focus on an end goal, which can be considered a great achievement.

Fortunately for me, the list does not end here. My appreciation for Michiel van der Meulen for his assistance with SWAG, Anneke de Groot for helping me set up simulations in BHawC and Sven Voormeeren for your involvement in the student projects. Also a shout out to my fellow students and colleagues at Siemens, you helped me with some tough subjects and made this a nice experience for me.

Last, but certainly not least, I would like to thank my friends, family and loved ones. Mom and dad, thank you for your support during, well, my entire life and also for the assistance during the final stages of this work. Thanks to my sister Jolande for all the positiveness and energy you bring me. Eline, I admire your patience during this project and would like to thank you for helping me through this experience. Max, your help towards the end of this study cannot be understated. You have protected the world from the horror that is my grammar and spelling. On a final note, a thank you to all my friends that either directly helped me or indirectly supported me just by being a good friend.

Contents

Summary i

Acknowledgements iii

Nomenclature ix

1 Introduction 1
- 1.1 Background . . . 1
- 1.2 Problem statement . . . 2
- 1.3 Past research . . . 3
- 1.4 Research objective . . . 3
- 1.5 Approach . . . 3
- 1.6 Scope . . . 5
- 1.7 Thesis outline . . . 8

2 Modelling a cylinder with shell and beam theory 11
- 2.1 Introduction . . . 11
- 2.2 Structural relations to model cylinders . . . 12
  - 2.2.1 Timoshenko's theory for beams . . . 12
  - 2.2.2 Flügge's theory for thin circular cylindrical shells . . . 14
- 2.3 Static loading . . . 18
  - 2.3.1 Timoshenko's theory for beams . . . 18
  - 2.3.2 Flügge's theory for circular cylindrical shells . . . 19
  - 2.3.3 Parameter study of a cantilever cylinder subjected to static edge loading . . . 24
- 2.4 Free vibration . . . 29
  - 2.4.1 Introduction . . . 29

2.4.2 Decoupling Timoshenko's beam equations 29
2.4.3 Decoupling Flügge's shell equations 30
2.4.4 Solving for eigenfrequencies and eigenmodes 31
2.4.5 Parameter study of a cantilever cylinder in free vibration . . . 34
2.5 Forced vibration by means of modal expansion 37
2.5.1 Introduction 37
2.5.2 Modal participation factor 37
2.6 Conclusions 40

3 Soil-structure interaction **43**
3.1 Introduction 43
3.2 Derivation of an equivalent elastic spring stiffness 45
3.2.1 Introduction 45
3.2.2 The circumferential wavenumber method 46
3.2.3 The mode shape method 53
3.2.4 Discussion on the circumferential wavenumber method and the mode shape method 56
3.3 Application in the research models: deriving the elastic foundation's characteristics 57
3.3.1 Overview 57
3.3.2 Comparison with the FEM model 58

4 Analysis by superelements **63**
4.1 Introduction 63
4.2 Coupling of continuous shell and beam segments 64
4.3 Model reduction methods for discrete systems 66
4.4 The Craig-Bampton substructuring method 68
4.4.1 Formulation of the reduction basis 68
4.4.2 Assembly of substructures 69
4.5 Application in the research models: modelling the monopile 70
4.5.1 Overview 70
4.5.2 Formulation of the reduction basis 72
4.5.3 Formulation of the reduced system 74

5 Environmental loading **79**
5.1 Theoretical background of wave loading 79
5.1.1 Introduction 79
5.1.2 Harmonic wave components 80
5.1.3 Statistical description of water movements 81

5.1.4 Velocity potential of an undisturbed wave 82
5.1.5 Diffraction theory 83
5.2 Theoretical background of wind action 86
5.3 Application in the research models: Calculating wave and wind loading 87
5.3.1 Calculation of wave loading 87
5.3.2 Applicability of diffraction theory 91
5.3.3 Calculation of wind loading 92

6 Time-domain simulations 95
6.1 Overview of the models, load cases and limitations 95
6.2 Results 98
6.3 Variations to the simulations 105
6.3.1 Variation 1: Monopile with an increased diameter 105
6.3.2 Variation 2: Monopile subjected to breaking waves 108

7 Conclusions and recommendations 111
7.1 Introduction 111
7.2 Conclusions 112
7.3 Recommendations 114

A Translation from the discrete spring stiffness profiles to a distributed elastic foundation 117
A.1 Distributing the discrete forces over a surface 117
A.2 Direct translation from a discrete spring stiffness profile to a distributed elastic foundation 119

B Calculation of matrix products 121

C Eigenfrequencies of the fixed-interface vibration modes 123

D Modal Assurance Criterion for the fixed-interface vibration modes 125

E Addtional results from the time-domain simulations 127

Bibliography 131

Nomenclature

Latin symbols

A	area	m^{-2}
a	radius, induction factor	m
$\boldsymbol{B}$	boundary condition matrix	$-$
$b^{(s)}$	shearing section width	m
$\boldsymbol{C}$	damping matrix	$-$
c	damping coefficient	Nsm^{-1}
$\boldsymbol{D}$	displacement field	m
D	extensional rigidity coefficient, diameter	Nm^{-1}, m
d	depth	m
E	Young's modulus	Nm^{-2}
F	reaction force	N
G	shear modulus	Nm^{-2}
g	gravitational acceleration	ms^{-2}
H	wave height	m
h	wall thickness	m
$\boldsymbol{I}$	interface condition matrix	$-$
I	area moment of inertia	m^4
$\boldsymbol{K}$	stiffness matrix	$-$
K	flexural rigidity coefficient, stiffness operator or coefficient	Nm, Nm^{-1}
k	thickness parameter, stiffness coefficient, wave number	$-$, Nm^{-1}, radm^{-1}
L	length, shell stiffness operator	m, Nm^{-1}

$\boldsymbol{M}$	mass matrix	
M	bending moment, membrane moment	Nm, N
m	axial mode shape number	–
N	membrane force	Nm^{-1}
n	circumferential wave number	–
N_{MP}	nodes on S_{MP}	–
$\boldsymbol{p}$	loading vector	–
$\boldsymbol{q}$	array of degrees of freedom	–
Q	shear force, axially distributed amplitude of surface load	N, Nm^{-2}
q	distributed line or surface load	Nm^{-1}, Nm^{-2},
$\boldsymbol{R}$	boundary condition matrix, reduction basis	–
S	substructure, segment	–
S_{MP}	cylindrical surface	–
S_x	Kirchhoff's transverse membrane force	Nm^{-1}
$S_z^{(s)}$	first moment of area	m^3
t	time	s
T_x	effective membrane shear force, period	Nm^{-1}, s
U	axial deflection amplitude, velocity	m , ms^{-1},
u	axial deflection	m
V	tangential deflection amplitude, shear force	m, N
v	tangential deflection	m
W	lateral deflection amplitude, radial deflection amplitude	m
w	lateral deflection, radial deflection	m
x	axial coordinate	m
z	radial coordinate, lateral coordinate	m

Greek symbols

α	angular rotation, phase angle	rad
ζ	free surface elevation	m
η	modal participation factor	–
θ	circumferential coordinate	rad
κ	shear coefficient	–
λ	axial wave number	–

ν	Poisson's ratio	$-$
ξ	ratio to the critical damping	$-$
ρ	density	kgm^{-3}
σ	stress	Nm^{-2}
τ	frequency coefficient	s
Φ	angular rotational amplitude, velocity potential	rad, $\mathrm{N}^2\mathrm{s}^{-1}$
ϕ	angular rotation, inflow angle	rad
Ω	frequency parameter	$-$
ω	frequency	rads^{-1}

Abbreviations

BHawC	Bonus horizontal axis wind turbine code
BEM	blade element momentum
C-B	Craig-Bampton
CFD	computational fluid dynamics
DLC	design load case
FEM	finite element method
FFT	fast Fourier transform
FLS	fatigue limit state
JONSWAP	joint North Sea wave project
KC	Keulegang Carpenter number
LCOE	levelized cost of electricity
RNA	rotor nacelle assembly
SWAG	Siemens wave generator
ULS	ultimate limit state

Chapter 1

Introduction

1.1 Background

Using the wind as a clean and renewable energy source is becoming increasingly popular. As stated in the energy agreement, the Dutch government aims to generate 14% of all energy from renewable sources in 2020, rising to 16% in 2023. Amongst other sources of renewable energy, offshore wind turbines will act as a contributor towards this goal [1]. A significant reduction in the levelized cost of electricity (LCOE) is necessary for offshore wind farms to become a competitive energy source.[1] A reduction of an offshore wind farm's LCOE can be achieved by increasing its energy yield or lowering its overall project cost. Amongst other methods, a higher energy yield can be obtained by increasing the turbine size and overall project cost reduction can be achieved by optimized support structure design.

The most popular and simple support structure type is the monopile, being often significantly cheaper than jacket, gravity based or floating type solutions. Monopiles were thought to be only feasible on locations with relatively shallow water depth while supporting relatively small turbines. In deeper water and when using larger turbines, the jacket types foundations start to take over as more feasible solutions. An upcoming trend is the use of 'XL monopile' foundations. These large diameter monopiles are expected to be the most cost effective foundation type in up to 40 m of water depth while being able to support 5-8 MW turbines. The monopiles are

[1] The LCOE is a metric which attempts to compare different methods of electricity generation. Here the LCOE is defined as the per-kilowatt hour cost of building and operating a power plant over an assumed life-time.

thus expected to partly take over jacket type support structures which were previously considered economically effective in the range of 25-50 m waterdepth while supporting 2-5 MW turbines [2]. Significant saving potentials on the overall project costs are predicted by the industry using the new large diameter monopile technology [3].

1.2 Problem statement

In the design process of offshore wind turbine support structures, many time domain simulations are required to quantify the lifetime loading on the structure. Current practice is to design offshore monopile foundations using calculations based on beam theories, as beam elements are simple and computationally effective. While beam theories are able to accurately predict the global bending behaviour of slender structures, such as offshore wind turbines with a monopile foundation, they are not able to predict the deformation of the monopile's shell. This may lead to a loss in accuracy in the assessment of soil-structure interaction and the prediction of stresses within the monopile's shell due to environmental loading. In this study the following definitions are adopted: the *global bending deformations* of the monopile are defined as all deformations that displace the vertical centreline of the monopile, while the *shell deformations* of the monopile are defined as deformation of the monopile's shell relative to the monopile's vertical centreline.

With the increased use of large diameter monopiles, structural design has become less slender and more thin-walled. This implies that, when compared to the global bending deformations, the monopile's shell deformations will be more pronounced for the large diameter monopiles. While it is expected that, over the structure's lifetime, the majority of the stress within the monopile's shell will be caused by global bending behaviour, it is currently unknown how much these shell deformations contribute to the fatigue lifetime of large diameter offshore wind turbines.

It can therefore be stated that, for the design process of large diameter monopiles, (i) the application of beam theory needs justification, and (ii) an assessment of the contribution of shell deformation on the predicted fatigue lifetime is to be made. In order to predict the deformation of the monopile's shell using a research model, a description of the environmental loading and boundary conditions along its circumference is to be included. To this end, several practices in the design of offshore wind turbines are no longer sufficient. These are: (i) one-dimensional representation of the wave loading as a vertical line load, and (ii) one-dimensional representation of soil-structure interaction.

1.3 Past research

A superelement study on an offshore wind turbine with a monopile foundation was performed by Engels [4]. A prediction of significant excitation of eigenmodes dominated by shell deformation due to wave loading was made. It was suggested that the predicted excitation of these modes could be caused by the application of wave loads in the numerical model as nodal point loads. Whether the excitation of the shell deformation modes due to wave loading is also physical, was not investigated.

1.4 Research objective

From the problem statement and the previous paragraph on the past research we conclude that there is a need to better understand the role of shell deformation in the analysis of large diameter offshore monopile support structures. This study will specifically focus on the fatigue limit state (FLS), which corresponds to failure of the structure due to cyclic loading. Since the monopile's fatigue lifetime can be directly related to the stress generated in the monopile's shell during its service life, the main research objective is hereby defined as the following.

Gain insight in the contribution of shell deformation on the internal stresses, with respect to the stresses caused by global bending, in a large diameter monopile.

The secondary objective of this study is to propose a method that incorporates the effect of the shell deformation in the assessment of the life-time loading of offshore monopile foundations. For this purpose a structural model of a large diameter monopile is to be developed which: (i) accounts for both global bending and shell deformations, (ii) is computationally effective when assessing the structure's life–time loading, and (iii) takes into account the distribution of the wave loading and the soil reaction forces over the circumference of the monopile.

1.5 Approach

A case study is performed in which the stress caused by global bending deformations and shell deformations in a large diameter monopile are analysed. For this purpose, two structural models of an offshore wind turbine with a large diameter monopile foundation are developed. For several design load cases the two models

will be analysed in the time domain, as is the current practice in the industry. In the first and second model, the structural behaviour of the monopile is described by respectively Timoshenko's theory for beams and Flügge's theory for thin circular cylindrical shells. These models will be referred to as the beam model and the shell model. The beam model will be able to capture the global bending behaviour of the monopile while the shell model will be able to capture both global bending and shell deformations. Insight on the previously stated research objective is then gained by comparison of: (i) the total stress levels in the monopile's shell as predicted by the beam model and the shell model, and (ii) the ratio of stress in the monopile's shell caused by global bending deformations to stress caused by shell deformations, both as predicted by the shell model.

For both models the equations of motion governing the monopile are derived, which are then solved in a semi-analytical way. A semi-analytical solution procedure to the problem is chosen, because it provides insight in the mechanisms that cause the global bending and shell deformation within the monopile support structure. An analytical or semi-analytical method is also preferable for its computational efficiency when compared to alternatives such as the finite element method (FEM), while it additionally provides a continuous solution of the structural response. In order to familiarize ourselves with the governing equations, solution strategies and predicted response of the monopile in both structural models, a parameter study is performed. In the parameter study, the static and dynamic behaviour of cylinders of various dimensions is analysed using both Timoshenko's beam theory and Flügge's shell theory. This study may indicate if a difference in the monopile's predicted global bending behaviour by the two models of the offshore monopile is expected.

Once the relations to describe the structural behaviour of beams and circular cylindrical shells are known, several steps are taken to model a reference case offshore wind turbine. First, soil-structure interaction characteristics are obtained using an available three-dimensional FEM model of a soil. The soil's properties in the FEM model are based on seismic measurements. From this FEM model an equivalent distributed elastic foundation is derived. Secondly, it is shown how, using interface conditions, several analytically described cylinder segments can be coupled to each other. The cylinder segments are used to model the parts of the monopile above the sea level, submerged in water and embedded within the soil. Various segments are used to model the part of the monopile below the mudline. For each segment a unique magnitude of the soil stiffness can be assigned. This procedure allows for the implementation of a non-homogeneous soil-stiffness profile in the models without unnecessary complication of the governing equations. Third, wave action on the monopile is analysed according to diffraction theory. Using Airy's wave theory and the JONSWAP spectrum, the wave action is calculated for several design load cases

based on site specific parameters. Fourth, wind loading on the rotor and the connection of the monopile to the tower is incorporated in this study by coupling of the monopile to Siemens' BHawC using the Craig-Bampton substructuring method. The Craig-Bampton method transforms the monopile into a superelement, located at interface level of the wind turbine, which represents the monopile's dynamic behaviour in the time domain simulations. BHawC, which abbreviates Bonus Horizontal axis wind turbine Code, is an aero-elastic code capable of performing non-linear time domain simulations of the turbine and tower which include controller effects of the turbine. The tower and turbine are modelled within BHawC with Timoshenko beam elements, using the FEM. The shell model is schematically visualized in figure 1.1. For the beam model, the continuous shell segments are replaced by continuous beam segments.

Resulting from the BHawC simulations is a time series of the loading and deformations of the monopile support structure. Since for both the beam and shell model the monopile is described continuous in space, stresses at any location within the monopile's shell can be determined directly from the deformations.

1.6 Scope

To limit the model's complexity and to keep calculation results transparent, several simplifications were made when translating the physical reality to a research model.

- Physically, the environment of an offshore wind turbine is very complex and coupled with the structure through many interaction mechanisms. This study will take into account the structural motion due to the controller and the wave loading in the determination of the wind loads. As generally accepted in practice [5], the direct effect of wind and structural motion will be neglected in the assessment of the wave loading.

- Wave loading is calculated by means of diffraction theory, assuming a linear and harmonic wave field. This implies that the frequency bands governing the vast majority of the wave loading will be significantly lower then the lowest eigenfrequencies corresponding to modes dominated by shell deformation behaviour. It is therefore expected that shell deformation behaviour will mainly be induced quasi-statically. It is possible that breaking waves, which excite the structure at a wide frequency range, will induce additional shell deformation behaviour. This effect is not considered in this study.

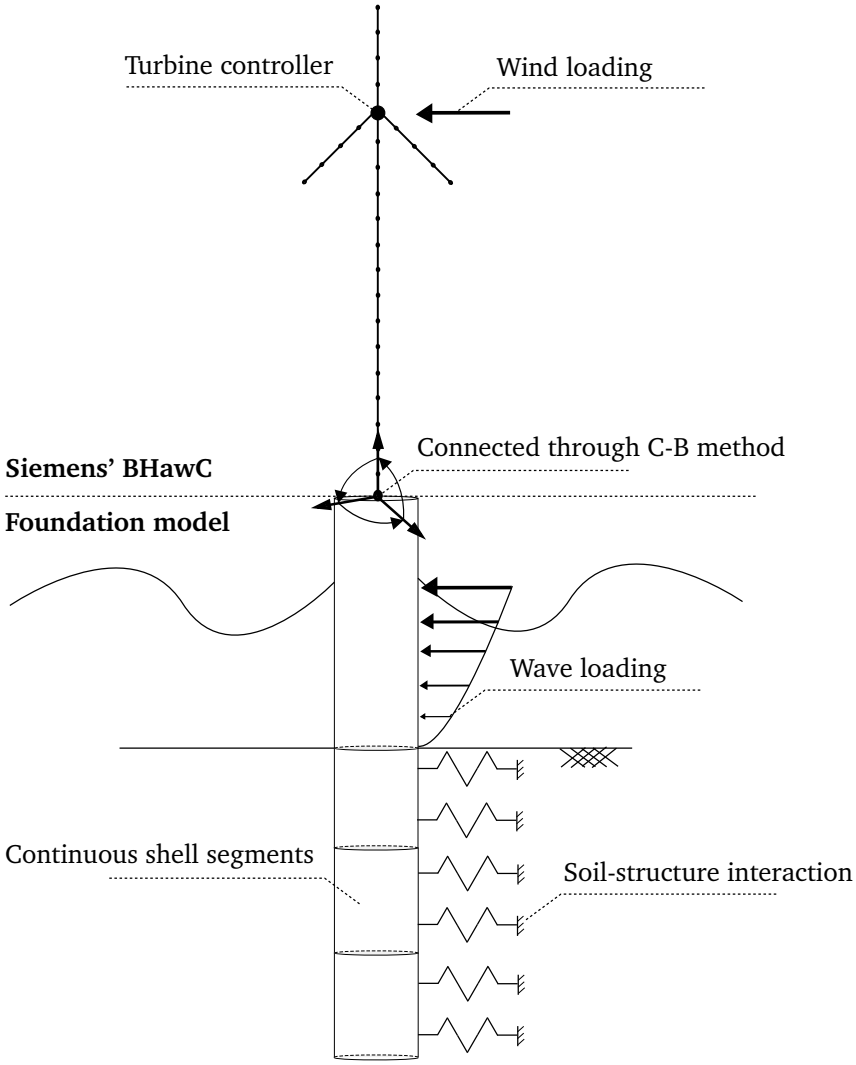

Figure 1.1: Schematic representation of the shell model, as used for the case study.

- The wind loading is assumed to be negligible on all structural parts apart from the rotor plane.

- This study will consider the behaviour of the monopile to be fully linear elastic. Additionally, stresses in the structure will solely be derived with the structure's FLS in mind. While the shell deformations of the monopile are usually associated with ultimate limit state (ULS) buckling strength calculations, buckling is not considered in this work.

- The shell deformations of the monopile are believed to be mainly induced by wave loading and soil-structure interaction. The effect of the wind loading is assumed to be small. With model simplicity in mind, the stiffness of the connection between the tower and the monopile is overestimated and modelled as a rigid-ring connection. Additionally the tower sections are solely modelled using Timoshenko beam elements. These modelling choices effectively eliminate the coupling of the shell deformation between the tower and the monopile.

- An effect different from wave loading that could possibly introduce shell deformation behaviour is the coupling between the structure's modes. In this study perfectly orthogonal eigenmodes are considered, which is not an exact representation of reality.

- Significant simplifications are made to the modelling of the soil stiffness. While the soil behaviour is non-linear, non-local and may experience influence from the ocean's waves, soil stiffness is represented using a set of local and linear distributed springs. The application of linear springs is assumed to be feasible as only small displacements occur within the soil due to the monopile's behaviour. Non-local effects are partly taken into account with the translation from the FEM model by means of the circumferential wavenumber method.

- The distributed springs that represent the soil are able to exert a tension force on the monopile's shell. While the soil has no meaningful physical tensional strength, this can be thought of as an effective tensional strength resulting from a reduction of the static soil pressure on one side of the shell. The static soil pressure works on both sides of the shell and, assuming the monopile to be unplugged, is of the same magnitude on both sides. The static pressure exerted by the soil on the pile is zero at the mudline and increases with penetration depth. Therefore, near the mudline, the effective tensional strength of the soil can be overestimated. Note that also the difference between the active and passive reaction of the soil is neglected in this study.

– In this study the monopile is modelled as a perfect cylinder with no inhomogeneities. This makes the model unfit for the accurate prediction of edge disturbance effects for monopiles with a traditional transition piece and a grouted connection.

1.7 Thesis outline

The outline for the remainder of this thesis follows the approach as described in section 1.5. Chapters 2-5 present all theory used in this study with an additional focus on the implementation in the research models. Chapter 6 covers the simulations with the research models and chapter 7 discusses the conclusions and recommendations derived from this work. A more detailed overview is present below.

Chapter 2	Chapter 2 presents the equations of motion given by Timoshenko's theory for beams and Flügge's theory for thin circular cylindrical shells. Solution procedures for the static and dynamic analysis of cylinders according to both theories are discussed. The predicted global bending behaviour of cylinders according to both theories is analysed.
Chapter 3	In chapter 3 a selected overview of different approaches that can be used to incorporate soil-structure interaction in the research models of the offshore wind turbine is presented. After this, a method to obtain characteristics of an elastic foundation which approximates the reaction forces of the soil on the monopile is discussed. The implementation of the method in the research models is elaborated upon.
Chapter 4	In the fourth chapter coupling of various cylinder segments, using interface conditions, as well as the transformation of the structural models of the monopile into superelements is discussed. An overview of the application of the two strategies in the research models of the monopile is also presented.

Chapter 5	In this chapter the relevant theoretical background of environmental load analysis on offshore wind turbine support structures is provided. Furthermore, the implementation of environmental loading within the case study model is outlined. In this study two types of environmental loads are considered: water wave loads and wind loads.
Chapter 6	Chapter 6 presents an overview of the simulations performed with the research models. The resulting displacements from the simulations are translated to stresses in the monopile's shell, which are then analysed over the entire surface of the monopile.
Chapter 7	The last chapter summarizes the performed study and results. Fulfilment of the research objectives is also discussed. The report closes with recommendations for future research.

Chapter 2

Modelling a cylinder with shell and beam theory

After a short introduction, the equations of motion given by Timoshenko's theory for beams and Flügge's theory for thin circular cylindrical shells are presented. These equations will later be used to describe the structural behaviour of the monopile in the research models. The remainder of this chapter is used to discuss the behaviour of a uniform cylinder, modelled with both beam and shell theory, in three distinct cases. In the first case the cylinder is subjected to static edge loading, while in the second case, a cylinder in free vibration is considered. The theory discussed in the first and second cases will be used to derive the generalized coordinates of the models for the monopile as discussed in section 4.5. Using both shell and beam theory, a parameter is performed which analyses the behaviour of cylinders of various dimensions in the first and second case. The third and last case discussed, is the dynamic analysis of a cylinder by means of modal expansion. This will prove to be similar to the analysis of a monopile by means of the Craig-Bampton substructure method as discussed in section 4.4.

2.1 Introduction

As noted in Chapter 1, the monopile will be modelled using Timoshenko's beam theory and Flügge's theory for circular cylindrical shells. In this chapter the static and dynamic modelling of circular cylinders, according to both theories, is treated. The considered cylinder will be thin-walled and of constant circular cross-section. The

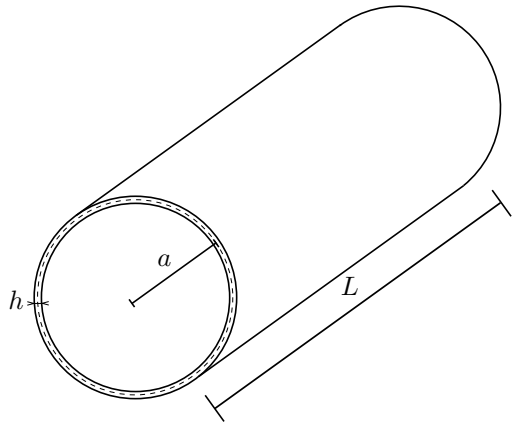

Figure 2.1: Geometry of the thin-walled hollow cylinder

geometry of the cylinder is described by the radius to the middle of the wall surface a, wall thickness h and axial length L. The geometry is depicted in figure 2.1. The cylinder's material is linear elastic, isotropic, homogeneous and is defined with a Young's modulus E, a Poisson's ratio ν and a specific density ρ. This chapter serves two purposes. First, this chapter presents derivations and solution procedures used to develop a more advanced structural model. As will be seen in chapter 4, formulations of the cylinder's response due to static edge loading, eigenmodes and dynamic response to loading in terms of the eigenmodes are used in the Craig-Bampton reduction of the monopile considered in the case study. Second, some differences between the static and dynamic bending behaviour of cylinders modelled with Timoshenko's beam theory and Flügge's theory are studied. The differences in predicted response by the two theories found in this chapter will provide a theoretical basis to understand the differences between shell and beam theory based modelling of offshore wind turbines through more realistic but also more complex modelling.

2.2 Structural relations to model cylinders

2.2.1 Timoshenko's theory for beams

Timoshenko's beam theory can be seen as an extension of the Euler-Bernoulli beam theory that includes a first-order transverse shear effect. The position of the beam is described by two degrees of freedom: a lateral deflection w, measured from the

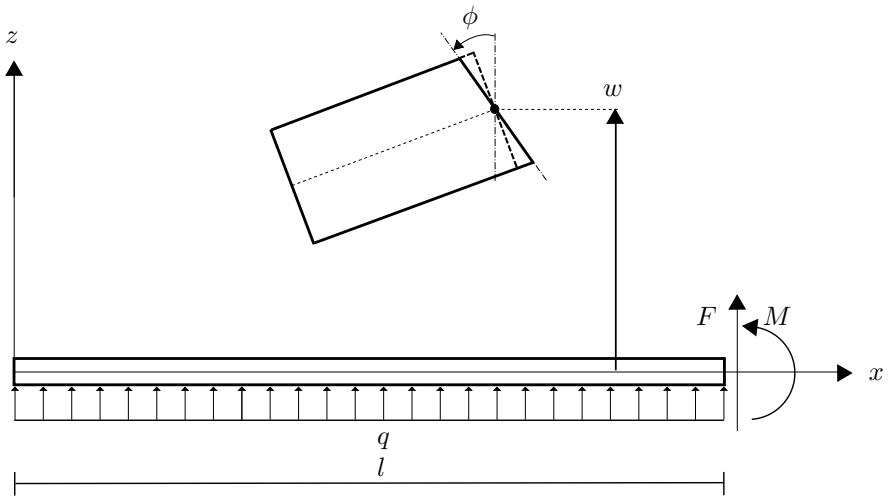

Figure 2.2: A Timoshenko beam in its coordinate system.

beam's centreline, and an angular rotation ϕ of the beam's cross-sectional plane, measured from the normal to the beam's center line. In contrast to the Euler-Bernoulli beam theory, the cross-sectional plane does not remain perpendicular to the beam axis during bending in Timoshenko's beam theory. A shear strain is generated through the additional rotation of the cross-sectional plane. [6, 7, 8]

Governing equations

Consider a beam element as visualized in figure 2.2, the position along the longitudinal direction of the beam is described by the x-coordinate. The beam is subjected to a transverse distributed load q, which works in the positive z direction. The transverse motion w and cross sectional rotation ϕ of such a beam are described by Timoshenko's beam theory with two coupled second-order partial differential equations:

$$\rho A \frac{\partial^2 w}{\partial t^2} + c\frac{\partial w}{\partial t} + \frac{\partial}{\partial x}\left[\kappa AG\left(\frac{\partial w}{\partial x} - \phi\right)\right] = q, \tag{2.1a}$$

$$\rho I \frac{\partial^2 \phi}{\partial t^2} - EI\frac{\partial}{\partial x}\left(\frac{\partial \phi}{\partial x}\right) - \kappa AG\left(\frac{\partial w}{\partial x} - \phi\right) = 0, \tag{2.1b}$$

where c is a damping coefficient and G is the shear modulus of the beam which is given by $G = E/2(1+\nu)$. For a beam with a hollow circular cross section the

cross-sectional area A and area moment of inertia I are given by

$$A = \pi \left(\left(a + \frac{h}{2} \right)^2 - \left(a - \frac{h}{2} \right)^2 \right), \tag{2.2}$$

$$I = \frac{\pi}{4} \left(\left(a + \frac{h}{2} \right)^4 - \left(a - \frac{h}{2} \right)^4 \right). \tag{2.3}$$

For the shear coefficient κ the following formulation can be used [9]

$$\kappa = \frac{6\left(1-\nu\right)\left(1+m_1^2\right)^2}{\left(7+6\nu\right)\left(1+m_1^2\right)^2 + \left(20+12\nu\right)m_1^2}, \tag{2.4}$$

where

$$m_1 = \frac{a+h}{a-h}. \tag{2.5}$$

The bending moment, shear force, axial stress and shear stress in the beam can be determined using

$$M_{xx} = EI\frac{\partial \phi}{\partial x}, \tag{2.6a}$$

$$Q_{xx} = \kappa AG\left(-\phi + \frac{\partial w}{\partial x} \right), \tag{2.6b}$$

$$\sigma_{xx} = \frac{M_{xx} z}{I}, \tag{2.7a}$$

$$\sigma_{x\theta} = \frac{Q_{xx} S_z^{(s)}}{b^{(s)} I}. \tag{2.7b}$$

In the aforementioned equations z is the in-plane distance from the centre of the circular cross section, which equals the cylinder's radius. $S_z^{(s)}$ and $b^{(s)}$ are the first moment of area and the width of the shearing section respectively. In order to solve for $w(x)$ and $\phi(x)$, the definition of four boundary conditions, two at each end of the beam, is necessary.

2.2.2 Flügge's theory for thin circular cylindrical shells

Shells can be seen as plate structures with the additional characteristic of curvature. In literature various theories are presented to describe the behaviour of thin shells. A comprehensive study on the vast amount of different shell theories was performed by

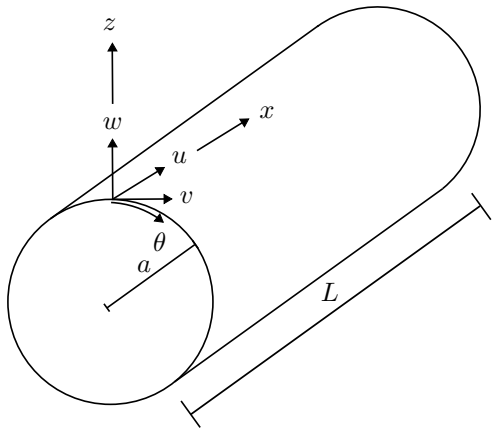

Figure 2.3: A circular cylindrical shell in its coordinate system.

Leissa [10]. It was shown that circular cylindrical shells are often described using an eighth-order system of three coupled partial differential equations, based on Love's first formulations [11]. The governing equations have three degrees of freedom: the axial displacement u, the circumferential displacement v and the radial displacement w. These degrees of freedom are a function of a longitudinal coordinate x and a circumferential coordinate θ. A circular cylindrical shell in its coordinate system can be observed in figure 2.3. It was found that various circular cylindrical shell theories can be described using the equations of Donnell-Mushtari supplemented with a unique contribution which is multiplied by a constant k. The dimensionless thickness parameter k is given by

$$k = \frac{h^2}{12a^2}. \tag{2.8}$$

While the various theories fundamentally have many things in common, a single set of equations has not been agreed upon in literature. In this thesis, the linear relations published by Flügge [12] for thin circular cylindrical shell are used. The equations are also known as Flügge-Byrne-Lur'ye in literature.

Governing equations

In terms of displacements the equilibrium of a circular cylindrical shell is in general described by a system of three coupled partial differential equations is the form of

$$\rho h\frac{\partial^2 u}{\partial t^2}+c_1\frac{\partial u}{\partial t}-L_1\{u,v,w\}=q_x, \tag{2.9a}$$

$$\rho h\frac{\partial^2 v}{\partial t^2}+c_2\frac{\partial v}{\partial t}-L_2\{u,v,w\}=q_\theta, \tag{2.9b}$$

$$\rho h\frac{\partial^2 w}{\partial t^2}+c_3\frac{\partial w}{\partial t}-L_3\{u,v,w\}=q_z, \tag{2.9c}$$

where for i=1, 2 and 3, c_i denotes the damping coefficient in a given direction and

$$L_i\{u,v,w\}=L_{i1}u+L_{i2}v+L_{i3}w. \tag{2.10}$$

L_{i1}, L_{i2} and L_{i3} are partial differential operators with respect to x and θ. In Flügge's shell theory the partial differential operators are defined by the following.

$$L_{11}=\frac{D}{a^2}\left[a^2\frac{\partial^2}{\partial x^2}+(1+k)\frac{1-\nu}{2}\frac{\partial^2}{\partial\theta^2}\right] \tag{2.11a}$$

$$L_{12}=-L_{21}=\frac{D}{a^2}\left[\frac{1+\nu}{2}a\frac{\partial^2}{\partial x\partial\theta}\right] \tag{2.11b}$$

$$L_{13}=L_{31}=\frac{D}{a^2}\left[\nu a\frac{\partial}{\partial x}+k\left(-a^3\frac{\partial^3}{\partial x^3}+\frac{1-\nu}{2}a\frac{\partial^3}{\partial x\partial\theta^2}\right)\right] \tag{2.11c}$$

$$L_{22}=\frac{D}{a^2}\left[(1+3k)\frac{1-\nu}{2}a^2\frac{\partial^2}{\partial x^2}+\frac{\partial^2}{\partial\theta^2}\right] \tag{2.11d}$$

$$L_{23}=L_{32}=\frac{D}{a^2}\left[-k\frac{3-\nu}{2}a\frac{\partial^3}{\partial x^2\partial\theta}+\frac{\partial}{\partial\theta}\right] \tag{2.11e}$$

$$L_{33}=-\frac{D}{a^2}\left[1+k\nabla^4+k\left(1+2\frac{\partial^2}{\partial\theta^2}\right)\right] \tag{2.11f}$$

In the equations above, the following notation was used: $\nabla^2=a^2\frac{\partial^2}{\partial x^2}+\frac{\partial^2}{\partial\theta^2}$, $\nabla^4=\nabla^2\nabla^2=a^4\frac{\partial^4}{\partial x^4}+a^2\frac{\partial^4}{\partial x^2\partial\theta^2}+\frac{\partial^4}{\partial\theta^4}$, $D=\frac{Eh}{1-\nu^2}$. Internal membrane forces and moments

in the shell wall are related to the displacement by the following relations.

$$N_{xx} = \frac{D}{a}\left(a\frac{\partial u}{\partial x} + \nu\frac{\partial v}{\partial \theta} + \nu w\right) - \frac{K}{a}\frac{\partial^2 w}{\partial x^2} \tag{2.12a}$$

$$N_{\theta\theta} = \frac{D}{a}\left(\frac{\partial v}{\partial \theta} + w + \nu a\frac{\partial u}{\partial x}\right) + \frac{K}{a^3}\left(w + \frac{\partial^2 w}{\partial \theta^2}\right) \tag{2.12b}$$

$$N_{\theta x} = \frac{D}{a}\frac{1-\nu}{2}\left(\frac{\partial u}{\partial \theta} + a\frac{\partial v}{\partial x}\right) + \frac{K}{a^3}\frac{1-\nu}{2}\left(\frac{\partial u}{\partial \theta} + a\frac{\partial^2 w}{\partial x \partial \theta}\right) \tag{2.12c}$$

$$N_{x\theta} = \frac{D}{a}\frac{1-\nu}{2}\left(\frac{\partial u}{\partial \theta} + a\frac{\partial v}{\partial x}\right) + \frac{K}{a^3}\frac{1-\nu}{2}\left(a\frac{\partial v}{\partial x} - a\frac{\partial^2 w}{\partial x \partial \theta}\right) \tag{2.12d}$$

$$M_{xx} = \frac{K}{a^2}\left(a^2\frac{\partial^2 w}{\partial x^2} + \nu\frac{\partial^2 w}{\partial \theta^2} - a\frac{\partial u}{\partial x} - \nu\frac{\partial v}{\partial \theta}\right) \tag{2.12e}$$

$$M_{\theta\theta} = \frac{K}{a^2}\left(w + \frac{\partial^2 w}{\partial \theta^2} + \nu a^2\frac{\partial^2 w}{\partial x^2}\right) \tag{2.12f}$$

$$M_{\theta x} = \frac{K}{a^2}(1-\nu)\left(a\frac{\partial^2 w}{\partial x \partial \theta} + \frac{1}{2}\frac{\partial u}{\theta} - \frac{1}{2}a\frac{\partial v}{\partial x}\right) \tag{2.12g}$$

$$M_{x\theta} = \frac{K}{a^2}(1-\nu)\left(a\frac{\partial^2 w}{\partial x \partial \theta} - a\frac{\partial v}{\partial x}\right) \tag{2.12h}$$

In these equations $K = \frac{Eh^3}{12(1-\nu^2)}$. The membrane forces and moments acting on a section of a circular cylindrical shell are visualized in figure 2.4. Normal and shear stresses can be obtained using relations valid for thin plates:

$$\sigma_{xx} = \frac{N_{xx}}{h} \pm z\frac{12M_{xx}}{h^3}, \tag{2.13a}$$

$$\sigma_{\theta\theta} = \frac{N_{\theta\theta}}{h} \pm z\frac{12M_{\theta\theta}}{h^3}, \tag{2.13b}$$

$$\sigma_{x\theta} = \frac{N_{x\theta}}{h} \pm z\frac{12M_{x\theta}}{h^3}, \tag{2.13c}$$

where z denotes the distance from the centreline of the shell wall. Solving the shell problem requires the formulation of eight boundary conditions, four at each end of the shell.

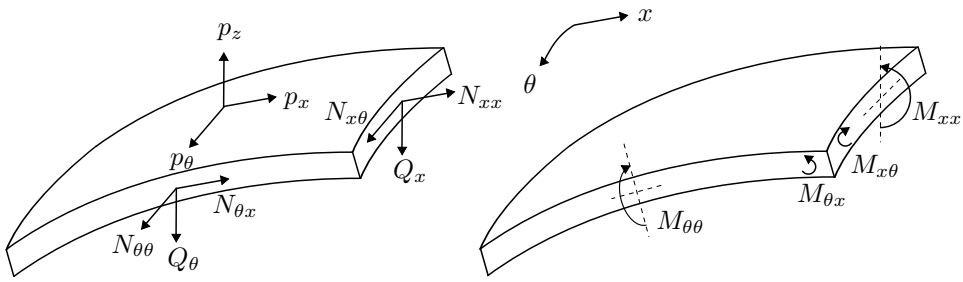

Figure 2.4: Membrane forces, shear forces, surface loading and membrane moments acting on a shell segment.

2.3 Static loading

In this section the modelling of cylinders with Timoshenko's beam theory and Flügge's theory for circular cylindrical shells will be discussed. First a solution procedure for both theories will be presented. It is shown that in order to find an analytical solution to the shell problem, the interface load can be decomposed as a Fourier series of harmonic functions along the cylinder's circumference. Off all the terms in the Fourier decomposition of the loading, only one term will cause a bending response of the shell. At the end of this section a parameter study is performed that compares the bending behaviour of a shell and beam cylinder of various dimensions.

2.3.1 Timoshenko's theory for beams

A Timoshenko beam subjected solely to static loading is described by equations 2.1a - 2.1b while taking all time derivatives with respect to time equal to zero. The governing relations can now be written as ordinary differential equations with respect to x.

$$-\frac{d}{dx}\left[\kappa AG\left(\frac{dw}{dx}-\phi\right)\right] = q \tag{2.14a}$$

$$-EI\frac{d}{dx}\left(\frac{d\phi}{dx}\right) - \kappa AG\left(\frac{dw}{dx}-\phi\right) = 0 \tag{2.14b}$$

After some substitution the rotation and lateral displacement of the beam can be solved from

$$\frac{d^3\phi}{dx^3} = \frac{q}{EI}, \tag{2.15a}$$

$$\frac{dw}{dx} = \phi - \frac{EI}{\kappa AG}\frac{d^2\phi}{dx^2}. \tag{2.15b}$$

The solutions for w and ϕ yield a total of four unique integration constants which can be determined using boundary conditions. The unknown integration constants can be solved from

$$\boldsymbol{R}\boldsymbol{c} = 0 \tag{2.16}$$

where $\boldsymbol{c}$ is a vector containing the unknown integration constants and $\boldsymbol{R}$ is a matrix containing the boundary condition relations. When only loading at the edges of the beam is considered, the external distributed loading term q in equations 2.14a - 2.15b is omitted. The loading on the edges can enter through the boundary condition relations.

2.3.2 Flügge's theory for circular cylindrical shells

When considering a circular cylindrical shell subjected to static loading, the governing relations follow from equations 2.9a - 2.9c while omitting all time-dependence.

$$-L_1\{u, v, w\} = q_x \tag{2.17a}$$

$$-L_2\{u, v, w\} = q_\theta \tag{2.17b}$$

$$-L_3\{u, v, w\} = q_z \tag{2.17c}$$

In equations 2.17a - 2.17c the displacements are a function of both x and θ. In order to simplify the set of partial differential equations, the loading on the shell surface q_x, q_θ and q_z and the displacements u, v and w are each expressed as Fourier series of harmonic functions which are symmetric with respect to the axis $\theta = 0$.

$$q_x(x, \theta) = \sum_{n=0}^{\infty} Q_{xn}(x)\cos(n\theta) \tag{2.18a}$$

$$q_\theta(x, \theta) = \sum_{n=0}^{\infty} Q_{\theta n}(x)\sin(n\theta) \tag{2.18b}$$

$$q_z(x, \theta) = \sum_{n=0}^{\infty} Q_{zn}(x)\cos(n\theta) \tag{2.18c}$$

$$u(x,\theta) = \sum_{n=0}^{\infty} U_n(x)\cos(n\theta) \tag{2.19a}$$

$$v(x,\theta) = \sum_{n=0}^{\infty} V_n(x)\sin(n\theta) \tag{2.19b}$$

$$w(x,\theta) = \sum_{n=0}^{\infty} W_n(x)\cos(n\theta) \tag{2.19c}$$

The application can be extended to asymmetric loading using a combination of trigonometric series.

The total response of the shell is now expressed in terms of various circumferential deformation mode shapes, which are visualized in figures 2.5a - 2.5f. Each circumferential deformation mode can be analysed individually. Three different types of circumferential deformation shapes are distinguished [13]. The axis symmetric mode indicated by $n = 0$ describes behaviour which is constant along the circumferential direction. The response of the shell in tangential direction is decoupled from the response in axial and radial direction. This mode describes expansion in the radial and axial direction of the shell, as well as torsion. The mode noted with $n = 1$ is commonly referred to as the beam mode. This mode caries the bending response of the shell due to the resultant lateral load, similar to beam theory. The rotation of the cross-section due to the resultant overturning moment is accounted for. Unlike beam theory, the three shell displacements u, v and w can describe cross-sectional ovalisation, which occurs when the solution for $W(x)$ differs from the solution for $V(x)$. Another difference with respect to beam theory is that the solution for the $n = 1$ mode contains an edge disturbance which mainly originates from constrains to the cross-sectional deformation. The self-balancing modes are indicated with $n > 1$. The response of a ring to circumferential loading distributed with $n > 1$ is fully described by the deformation of the circular shape, the center point will not be displaced. For an unconstrained cylinder the circumferential response will be the same as for a ring with the same circular profile. In this case only the membrane forces, moments and transverse shear forces in the circumferential direction will occur. If displacement constraints are enforced along a circular edge, membrane forces and moments in the axial direction are induced.

With the formulation of the circumferential deformation shapes, the governing differential equations for the circular cylindrical shell under static loading can be significantly simplified into a set of ordinary differential equations with respect to x for each circumferential wavenumber n. This is done by substitution of equations 2.19a

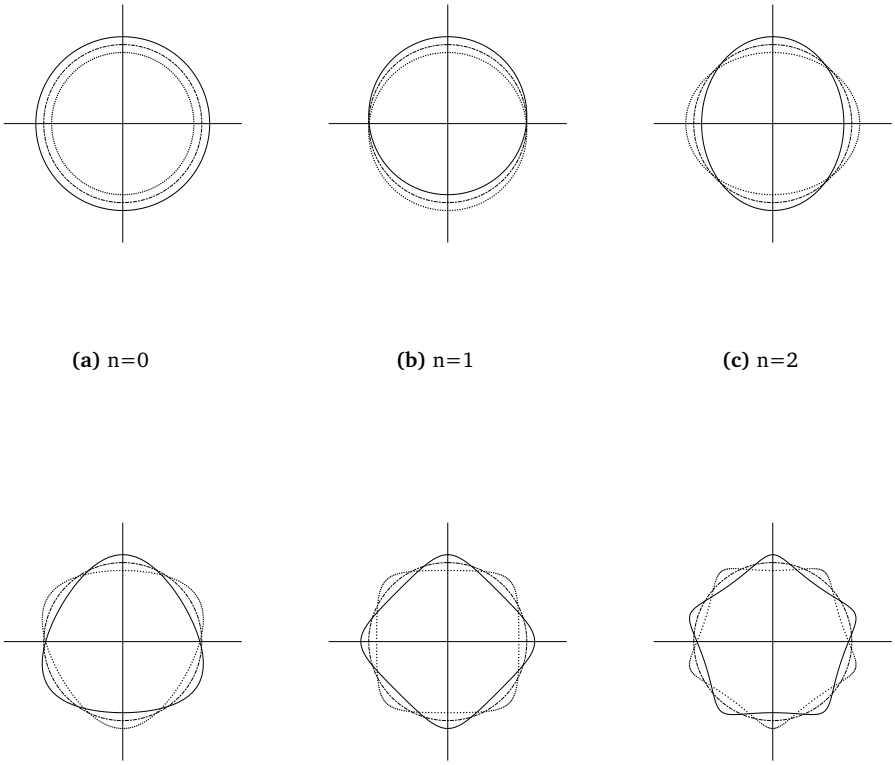

(a) n=0 **(b)** n=1 **(c)** n=2

(d) n=3 **(e)** n=4 **(f)** n=5

Figure 2.5: Circumferential deformation shapes of circular cylindrical shells.

- 2.19c and 2.18a - 2.18c into equations 2.17a - 2.17c. The resulting equations will have a common factor of $\cos(n\theta)$ or $\sin(n\theta)$, which may be dropped from the equations. The total solution for the axial displacement distributions U_n, V_n and W_n can be taken as the summation of the homogeneous and the particular solution to the differential equations. Since in this section only the response of a cylinder to loading at the edges is considered, the external loading on the shell surface is put to zero. Therefore, only the homogeneous solution remains. The homogeneous solution can be taken in the form of

$$U_n(x) = Ae^{\lambda\frac{x}{a}}, \tag{2.20a}$$

$$V_n(x) = Be^{\lambda\frac{x}{a}}, \tag{2.20b}$$

$$W_n(x) = Ce^{\lambda\frac{x}{a}}. \tag{2.20c}$$

Substitution of equations 2.20a - 2.20c allows the transformation of the ordinary differential equations into a set of three linear equations which can, for the homogeneous case, be written as

$$\begin{bmatrix} \hat{L}_{11} & \hat{L}_{12} & \hat{L}_{13} \\ \hat{L}_{21} & \hat{L}_{22} & \hat{L}_{23} \\ \hat{L}_{31} & \hat{L}_{32} & \hat{L}_{33} \end{bmatrix} \begin{bmatrix} A \\ B \\ C \end{bmatrix} = \begin{bmatrix} 0 \\ 0 \\ 0 \end{bmatrix}, \tag{2.21}$$

using

$$\hat{L}_{11} = \lambda^2 - \frac{1-\nu}{2}n^2(1+k), \tag{2.22a}$$

$$\hat{L}_{12} = -\hat{L}'_{21} = \frac{1+\nu}{2}\lambda n, \tag{2.22b}$$

$$\hat{L}'_{13} = -\hat{L}'_{31} = \nu\lambda - k\left(\lambda^3 + \frac{1-\nu}{2}\lambda n^2\right), \tag{2.22c}$$

$$\hat{L}'_{22} = -n^2 + \lambda^2(1+3k)\frac{1-v}{2} \tag{2.22d}$$

$$\hat{L}'_{23} = \hat{L}'_{32} = -n + \frac{3-\nu}{2}k\lambda^2 n, \tag{2.22e}$$

$$\hat{L}'_{33} = -1 - k\left(\lambda^4 - 2\lambda^2 n^2 + n^4 - 2n^2 + 1\right). \tag{2.22f}$$

These homogeneous equations have a unique solution for A, B and C if the determinant of their coefficients is set to zero. The expansion of the determinant will lead to an equation in λ which is known as the characteristic equation. The characteristic equation is of the eighth order in λ and will therefore yield eight roots. The total

solution for u_n, v_n and w_n is taken as

$$u_n(x) = \sum_{j=1}^{8} A_{nj} e^{\lambda_{nj} \frac{x}{a}} \cos(n\theta), \tag{2.23a}$$

$$v_n(x) = \sum_{j=1}^{8} B_{nj} e^{\lambda_{nj} \frac{x}{a}} \sin(n\theta), \tag{2.23b}$$

$$w_n(x) = \sum_{j=1}^{8} C_{nj} e^{\lambda_{nj} \frac{x}{a}} \cos(\theta). \tag{2.23c}$$

The coefficients A_{nj}, B_{nj} and C_{nj} can be related to each other through the linear relations given by equation 2.21. Since the determinant of the system was set to zero, any two of the three relations may be used for this purpose. Substitution of the corresponding value for λ_{nj} into equation 2.21 allows the coefficients to be expressed as

$$A_{nj} = \alpha_{nj} C_{nj} \quad \text{and} \quad B_{nj} = \beta_{nj} C_{nj}. \tag{2.24}$$

Note that for the circumferential wavenumbers of zero and one, some roots of the characteristic equation will be zero. Therefore a polynomial term will also arise in the equations of u, v and w, taking the place of one or more exponential terms. Remaining is the determination of the eight unknown integration constants C_{nj} for each circumferential wavenumber n. These are obtained by introducing boundary conditions. The eight unknown integration constants can then be solved from

$$\boldsymbol{R}\boldsymbol{c} = 0, \tag{2.25}$$

where $\boldsymbol{c}$ is a vector containing the unknown integration constants and $\boldsymbol{R}$ is a matrix containing the boundary condition relations. External forces on the edges of the shell can be included in the boundary condition relations. Once the integration constants are calculated for each circumferential wavenumber, the total response of the shell is known.

While not shown in this section, the structural response of a circular cylindrical shell to distributed loading on the cylinder's surface can only be calculated analytically for certain cases. Using Flügge's shell theory, only the case where the circumferential wavenumber is equal to one or zero can be analysed analytically due to a uniform or linearly distributed surface load. For any higher circumferential wavenumber this is not possible as the general solution will not have enough free constants to adapt to both the surface loading and the boundary constraints. Alternatively, a cylinder due to static distributed loading with a constant or linear distri-

bution in the axial direction can be analysed directly using Morley's theory [13], for all circumferential wavenumbers.

2.3.3 Parameter study of a cantilever cylinder subjected to static edge loading

In this section a parameter study is presented which compares the behaviour of cantilever cylinders modelled with Flügge's shell theory and Timoshenko's beam theory. The comparison is made for a cylinder subjected to a lateral static load and an overturning static moment, which are analysed separately. In the analyses, the lateral displacement of the cylinders centre point and the rotation of the cross-sectional plane are calculated at the free end. For the aforementioned structural reactions, the ratio between the shell and beam solutions are calculated as a function of the length over diameter ratio, L/D and the diameter over wall thickness ratio, D/h. For the shell calculations two types of boundary conditions at the free end are considered. The first type is a rigid ring, the second type is a completely free end.

For the calculations in this section a poison's ratio of 0.3 $[-]$ and a Young's modulus of $210 \cdot 10^9$[Nm^{-2}] are used. Our considered cylinder will be clamped at $x = 0$ and is free at $x = L$. For calculations with the shell model in combination with the completely free end boundary condition, the circumferential distribution of the force has to be specified. The lateral force can be represented with a radial or a tangential load with a circumferential wavenumber of $n = 1$, a tangential load was chosen in this section. The overturning moment is represented as an axial load, also with a circumferential wavenumber of $n = 1$.

For the Timoshenko beam model, the following boundary conditions are defined

$$\begin{cases} w = 0 & \text{at } x = 0 \\ \phi = 0 & \text{at } x = 0 \\ M = M^{(L)} & \text{at } x = L \\ V = V^{(L)} & \text{at } x = L, \end{cases}$$

where $M^{(L)}$ and $V^{(L)}$ are chosen depending on the load case, which is explained below. For the shell model without the rigid ring at $x = L$, the boundary conditions

are defined as

$$\begin{cases} u = 0 & \text{at } x = 0 \\ v = 0 & \text{at } x = 0 \\ w = 0 & \text{at } x = 0 \\ \phi = 0 & \text{at } x = 0 \\ M_{xx} = 0 & \text{at } x = L \\ N_{xx} = P_{1x}^{(L)} & \text{at } x = L \\ T_x = P_{1\theta}^{(L)} & \text{at } x = L \\ S_x = 0 & \text{at } x = L, \end{cases}$$

where T_x is the effective membrane shear force given by

$$T_x = N_{x\theta} - \frac{M_{x\theta}}{a} \tag{2.26}$$

and S_x is Kirchhoff's transverse shear force, which is related to the transverse force Q_x by

$$S_x = Q_x + \frac{\partial}{\partial\theta}\frac{M_{x\theta}}{a}, \quad Q_x = \frac{1}{a}\left(\frac{\partial}{\partial x}M_{xx} + \frac{\partial}{\partial\theta}M_{x\theta}\right). \tag{2.27}$$

$P_{1x}^{(L)}$ and $P_{1\theta}^{(L)} = 1/\pi$ are again dependant on the load case. For the shell model with the rigid ring stiffener at $x = L$ the last four boundary conditions are replaced with the following.

$$\begin{cases} v + w = 0 & \text{at } x = L \\ \phi + \dfrac{u}{a} = 0 & \text{at } x = L \\ aN_{xx} - M_{xx} = M^{(L)} & \text{at } x = L \\ S_x + T_x = V^{(L)} & \text{at } x = L \end{cases}$$

Four cases are considered. In these cases the cylinder will be subjected to

1. only a lateral load and will have a completely free end in the shell model. The load is distributed with a pure tangential load.

2. only a lateral load and will have a rigid ring stiffener at $x = L$ in the shell model.

3. only an overturning moment and will have a completely free end in the shell model. The moment is distrusted as a pure axial load.

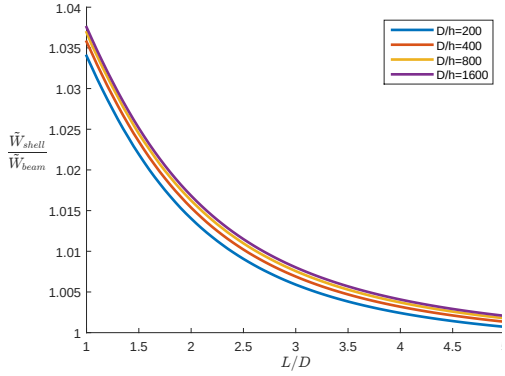

(a) Displacement ratio due to lateral loading

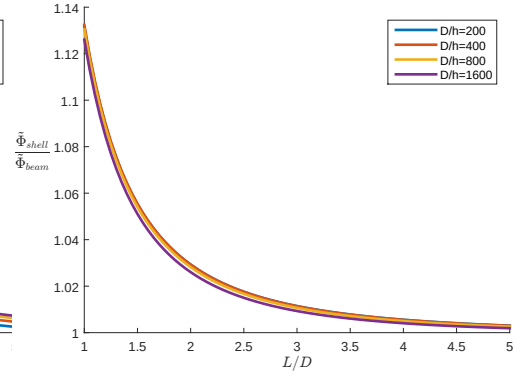

(b) Rotation ratio due to lateral loading

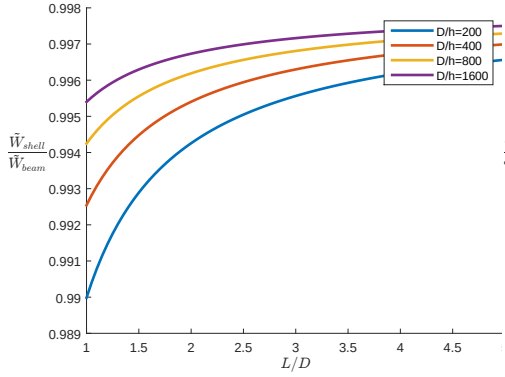

(c) Displacement ratio due to an overturning moment

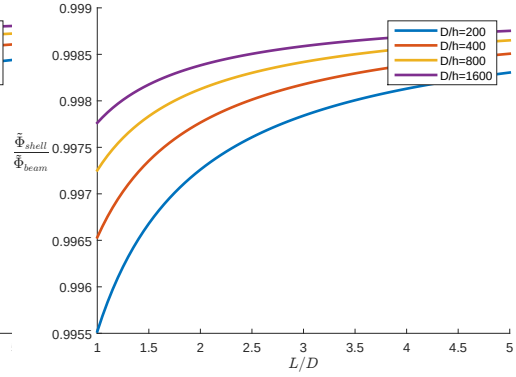

(d) Rotation ratio due to an overturning moment

Figure 2.6: Displacement and rotation ratios for various values of L/D and D/h for a clamped-free cylinder at the free end, loaded with either a lateral load or an overturning moment at the free end.

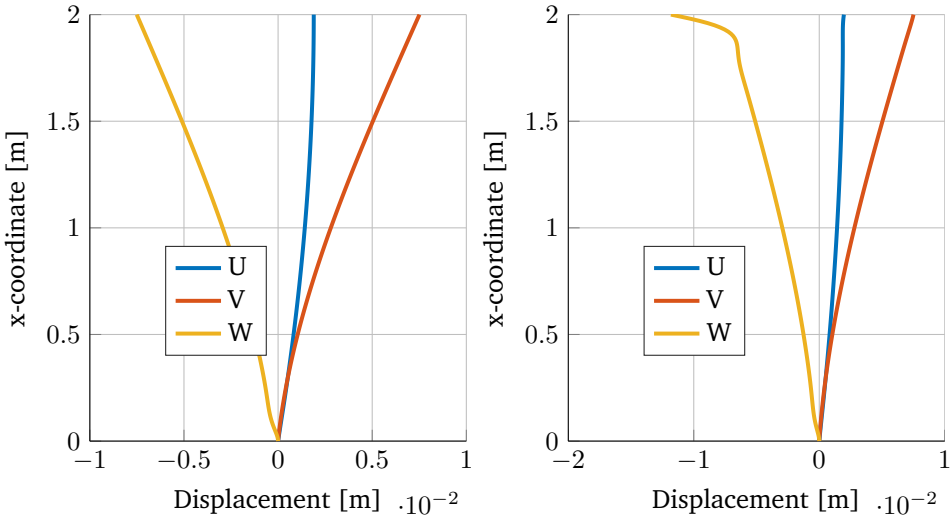

Figure 2.7: In the left figure, the static response of a circular cylinder subjected to a tangential load at the upper edge is shown. In the right figure, the same cylinder is considered, now due to a radial load at the upper edge.

4. only an overturning moment and will have a rigid ring stiffener at $x = L$ in the shell model.

The effective lateral load used in beam theory is related to the circumferential load distribution used with shells by the following relation

$$V = 2a \int_0^{\pi} P_{1\theta} \sin^2(\theta) + P_{1z} \cos^2(\theta) \mathrm{d}\theta. \tag{2.28}$$

Where V is the effective lateral load, $P_{1\theta}$ and P_{1z} are the tangential and radial load amplitudes respectively for $n = 1$. The resulting overturning moment $M^{(L)}$ is related to the axial load distribution P_x in a similar manner. The ratio's for the clamped-free cylinder can be observed in figure 2.6. Analyses of a shell with rigid ring boundary condition yield similar results as shown in figure 2.6. It can be observed that the ratio between the shell and the beam solution approaches 1 for increasing slenderness of the cylinder. For very low values of L/D the predicted responses by Timoshenko's theory start to deviate from Flügge's theory, where the later one is considered to be more accurate. This deviation could be caused by various mechanisms, possibly related to edge disturbance in the shell problem or the shear coefficient κ for the beam problem. For the remainder of this study, these deviations are considered not important and are therefore not discussed further.

In the calculation presented above involving a lateral edge load and the free boundary condition for the shell cylinder, the lateral load was chosen with tangential distribution. This was done as a radial load distribution which will induce a disturbance near the free edge. In figure 2.7 the response of a circular cylinder with $L/D = 2$ and $D/h = 100$ due to a radially and tangentially distributed edge load is shown. The total lateral load is the same in both calculations. An edge disturbance at the free end due to the radial edge load is observed. Note that in both figure's also an edge disturbance near the clamped end can be observed in the radial response of the shell. Edge disturbances in shell structures is a well known phenomena. The axial length of the edge disturbance region solely depends on properties of the cross section of the cylinder. For increasing slenderness of the cylinder the edge disturbance region will become smaller relative to the cylinder's axial length.

2.4 Free vibration

2.4.1 Introduction

In this section a method to analyse cylinders with general boundary conditions in free vibration according to shell and beam theory are presented. It is shown how undamped eigenfrequencies and eigenmodes can be determined. This is done by assuming synchronous motion at a natural frequency, which allows us to separate time from the equations of motion and reduce the problem to a set of ordinary differential equations. Note that this would only hold for an undamped system. For shells also the dependence on the circumferential coordinate is separated from the equations. Resulting is a set of equations from which the remaining unknowns, the axial distributions for the displacements, can be solved in general form. Using boundary constraints the undamped eigenfrequencies and eigenmodes can be solved. A parameter comparison is performed of the first and second natural frequency, as calculated with beam and shell theory, of cantilever cylinders with various L/D and D/h. As is shown in chapter 4, undamped eigenmodes can be used to express the internal degrees of freedom of a structure using a Craig-Bampton reduction.

2.4.2 Decoupling Timoshenko's beam equations

The dynamic, homogeneous and undamped Timoshenko beam equations are given by

$$\rho A \frac{\partial^2 w(x,t)}{\partial t^2} - \frac{\partial}{\partial x}\left[\kappa A G \left(\frac{\partial w(x,t)}{\partial x} - \phi(x,t)\right)\right] = 0, \tag{2.29a}$$

$$\rho I \frac{\partial^2 \phi(x,t)}{\partial t^2} - EI \frac{\partial}{\partial x}\left(\frac{\partial \phi(x,t)}{\partial x}\right) - \kappa A G \left(\frac{\partial w(x,t)}{\partial x} - \phi(x,t)\right) = 0. \tag{2.29b}$$

In order to separate time from the equations, the following solution is attempted:

$$\phi(x,t) = \Phi(x)\eta(t), \tag{2.30a}$$

$$w(x,t) = W(x)\eta(t). \tag{2.30b}$$

For this it can be shown, see for example reference [14], that the solution for the time dependant part $\eta(t)$ can be expressed as a complex exponent multiplied with a unknown constant $\hat{\eta}$ in the form of

$$\eta(t) = \hat{\eta} e^{i\omega t} \tag{2.31}$$

Substitution of equations 2.30a - 2.30b and 2.31 into equations 2.29a - 2.29b, while omitting the harmonic time-dependant exponent in all terms and dividing by $\hat{\eta}$, gives a set of ordinary differential equations.

$$-\omega^2 \rho A W(x) - \frac{d}{dx}\left[\kappa A G\left(\frac{dW(x)}{dx} - \phi(x,t)\right)\right] = 0 \tag{2.32a}$$

$$-\omega^2 \rho I \Phi(x) - EI\frac{d}{dx}\left(\frac{d\Phi(x)}{dx}\right) - \kappa A G\left(\frac{dW(x)}{dx} - \Phi(x)\right) = 0 \tag{2.32b}$$

2.4.3 Decoupling Flügge's shell equations

The dynamic shell equations for the homogeneous case and while omitting damping can, according to Flügge, be written as

$$\rho h \frac{\partial^2 u}{\partial t^2} - L_1\{u,v,w\} = 0, \tag{2.33a}$$

$$\rho h \frac{\partial^2 v}{\partial t^2} - L_2\{u,v,w\} = 0, \tag{2.33b}$$

$$\rho h \frac{\partial^2 w}{\partial t^2} - L_3\{u,v,w\} = 0. \tag{2.33c}$$

Here L_1, L_2 and L_3 are still defined by equations 2.10 and 2.11a - 2.11f. Similar as for the Timoshenko beam equations, the assumption of synchronous motion also holds when searching for eigensolutions. Furthermore, judging from equations 2.33a - 2.33c, the time dependant function must be harmonic. Since boundary conditions of a cantilever cylinder are to be described along the circumference of the cylinder, the spatial functions can also be split up. This is done in the same way as presented in the static analysis in section 2.3.2. Summarizing, we can write the solution to equations 2.33a - 2.33c in the following form:

$$u_{mn}(x,\theta,t) = U_{mn}(x)\cos(n\theta)e^{\Omega_{mn}t/\tau}, \tag{2.34a}$$

$$v_{mn}(x,\theta,t) = V_{mn}(x)\sin(n\theta)e^{\Omega_{mn}t/\tau}, \tag{2.34b}$$

$$w_{mn}(x,\theta,t) = W_{mn}(x)\cos(n\theta)e^{\Omega_{mn}t/\tau}, \tag{2.34c}$$

where the dimensionless frequency parameter is introduced for convenience as $\Omega_{mn} = \omega_{mn}\tau$ where ω_{mn} is the natural frequency for the combination of circumferential mode n and axial mode m. Furthermore, $\tau = \sqrt{(1-\nu^2)\,\rho a^2/E}$. Substitution of

equations 2.34a - 2.34c into 2.33 and omitting the time and circumferential dependant functions leaves us with a set of ordinary differential equations with respect to the axial displacement distributions $U_{mn}(x)$, $V_{mn}(x)$ and $W_{mn}(x)$.

2.4.4 Solving for eigenfrequencies and eigenmodes

Deriving the characteristic equation In order to derive the characteristic equations of both the beam and shell equations, the form of the solution for the axial displacement distributions has to be assumed. For the shell equations the same form is assumed as in section 2.3.2. For the Timoshenko beam equations a similar form is taken:

$$W(x) = Be^{\lambda x/a}, \tag{2.35a}$$

$$\Phi(x) = Ce^{\lambda x/a}. \tag{2.35b}$$

This allows for the transformation of the ordinary differential equations into linear algebraic equations. For the Timoshenko beam these equations are given by

$$\begin{bmatrix} -\omega^2\rho A - \kappa AG\lambda^2 & \kappa AG \\ -\kappa AG & -\omega^2\rho I - EI\lambda^2 + \kappa AG \end{bmatrix} \begin{bmatrix} B \\ C \end{bmatrix} = \begin{bmatrix} 0 \\ 0 \end{bmatrix} \tag{2.36}$$

For Flügge's shell theory the equations are given by 2.21, while adding the inertia terms to the diagonal. Thus, in equation 2.21 the coefficients are still given by 2.22a - 2.22f, with the exception of the diagonal terms, which are now defined as:

$$L'_{11} = \Omega^2 + \lambda^2 - \frac{1-\nu}{2}n^2(1+k), \tag{2.37a}$$

$$L'_{22} = \Omega^2 - \frac{1-\nu}{2}\lambda^2 + n^2 - \frac{3}{2}(1-\nu)\,k\lambda^2, \tag{2.37b}$$

$$L'_{33} = \Omega^2 + 1 + k\left(\lambda^4 - 2\lambda^2 n^2 + n^4 - 2n^2 + 1\right). \tag{2.37c}$$

Or in a more general form, the systems resulting from both theories are now described by

$$\boldsymbol{C}\hat{\boldsymbol{u}} = 0, \tag{2.38}$$

where the vector $\hat{u}$ contains the coefficients B and C in the case of Timoshenko's beam theory, and the coefficients A, B and C in case of Flügge's shell theory. For the non-trivial solution of the set of algebraic equations the determinant of the matrix $\boldsymbol{C}$ must equal zero.

$$\left|\boldsymbol{C}\right| = 0 \tag{2.39}$$

Expansion of the determinant yields the characteristic equation. For the Timoshenko beam theory the eigenmodes are now given by

$$w_m(x,t) = \sum_{j=1}^{4} B_{mj} e^{\lambda_{mj}\frac{x}{a}} e^{i\omega_m t} \tag{2.40a}$$

$$\phi_m(x,t) = \sum_{j=1}^{4} \alpha_{mj} B_{mj} e^{\lambda_{mj}\frac{x}{a}} e^{i\omega_m t} \tag{2.40b}$$

and for Flügge's shell theory the following formulations are used.

$$u_{mn}(x,\theta,t) = \sum_{j=1}^{8} \alpha_{mnj} C_{mnj} e^{\lambda_{mnj}\frac{x}{a}} \cos(n\theta) e^{i\Omega_{mn} t} \tag{2.41a}$$

$$v_{mn}(x,\theta,t) = \sum_{j=1}^{8} \beta_{mnj} C_{mnj} e^{\lambda_{mnj}\frac{x}{a}} \sin(n\theta) e^{i\Omega_{mn} t} \tag{2.41b}$$

$$w_{mn}(x,\theta,t) = \sum_{j=1}^{8} C_{mnj} e^{\lambda_{mnj}\frac{x}{a}} \cos(n\theta) e^{i\Omega_{mn} t} \tag{2.41c}$$

In equations 2.40a - 2.41c subscripts m and n denote the axial and circumferential mode number respectively. The values for λ_m are given as the mth roots to the characteristic equation for the Timoshenko beam. Similarly, the values for λ_{mn} are obtained through the characteristic equation for the shell using a circumferential wavenumber of n. Additionally, for all combination's of n, m and j the coefficients α_{mj}, α_{mnj} and β_{mnj} can be determined by substitution of the values for λ_{mnj} or λ_{mj} in equation 2.38, similar as presented in section 2.3.2. Note that all these coefficients, as well as λ_{mj} and λ_{mn} will now be a function of frequency.

Solving for the eigenfrequencies To find non-trivial solutions for the integration constants, the determinant of the boundary condition matrix $\boldsymbol{R}$ of the homogeneous system must equal zero.

$$\left|\boldsymbol{R}\right| = 0 \tag{2.42}$$

Equation 2.42 is used to determine the natural frequencies of the system. The expansion of equation 2.42 will lead to a complex equation. Therefore its roots can be obtained by analysing when the absolute value of this equation, as a function of frequency, approaches zero. Most conveniently this is done numerically, especially

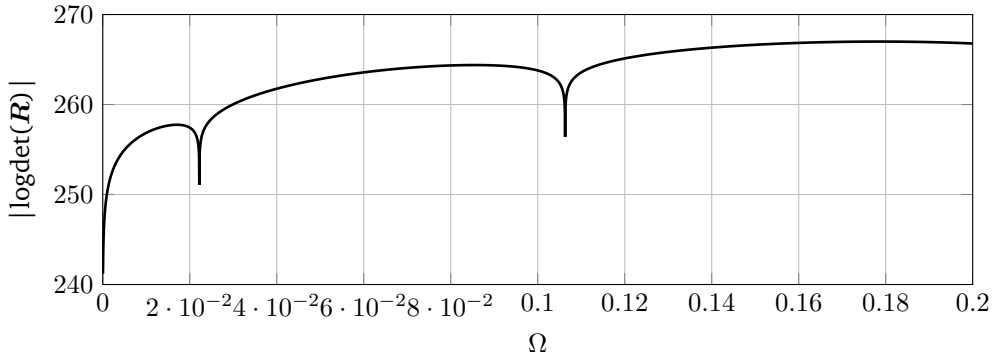

Figure 2.8: Example calculation of the log-determinant of the boundary condition matrix for the shell problem versus the frequency parameter.

for the equations governing the shell problem. An example of the determinant of the boundary condition matrix for a shell problem as a function of the dimensionless frequency parameter Ω is presented in figure 2.8. Note that in the figure the determinant never actually reaches zero, this is explainable by the sensitivity to small increases in $\Delta\Omega$ used in the numerical calculation. The minimum points in figure 2.8 are to be interpreted as natural frequencies of the cylinder [15]. Alternatively, the real and imaginary parts of the determinant can also be investigated separately.

Solution for the mode shapes When the natural frequencies of the cylinder are known, all parameters within the boundary condition matrix are determined. Equation 2.42 can now be used to determine the integration constants c_j. However, since the determinant of the boundary condition matrix is set to zero, the boundary condition matrix is singular. Due to this singularity $J-1$ out of J integration constants can be solved. To accomplish this, one of the integration constants must be assigned a convenient arbitrary value. Any one of the coefficients can be chosen. Once one integration constant has been assigned a convenient value, a finite number of $J-1$ by $J-1$ matrices can be constructed. The remaining integration constants can be calculated from these matrices and are proportional to the arbitrary chosen value [16]. In the case that the determinant truly equals zero, an arbitrary construction can be chosen. If the determinant is close to zero, it is advisable that calculations of the mode shapes resulting from several $J-1$ by $J-1$ matrices are compared with each other in order to verify the correctness of the calculations. Once the integration constants are calculated the mode shapes are obtained. Using the described method, the

solutions for the mode shapes may be complex valued. In order to obtain real-valued displacements, the solutions are multiplied by a complex rotation mapping $e^{\alpha\sqrt{-1}}$, where α is determined to rotate the displacements through the complex plane onto the real axis [17].

2.4.5 Parameter study of a cantilever cylinder in free vibration

Similar to section 2.3.3 a parameter study is presented which compares cantilever cylinders modelled with Flügge's shell theory and Timoshenko's beam theory. This comparison is made for cylinders in free vibration. The cylinder's first and second dimensionless eigenfrequencies for the beam modes are calculated using both theories. The shell equations of circumferential wavenumber $n = 1$ are thus considered. The comparison has once again been done for various L/D ratio's. h/D has been chosen equal to $1/100$, which is a realistic value for the wall thickness to diameter ratio of an offshore monopile foundation. The same material properties were used as in section 2.3.3. Furthermore, the shell has a free end boundary at $x = L$. Comparisons for the first eigenfrequency can be observed in figures 2.9 and 2.10 while the comparisons for the second eigenfrequency can be observed in figure 2.11 and 2.12. It is concluded that Timoshenko's beam theory and Flügge's shell theory show good agreement on the prediction of eigenfrequencies of the investigated cylinders. For comparative purposes, the prediction of the eigenfrequencies according to Euler-Bernoulli's beam theory has also been concluded. These predictions show a notable mismatch with both Flügge's theory and Timoshenko's theory, especially for low values of L/D.

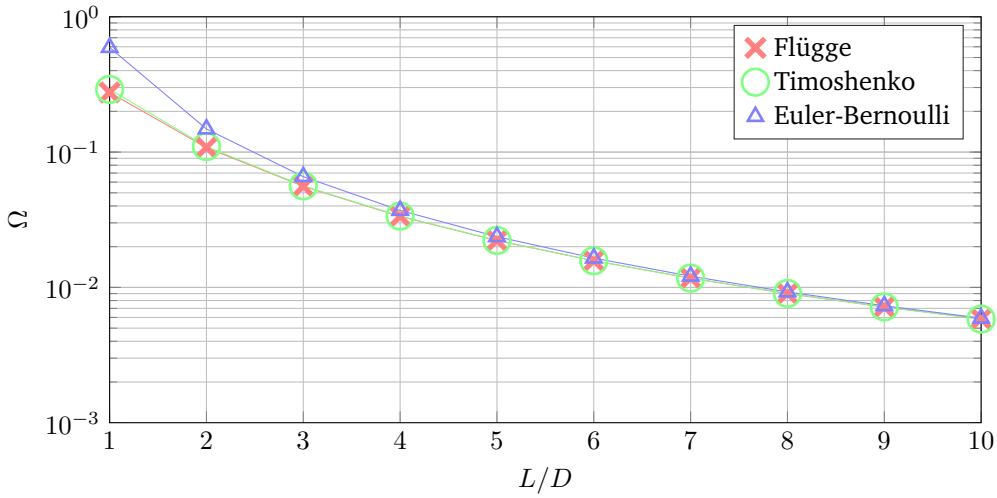

Figure 2.9: Comparison of the first dimensionless eigenfrequency of a cantilever cylinder with $h/D = 100$ according to Flügge's theory, Timoshenko's theory and Euler-Bernoulli's theory.

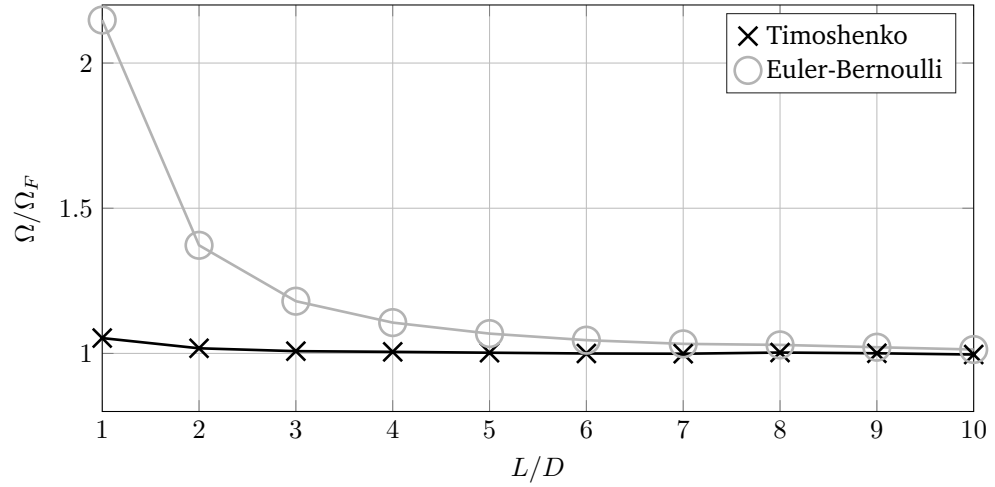

Figure 2.10: Ratio of Timoshenko's and Euler-Bernoulli's prediction to Flügge's prediction of a cantilever cylinder's first eigenfrequency with $h/D = 100$.

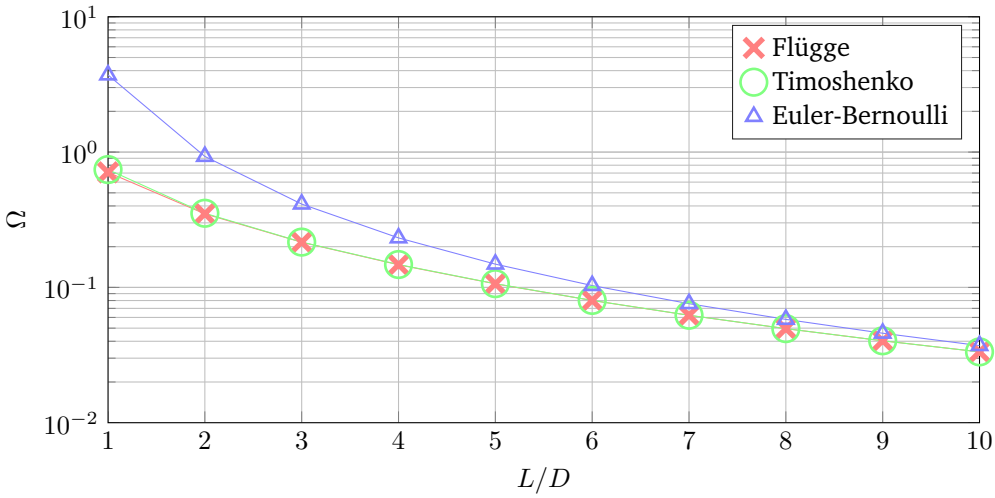

Figure 2.11: Comparison of the second dimensionless eigenfrequency of a cantilever cylinder with $h/D = 100$ according to Flügge's theory, Timoshenko's theory and Euler-Bernoulli's theory.

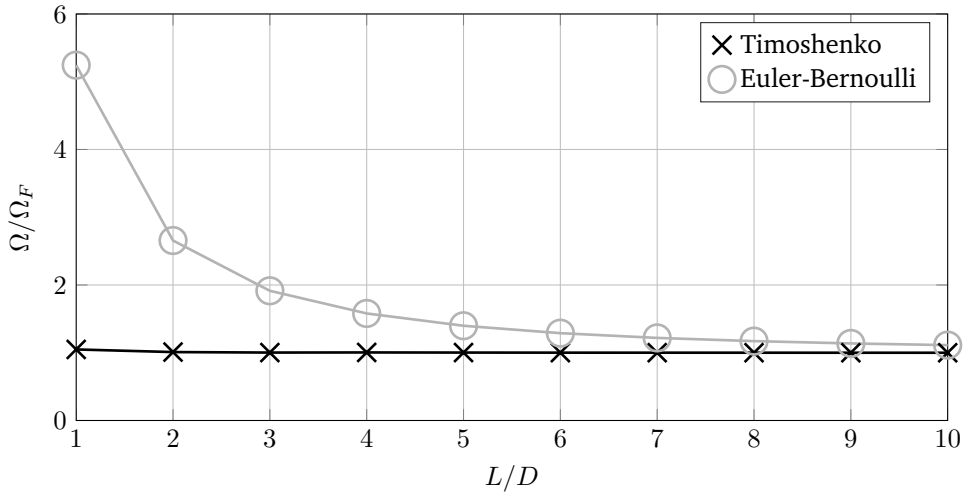

Figure 2.12: Ratio of Timoshenko's and Euler-Bernoulli's prediction to Flügge's prediction of a cantilever cylinder's first eigenfrequency with $h/D = 100$.

2.5 Forced vibration by means of modal expansion

2.5.1 Introduction

The method presented in this section to analyse a Timoshenko beam and a Flügge shell cylinder in forced vibration will be based on the previously derived eigenmodes. Knowing the eigenvalues of the cylinder makes it possible to obtain the forced solution in terms of these eigenvalues. This is referred to as modal expansion. An advantage of this method is that it is computationally fast. For this study in particular, modal expansion is a desirable method as it will give insight into how much each mode contributes to the total response of the structure. When analysing the stress levels in the cylinder wall, contributions made by shell modes with a circumferential wavenumber of $n > 1$ are thus easily observed. Hereby insight can be obtained in the contribution of shell deformation to the fatigue life time of the structure. Modal expansion is widely used in the dynamic analysis of circular cylindrical shells and, as is shown in chapter 4, modal expansion shares the same concept with various model reduction methods applied to discrete systems. The theory presented in this section can thus be used to apply the reduction methods discussed in chapter 4 to the continuous shell and beam equations.

2.5.2 Modal participation factor

Consider a cylinder subjected to a given dynamic surface loading. The load will excite the modes of the cylinder in various amounts. These amounts are quantified for each mode by means of a modal participation factor. Mathematically, any response of the system can be expressed as a combination of all the orthogonal vectors that satisfy the structure's boundary conditions. Since beams and shells are continuous systems, the number of degrees of freedom is infinite. Therefore, the response of the structure must be expressed as an infinite series of orthogonal vectors. Using beam theory, in general we take

$$\psi(x,t) = \sum_{k=1}^{\infty} \Psi_k(x)\eta_k(t), \tag{2.43}$$

where $\psi(x,t)$ is the total response of the system in a given direction, $\Psi_k(x)$ is the kth eigenmode in the given direction and $\eta_k(t)$ is the time dependent modal participation factor for the kth mode. When using a shell theory, also the dependence on the circumferential coordinate θ must be accounted for. The equivalent of equation 2.43

is then written as

$$\psi(x,\theta,t) = \sum_{k=1}^{\infty} \Psi_k(x,\theta)\eta_k(t), \tag{2.44}$$

where the total response of the system and kth mode shape in a given direction are now given by $\psi(x,\theta,t)$ and $\Psi_k(x,\theta)$ respectively. In both equations 2.43 and 2.44 the modal participation factors are unknown and have to be determined, as will be explained in the following subsections.

Modal participation factors for Timosenko's beam theory

The inhomogeneous dynamic Timoshenko beam equations are given by equations 2.1a - 2.1b. Note that an equivalent viscous damping coefficient c has only been taken into account for the lateral displacement of the beam. In this section it is assumed that the rotational damping is negligible compared to the damping acting on the displacement. Alternatively, if a rotational damping term is added in the equation of motion the relations in the remainder of this section must be changed accordingly.

The solutions for the deflection $w(x,t)$ and rotation $\phi(x,t)$ of the Timoshenko beam will be expressed by the following series

$$w(x,t) = \sum_{k=1}^{N} W_k(x)\eta_k(t), \tag{2.45a}$$

$$\phi(x,t) = \sum_{k=1}^{N} \Phi_k(x)\eta_k(t). \tag{2.45b}$$

where N is the number of modes taken into consideration. By substitution of equations 2.45a - 2.45b into equations 2.1a - 2.1b, making use of equations 2.30a - 2.30b, multiplying both sides of the first and second equation with the pth mode shapes $W_p(x)$ and $\Phi_p(x)$ respectively, integrating over length L of the beam, applying the orthogonality property of eigenmodes and summing the two resulting equations gives the equation for the modal participation factor [18]. This equation can be written as

$$\frac{d^2\eta_k(t)}{dt^2} + 2\xi_k\omega_k\frac{d\eta_k(t)}{dt} + \omega_k^2\eta_k(t) = F_k(t), \tag{2.46}$$

where

$$\xi_k = \frac{c}{2\omega_k} \frac{\int_0^L W_k(x)^2 dx}{\int_0^L \rho I \Phi_k(x)^2 + \rho A W_k(x)^2 dx}, \tag{2.47a}$$

$$F_k(t) = \frac{\int_0^L q(x,t) W_k(x) dx}{\int_0^L \rho I \Phi(x)^2 + \rho A W_k(x)^2 dx}. \tag{2.47b}$$

The modal participation factor for the kth mode can now be solved from equation 2.46. The modal paticipation factor equation is a simple oscillator equation. In order to solve the transient response, two initial conditions must be specified. The amplitude $\hat{\eta}_k$ of the modal participation factor for the steady state response due to harmonic loading can be determined directly from

$$\hat{\eta}_k = \frac{F_k^*}{\left(\omega_k^2 - \omega^2\right) + 2}, \tag{2.48}$$

determining F_k^* using

$$F_k(t) = F_k^* e^{i\omega t}. \tag{2.49}$$

The modal participation factor η_k for the kth mode for the steady state response is now given by

$$\eta_k(t) = \hat{\eta}_k e^{i\omega t - \alpha_k}, \tag{2.50}$$

where the phase angle α_k is given by

$$\alpha_k = \tan^{-1}\left(\frac{2\xi_k(\omega/\omega_k)}{1-(\omega/\omega_k)^2}\right). \tag{2.51}$$

Modal participation factor for Flügge's shell theory Determination of the modal participation factor for shell theory is similar as demonstrated for Timoshenko's beam theory. The difference here is that three equations of motion are used and that the viscous damping is assumed to be the same in all principle directions. However, the assumption on the viscous damping can be relaxed leading to a slightly different derivation of the following equations. The starting point is the inhomogeneous dynamic equations of motion from Flügge's theory including viscous damping. These are given by equations 2.9a - 2.9c, where all terms $L_i(u,v,w)$ are again defined by equations 2.11a - 2.11f and substituting $c_1 = c_2 = c_3 = c$. For a shell theory

the solution for the axial, circumferential and radial displacements, respectively, will be an infinite series defined as

$$u(x,\theta,t) = \sum_{k=1}^{n} U_k(x,\theta)\eta_k(t), \tag{2.52a}$$

$$v(x,\theta,t) = \sum_{k=1}^{\infty} V_k(x,\theta)\eta_k(t), \tag{2.52b}$$

$$w(x,\theta,t) = \sum_{k=1}^{\infty} W_k(x,\theta)\eta_k(t). \tag{2.52c}$$

Using an approach similar to the one presented for Timoshenko's beam theory, the equation for the kth modal participation factor for shell theory can be written as

$$\omega_k^2\eta_k(t) + 2\xi_k\omega_k\frac{d\eta_k(t)}{dt} + \frac{d^2\eta_k(t)}{dt^2} = F_k(t), \tag{2.53}$$

where

$$\xi_k = \frac{c}{2\rho h\omega_k} \tag{2.54}$$

and

$$F_k(t) = \frac{\int_0^L \int_0^{2\pi} q_x(x,\theta,t)U_k(x,\theta) + q_\theta(x,\theta,t)V_k(x,\theta) + q_z(x,\theta,t)W_k(x,\theta)dxd\theta}{\rho A \int_0^L \int_0^{2\pi} U_k(x,\theta)^2 + V_k(x,\theta)^2 + W_k(x,\theta)^2 dxd\theta}. \tag{2.55}$$

Note that in order to arrive at this equation, the equations of motion where integrated over both the axial and circumferential coordinate. Similar to the Timoshenko beam, analysis of the shell's transient response needs two initial conditions. The steady state response can be analysed using equations 2.48 - 2.51 while substituting in equations 2.53 and 2.5.2.

2.6 Conclusions

In this chapter the static and dynamic modelling of cylinders according to Timoshenko's beam theory and Flügge's shell theory has been discussed. Several conclusions can be made.

– As was discussed in section 2.3.2, nature of the static response of a circular cylindrical shell subjected to a load depends on the distribution of the load over the cylinder's circumference. A load with a given harmonic circumferential distribution n will solely induce a response with the same harmonic circumferential distribution n. This also holds for the response to dynamic loading, as can be derived from equation 2.5.2. It can be observed that F_k will equal zero if the loading terms q_x, q_θ and q_z have a different circumferential wavenumber than the mode shapes U_k , V_k and W_k.

– Taking note of the previous statement, a monopile's shell deformation behaviour can be isolated from its global bending behaviour when using a circular cylindrical shell theory. For this, consider an offshore monopile subject to a certain load $P(x, \theta)$. P can be expressed in terms of a summation of the axial distributions $\hat{P}_n(x)$ multiplied with circumferential distributions $\cos(n\theta)$ or $\sin(n\theta)$. For each term with $n \neq 1$ cross-section deformations, and thus stresses induced in the monopile's shell, are not considered using Timoshenko's beam theory.

– From section 2.3.3 it can be observed that Flügge's shell theory and Timoshenko's beam theory are in agreement with each other with respect to the rotation and lateral displacement of the center point of the cylinder due to edge loading. For increasing slenderness and thin-walledness of the cylinder, the ratio between the Timoshenko beam and Flügge shell solution approaches 1.

– Cross sectional deformation can also occur for a cylinder subjected to a load with a circumferential distribution of $n = 1$ as the radial displacement amplitude can differ from the tangential displacement amplitude. A possible cause for this is the edge disturbance phenomena. An edge disturbance occurs near constraints regarding the cross sectional deformation, such as a rigidly clamped or rigid ring boundary condition. An edge disturbance will also be induced by loads at a free edge, the edge disturbance due to radial loading will be more prominent compared to tangential or axial loading. The length of the region affected by the edge disturbance will decrease relative to the axial length of a cylinder with increasing slenderness of the cylinder. This can be observed in section 2.3.3.

– Judging from section 2.4.5 it can be concluded that the predictions of the first and second (beam) eigenfrequency of a circular cylinder with Timoshenko's

beam theory and Flügge's shell theory converge towards each other with increasing slenderness of the cylinder. Compared to Euler-Bernouli's beam theory, the Timoshenko beam theory is in much better agreement with Flügge's shell theory, especially with decreasing slenderness of the cylinder.

Chapter 3

Soil-structure interaction

This chapter starts with a selected overview of different approaches that can be used to incorporate soil-structure interaction in the research models of the offshore wind turbine. After this, a method to obtain characteristics of an elastic foundation which approximates the reaction forces of the soil on the monopile is discussed. This method forms the basis for modelling the soil-structure interaction in the remainder of this study. The implementation of this method in the research models is therefore discussed in the closing section of this chapter.

3.1 Introduction

For a structure embedded in or founded on the soil, the behaviour of the structure affects the behaviour of the soil, and the behaviour of the soil affects the behaviour of the structure. Kinematic interaction mechanisms exist between the soil and the structure, such as the resistance of the soil to the deformations of an embedded pile. Also inertial interaction mechanisms occur. Due to dynamic forces exerted by the structure on the soil, deformation waves will propagate through the soil and away from the structure, which causes radiation damping [19]. In this chapter the soil-stiffness which resists the small amplitude motion of the monopile will be addressed.

In the design practice of offshore wind turbines specifically, soil-structure interaction is traditionally modelled by the p-y curve method [5]. [1] The small ratio of

[1] The soil resistance is modelled as uncoupled non-linear lateral springs where the spring stiffness is extracted by p-y curves. However, this method was developed for slender piles with diameters up to approximately 2.0 m [20].

embedded length over diameter that is currently employed in the industry, most probably invokes a fundamentally different soil reaction than the reaction for which the p-y curves were originally calibrated [21]. Additionally, the p-y curve method only predicts an effective lateral soil reaction. The distribution of the soil's resistance along the pile's circumference and the soil's response to self-balancing shell modes is thus not accounted for.

In this study another approach is chosen. Instead, use has been made of an available FEM model of a given soil. The FEM model consists of several homogeneous, isotropic and horizontally stratified soil layers, which are described using a mesh of linear solid elements within the commercial software package Ansys. The material properties, i.e., Young's modulus, Poisson's ratio and specific density, as well as the thickness of the soil layers are related to in situ seismic measurements of the nearshore wind farm Westermeerwind. The model is circular in the horizontal plane and the degrees of freedom of the nodes at the bottom and the sides of the model are constrained. Furthermore, the elements are meshed using cylindrical coordinates. Time-domain simulations of an offshore wind turbine directly coupled to the FEM model would not be computationally effective. Therefore, it is desirable to obtain an alternative way to incorporate the soil-structure characteristics of the soil described by the FEM model in the research models used in this thesis.

Three methods to incorporate soil-structure interaction in the research models are considered. The first method consists of a modal expansion with respect to the in vacuo modes of the monopile and those of the soil. The modes of the two systems can be coupled using interface conditions and the orthogonality properties of the modes [22]. In the second method, an augmented FEM is to be developed in which the monopile is included. The augmented FEM model can be transformed into a single superelement using a substructuring method. In the third method soil-structure interaction is accounted for by an equivalent spatial distribution of linear uncoupled elastic springs which act on a model of the monopile. To obtain the equivalent soil stiffness distribution, displacements are enforced upon the nodes within the soil in the FEM model. The stiffness is then obtained by dividing the nodal reactions forces by their displacements. In this study the last of the aforementioned methods is chosen. The reasoning for this is as follows: an equivalent soil stiffness distribution provides clear insight in the behaviour of the soil, while analysis of the offshore wind turbine remains conceptually simple and close to the current design practice.

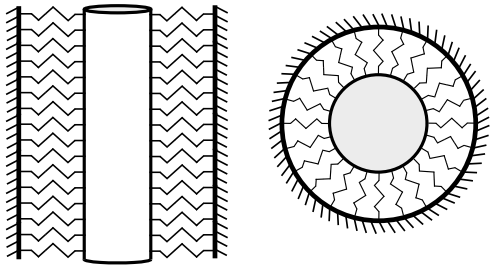

Figure 3.1: Front (left) and top (right) view of a vertical cylinder supported in the radial direction by an elastic foundation.

3.2 Derivation of an equivalent elastic spring stiffness

3.2.1 Introduction

This section describes the derivation of a spatial distribution of linear uncoupled elastic springs which approximate the reaction of the soil to deflections of the monopile. In this section it is assumed that the monopile extends from a certain depth within the soil to the mudline and is modelled as a circular cylindrical shell. The monopile's radius and wall thickness are assumed to be uniform along its length. In general, the soil reaction forces will enter the equations governing the motions of the shell by the following

$$\rho h \frac{\partial^2 u}{\partial t^2} + c_1 \frac{\partial u}{\partial t} - L_1\{u, v, w\} + K_1\{u, v, w\} = q_x, \tag{3.1a}$$

$$\rho h \frac{\partial^2 v}{\partial t^2} + c_2 \frac{\partial v}{\partial t} - L_2\{u, v, w\} + K_2\{u, v, w\} = q_\theta, \tag{3.1b}$$

$$\rho h \frac{\partial^2 w}{\partial t^2} + c_3 \frac{\partial w}{\partial t} - L_3\{u, v, w\} + K_3\{u, v, w\} = q_z, \tag{3.1c}$$

where K_1, K_2 and K_3 are yet unknown functions of u, v and w that represent the soil's reaction forces on the shell. To clarify, for a circular cylindrical shell supported by an elastic foundation in the radial direction with respect to the shell's surface, assuming a constant foundation stiffness in the axial and circumferential direction, the foundation stiffness terms in equation 3.1 are given by

$$K_1\{u, v, w\} = 0, \quad K_2\{u, v, w\} = 0, \quad K_3\{u, v, w\} = \hat{k}_z, \tag{3.2}$$

where $\hat{k}_z$ is a constant which represents the magnitude of the stiffness in the radial direction. A schematization of a shell supported in the radial direction by an elastic foundation is shown in figure 3.1.

For the research models, the functions K_1, K_2 and K_3 must now be chosen in correspondence with the considered FEM model of the soil. To keep the analysis of the shell similar to chapter 2, the functions K_1, K_2 and K_3 represent uncoupled elastic springs. As opposed to a set of uncoupled distributed springs, a three dimensional FEM model is able to capture the non-local behaviour of the soil. [2] However, a set of distributed springs can be tuned to approximate the reaction of the FEM model due to a given displacement field. The procedure for this is as follows.

Let S_{MP} be a surface within the FEM model. S_{MP} is an open, vertical cylinder with a radius a, which extends from the mudline to a depth L and has a centreline which coincides with the vertical centreline of the FEM model. S_{MP} represents the geometry of the part of the monopile which is embedded in the soil. N_{MP} is the set of nodes in the FEM model which lie on S_{MP}. Three distinct displacement fields, given by $\boldsymbol{D}_x$, $\boldsymbol{D}_\theta$ and $\boldsymbol{D}_z$, are imposed upon N_{MP} and for each displacement field the nodal reaction forces and moments are calculated for all nodes $\in N_{MP}$. The displacement fields $\boldsymbol{D}_x$, $\boldsymbol{D}_\theta$ and $\boldsymbol{D}_z$ consist solely of displacements which are respectively axial, tangential and radial with respect to S_{MP}. At the locations of N_{MP}, equivalent discrete spring stiffness constants can be determined as

$$\tilde{k}_{ij}^q = F_i^q / u_j^q \tag{3.3}$$

where $\tilde{k}_{ij}^q$ is the stiffness constant of an elastic spring, exerting a force F_i upon node $q \in N_{MP}$ in direction i due to a displacement u_j of q in direction j. The magnitude of $\tilde{k}_{ij}^q$ will depend on the chosen displacement fields. Therefore, the displacement fields should represent the behaviour of the monopile in the soil. The following two sections describe the derivation of the characteristics of the elastic foundation based on two types of the displacement fields.

3.2.2 The circumferential wavenumber method

As discussed in chapter 2, solutions to the shell equations can be found by decomposing the loading and resulting deformations as a Fourier series of harmonic functions along the cylinder's circumference. The deformations of the shell are thus assumed

[2] Here non-local behaviour implies that a reaction force at a given location within the soil, due to an enforced displacement field, depends on the entire displacement field, rather than solely the displacement at the given location.

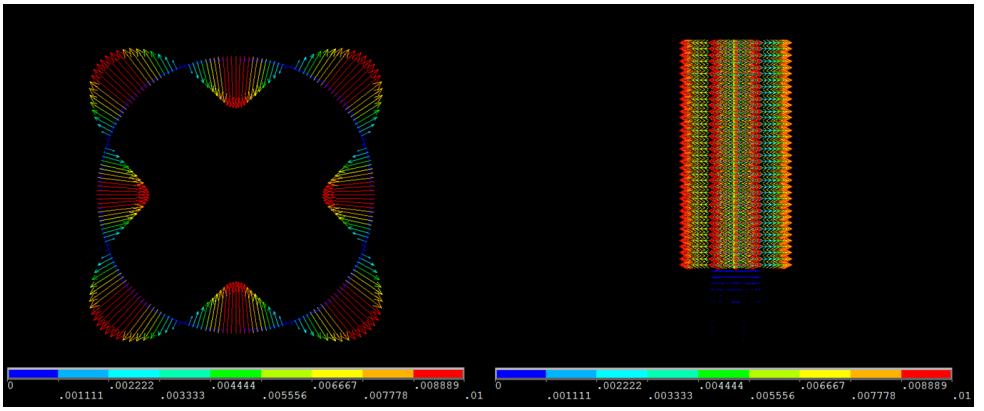

Figure 3.2: A top view (left) and frontal view (right) of the displacement field $\boldsymbol{D}_4 z$, taken from the Ansys graphical user interface.

to be of the following form.

$$u(x,\theta) = \sum_{n=0}^{\infty} U_n(x)\cos(n\theta) \tag{3.4a}$$

$$v(x,\theta) = \sum_{n=0}^{\infty} V_n(x)\sin(n\theta) \tag{3.4b}$$

$$w(x,\theta) = \sum_{n=0}^{\infty} W_n(x)\cos(n\theta) \tag{3.4c}$$

For each circumferential wavenumber n, the corresponding equations of motion can be solved independently in order to find solutions for $U_n(x)$, $V_n(x)$ and $W_n(x)$. The equivalent soil stiffness terms $K_1\{u,v,w\}$, $K_2\{u,v,w\}$ and $K_3\{u,v,w\}$ will be derived separately for each circumferential wavenumber n. For this purpose, the formulations of the displacement fields, corresponding to circumferential wavenumber n, are chosen as

$$\boldsymbol{D}_{nx} = \hat{u}\cos(n\theta), \tag{3.5a}$$

$$\boldsymbol{D}_{n\theta} = \hat{v}\sin(n\theta), \tag{3.5b}$$

$$\boldsymbol{D}_{nz} = \hat{w}\cos(n\theta). \tag{3.5c}$$

Here θ describes the position along the circumference of S_{MP} while $\hat{u}$, $\hat{v}$ and $\hat{w}$ are constants which denote the amplitudes of the displacement fields in respectively the

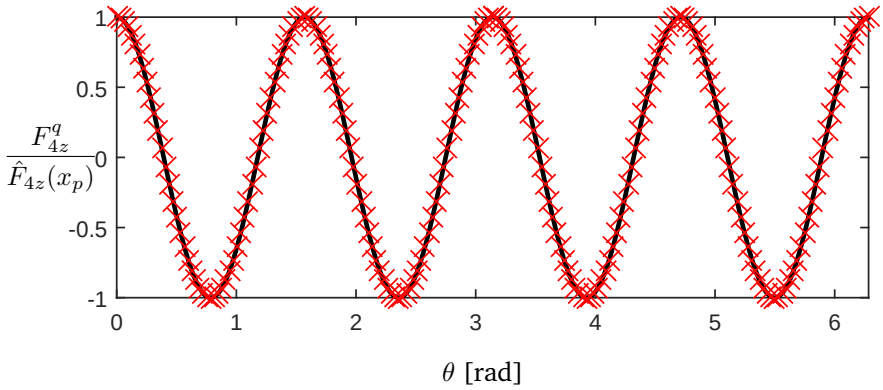

Figure 3.3: A comparison of the normalized distribution of reaction forces in the FEM model in the radial direction at $x = x_p$, due to $\boldsymbol{D}_{4z}$, given by $F^q_{4z}/\hat{F}_{4z}(x_p)$ ($\times$) and $\cos(4\theta)$ ($-$)

axial, tangential and radial direction. It is noted that the displacement of the nodes is constant over the vertical direction and only varied along the circumference of S_{MP} in the FEM model. A representation of the radial displacement field $\boldsymbol{D}_{4z}$, acting on N_{MP} in the FEM model, is given in figure 3.2. Note that only displacements of the nodes with a distance a from the centre point of the model are visualized.

Distribution of reaction forces over the circumferential direction

Due to all displacement fields it is found that, along the circumference of S_{MP}, the nodal reaction forces follow a harmonic distribution with the same circumferential wavenumber as the displacement fields. In other words, due to a given displacement field $\boldsymbol{D}_{nj}$ the reaction forces can be described by

$$F^q_{nxj} = \hat{F}_{nxj}(x)\cos(n\theta), \tag{3.6a}$$

$$F^q_{n\theta j} = \hat{F}_{n\theta j}(x)\sin(n\theta), \tag{3.6b}$$

$$F^q_{nzj} = \hat{F}_{nzj}(x)\cos(n\theta), \tag{3.6c}$$

where q denotes the number of a node. $\hat{F}_{nij}(x)$ is the amplitude of the reaction forces at x. The amplitudes $\hat{F}_{nij}(x)$ are equal to the reaction force at the vertical lines $\theta = 0$ for $i = x$ or $i = z$, and to the reaction force at $\theta = \frac{\pi}{2}$ for $i = \theta$. Note that equation 3.6 still describes the discrete reaction forces at the individual nodes. An example calculation of a normalized distribution of the nodal reaction forces over the circumference of S_{MP} is visualized in figure 3.3. The reaction forces in figure 3.3 act in the radial direction and are calculated at $x = x_p = -10$ due to $\boldsymbol{D}_{4z}$.

Stiffness profiles in the vertical direction

While along the circumferential direction of S_{MP} the distribution of the soils reac-

tion forces can be formulated using harmonic functions, the profile along the vertical direction of S_{MP} is much more irregular. For the circumferential wavenumbers $n = 1$ to $n = 10$ the soil's (discrete) spring stiffness profiles are given in figure 3.4. The stiffness profiles $\hat{K}_{nij}$ are obtained by dividing the amplitudes of the reaction forces $\hat{F}_{nij}$ by the amplitudes of the displacement fields $\hat{u}$, $\hat{v}$ or $\hat{w}$. It can be noted that these spring stiffness profiles equal the profiles for the reaction forces in [Newton] at the nodes on the lines $\theta = 0$ or $\theta = \frac{\pi}{2}$ due to displacement fields with unit amplitude, i.e., using equation 3.5 with $\hat{u} = \hat{v} = \hat{w} = 1$.

Interpretation of the obtained stiffness profiles

First, we distinguish between two types of stiffness profiles, defined as direct stiffness profiles and coupled stiffness profiles. For $i = x$, θ and z, the profiles $\hat{K}_{nii}$, i.e., $\hat{K}_{nxx}$, $\hat{K}_{n\theta\theta}$ and $\hat{K}_{nzz}$, are referred to as direct stiffness profiles. These profiles relate reaction forces in a direction i due to a displacement of the nodes in the same direction. For $i = x$, θ and z, and $j = x$, θ and z, the profiles $\hat{K}_{nij}$, where $i \neq j$, are referred to as coupled stiffness profiles. These profiles relate reaction forces in a direction i due to a displacement in a different direction j.

It is observed that direct stiffness profiles (i) are of higher magnitude then the indirect stiffness profiles, (ii) are always positive, (iii) indicate a similar vertical position of stiff and soft soil layers, and (iv) increase in magnitude for increasing n. If a node in the mesh is displaced in the direction i, it is not hard to imagine that the reaction force in the direction i will be of a larger magnitude then the reaction forces in the other two directions. While the reaction forces in the direction of the displacement are directly related to the stress strain relations governing the solid elements, the reaction forces in the other directions are introduced through Poisson's effect. For all soil layers the Poisson's ratio is defined as $0.3 < \nu < 0.5$, it is thus expected that the reaction forces in the same direction as the enforced displacements are of the largest magnitude. It is also expected that these reaction forces counteract the displacements, and therefore lead to positive values for the stiffness profiles. The increase of the soil stiffness for increasing n can be explained using the curvature of the displacement fields. A higher value for n will introduce a higher rate of change of the curvature of the line that describes the displacement field in the horizontal plane. This will lead to reaction forces of a higher magnitude at the nodes in the FEM model.

The indirect stiffness profiles $\hat{K}_{n\theta z}$ and $\hat{K}_{nz\theta}$ describe coupling between forces and displacements in the horizontal plane. The characteristics for these profiles are similar to the characteristics of the direct stiffness profiles. Additionally the stiffness profiles prove to be symmetric, this is expected since the FEM model consists

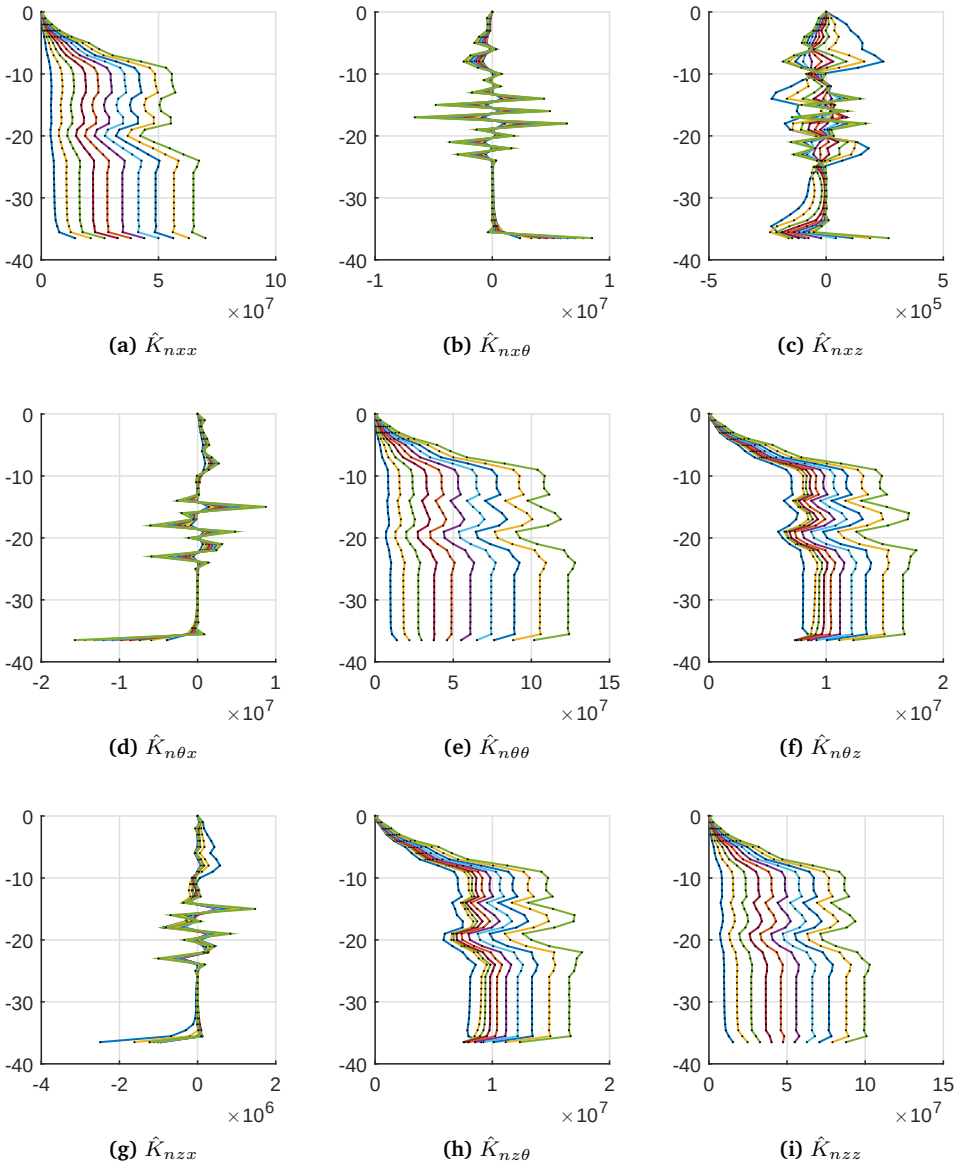

(a) $\hat{K}_{nxx}$ **(b)** $\hat{K}_{nx\theta}$ **(c)** $\hat{K}_{nxz}$

(d) $\hat{K}_{n\theta x}$ **(e)** $\hat{K}_{n\theta\theta}$ **(f)** $\hat{K}_{n\theta z}$

(g) $\hat{K}_{nzx}$ **(h)** $\hat{K}_{nz\theta}$ **(i)** $\hat{K}_{nzz}$

Figure 3.4: Plot of the discrete spring stiffness profiles for $n = 1$ to $n = 10$. The values for the spring stiffness at the nodes are all plotted as black dots. Coloured lines connect the dots corresponding to each value of n. The color of the lines representing n=1 to n=10 can be observed from left to right in **(a)**. In all figure's the vertical axis represents the position relative to the mudline in [m] and the horizontal axis represents the spring stiffness at the node in [N/m].

of linear solid elements. The profiles that describe the coupling between the vertical and the horizontal plane are given by $\hat{K}_{nx\theta}$, $\hat{K}_{nxz}$, $\hat{K}_{n\theta x}$ and $\hat{K}_{nzx}$. These profiles appear to be very irregular and contain both negative and positive values. The occurrence of both negative and positive values is to be expected. For example, due to a displacement field which describes radial contraction of N_{MP}, the nodes near the upper layer of the model will be pulled downwards while the nodes positioned around the bottom of S_{MP} will be pulled upwards. This leads to a different sign in the obtained stiffness for the nodes at the top and the bottom of the model. The irregularity in the obtained stiffness profile may have a threefold of causes: (i) different soil layers which are present in the model, (ii) only nodes above a certain depth in the model are displaced, and (iii) there is a difference in boundary conditions at the top and bottom of the model, at the top the nodes are free to move in any direction while at the bottom of the model the nodes are constrained. The spikiness of the obtained stiffness profiles may be explained using the distance between the nodes in the vertical plane. It might be the case that a more refined mesh would lead to a smooth stiffness profile. It is striking that the pair $\hat{K}_{nx\theta}$ and $\hat{K}_{n\theta x}$ as well as the pair $\hat{K}_{nxz}$ and $\hat{K}_{nzx}$ are not symmetric (or antisymmetric, depending on the definition of the global axis system). This may also be explained by the distance between the nodes in the vertical direction. If the stiffness would consist of a irregularly shaped, but smooth function with a high rate of change of curvature, small numerical errors may have a big influence on the values obtained for the reaction forces at the discrete nodes. Therefore, the discrete stiffness profiles may appear to be non-symmetrical. Due to time constraints on this research, no further investigation was performed on the derived stiffness profiles. It was concluded that, while some of the indirect stiffness profiles are probably derived incorrect, they are still usable for the remainder of this study. It should be noted that in all calculations with the circumferential wavenumber method, 38 nodes were used in the vertical direction of S_{MP} while 200 nodes were used over the circumference of S_{MP}. The high resolution along the circumference of S_{MP} was chosen in order to accurately represent the harmonic functions that describe the displacement fields. In hindsight it might have been a better choice to redistribute the density of the nodes more equally over both the vertical direction and the horizontal plane.

The stiffness profiles derived using a wavenumber of $n = 0$ show similar properties to the ones presented in figure 3.4, the direct profiles appear regular with an indication of the soft and stiff soil layers. Only two indirect profiles exist. The profiles describe the coupling between the vertical and radial direction. Similar irregularities to those in the indirect profiles for higher numbers of n are noticeable. Similar to the relations governing the behaviour of circular cylindrical shells for $n = 0$, the tangential direction is uncoupled from the other directions due to symmetry. Because the

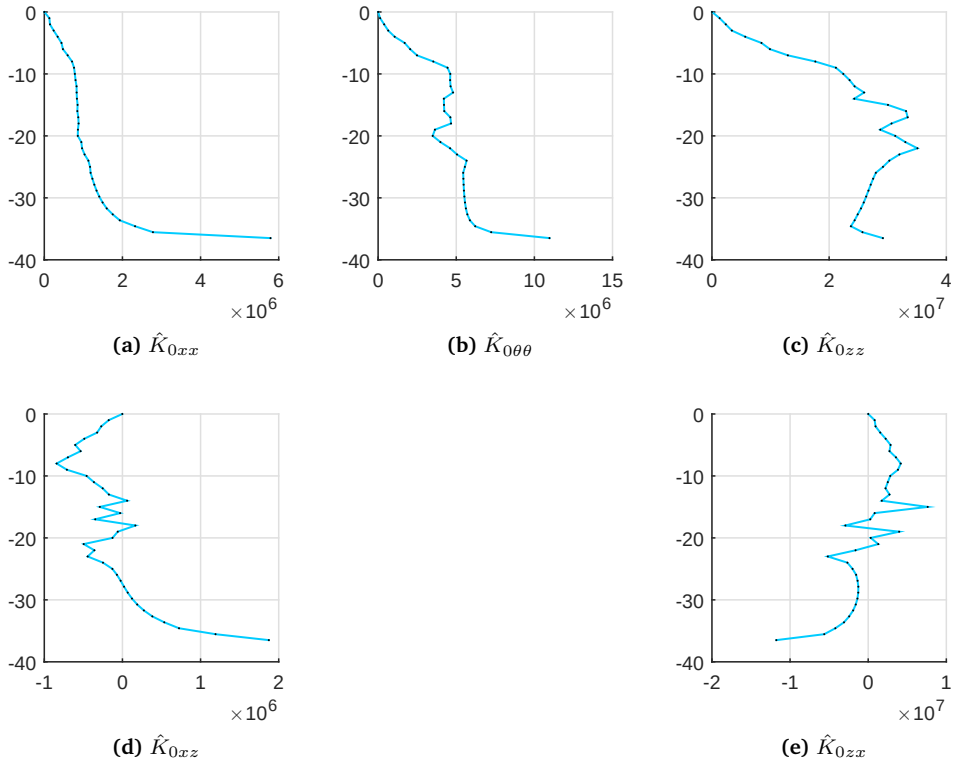

(a) $\hat{K}_{0xx}$ **(b)** $\hat{K}_{0\theta\theta}$ **(c)** $\hat{K}_{0zz}$

(d) $\hat{K}_{0xz}$ **(e)** $\hat{K}_{0zx}$

Figure 3.5: Plot of the discrete spring stiffness profiles for $n = 0$. The values for the spring stiffness at the nodes are all plotted as black dots, which are connected by a light blue line. In all figure's the vertical axis represents the position relative to the mudline in [m] and the horizontal axis represents the spring stiffness at the node in [N/m].

obtained stiffness profiles for $n = 0$ are of different shape and/or magnitude compared to the profiles obtained for $n > 0$, they are presented separately in figure 3.5.

Formulation of the total stiffness distribution

In order to keep analysis of the shell on the equivalent elastic foundation similar to

the methods presented in chapter 2, some assumptions are made. It is assumed that between any two successive nodes on any vertical line in S_{MP}, the stiffness of the elastic foundation is constant. The shell is hereby divided into 37 segments in the vertical direction. Since (i) both the reaction forces and the displacement fields are described by harmonic functions with the same wavenumber over the circumference of S_{MP}, and (ii) the stiffness distributions are constant for each shell segment, the terms corresponding to the elastic foundation in equations 3.1 can, for each individual segment, be written as

$$\begin{bmatrix} K_1^{(s)}\{u,v,w\} \\ K_2^{(s)}\{u,v,w\} \\ K_3^{(s)}\{u,v,w\} \end{bmatrix} = \begin{bmatrix} k_{nxx}^{(s)} & k_{nx\theta}^{(s)} \frac{1}{n}\frac{\partial}{\partial\theta} & k_{nxz}^{(s)} \\ -k_{n\theta x}^{(s)} \frac{1}{n}\frac{\partial}{\partial\theta} & k_{n\theta\theta}^{(s)} & -k_{n\theta z}^{(s)} \frac{1}{n}\frac{\partial}{\partial\theta} \\ k_{nzx}^{(s)} & k_{nz\theta}^{(s)} \frac{1}{n}\frac{\partial}{\partial\theta} & k_{nzz}^{(s)} \end{bmatrix} \begin{bmatrix} u^{(s)}(x,\theta) \\ v^{(s)}(x,\theta) \\ w^{(s)}(x,\theta) \end{bmatrix}, \tag{3.7}$$

where (s) denotes the segment. In equation 3.7 the derivatives with respect to θ are introduced to ensure that all terms have the proper distribution in the circumferential direction. Analysis of the segmented shell is discussed in detail in chapter 4. The values for the stiffness constants, given by $k_{nij}^{(s)}$ for $i = x,\ \theta,\ z$ and $j = x,\ \theta,\ z$ are derived using the discrete stiffness profiles over the vertical direction, as shown in figure 3.4 in combination with equation 3.6. The stiffness of the discrete springs is distributed over the surface of S_{MP} assuming a constant distribution in the vertical direction and a harmonic distribution in the circumferential direction. A detailed overview of the steps involved is given in appendix A.

3.2.3 The mode shape method

Another possibility is to derive an equivalent soil stiffness according to the modal behaviour of the wind turbine. Since the first eigenmode of the wind turbine is the most design driving, an attempt was made to determine an equivalent soil stiffness distribution which approximates the reaction of the soil due to displacement of the monopile according to this first eigenmode. In order to determine the first eigenmode, an augmented FEM model was developed which included a mesh of the monopile and tower using shell elements. In this model the nodes of the soil were fixed to the monopile and the effect of the RNA on the modal behaviour of the wind turbine was taken into account by applying a point mass and rotary inertia to the top of the tower. The extended model is shown in figure 3.6a.

The nodal displacements corresponding to the first eigenmode are obtained through an eigenvalue analysis. An impression of the first modeshape is given in figure 3.6b.

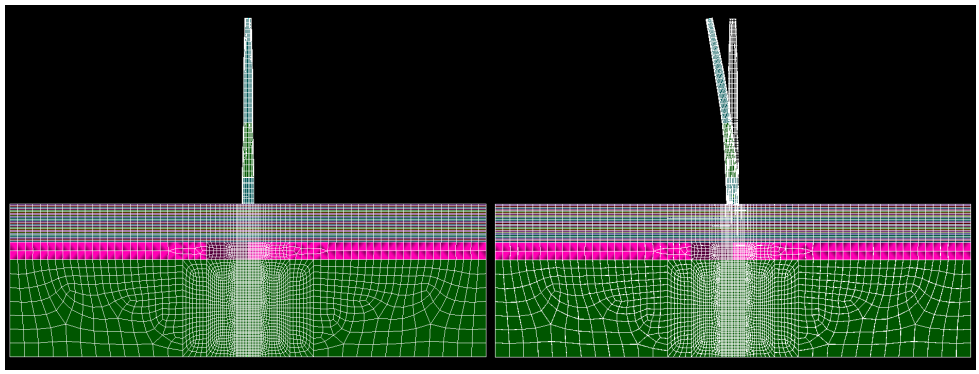

(a) Impression of the extended model. **(b)** Impression of the first mode shape.

Figure 3.6: Impression of the extended model and the first mode shape.

The obtained displacements are decomposed into three displacement fields which contain the axial, tangential and radial displacement of the nodes with respect to the monopile's surface. Due to each of the three displacement fields, reaction forces on the nodes in the continuum model are obtained in the axial, tangential and radial direction with respect to the surface S_{MP}. The stiffness profiles were derived following the same procedure as in section 3.2.2. As can be seen in figure 3.7, a singularity effect is found at a distance of -20 m relative to the mudline. This effect is due to the division of nodal reaction forces by small nodal displacements. Direct implementation of the stiffness with the non-physical singularity effects in the research model will lead to local disturbances of the deformation of the shell wall, most notable in the radial direction. It is therefore desirable to circumvent these mathematical anomalies. For this purpose, several methods are available. The first method involves curve fitting in order to derive an equivalent stiffness profile, which may be defined using a higher order polynomial function. An application of this method to derive a stiffness profile for an Euler-Bernoulli beam is shown in [21]. The implementation of a comparable method for a shell problem is considered to be too demanding from a computational point of view. Much more unknowns will be present in the derivation and the calculations necessary to solve these unknowns are computationally more expensive. In a different method, the area directly surrounding the singularity effects could be neglected altogether. An equivalent stiffness in the neglected region can then, for example, be approximated using interpolation.

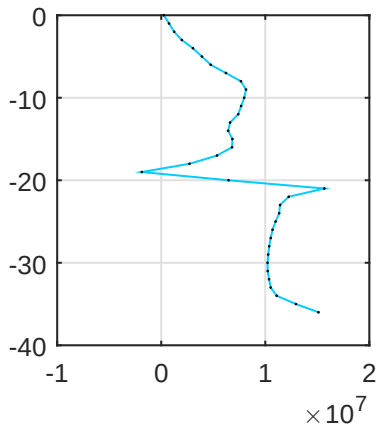

(a) K_{1zz}

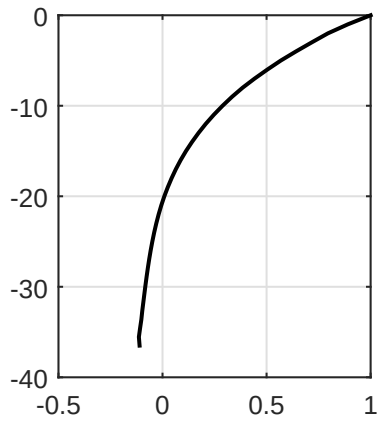

(b) $W_1(x)$

Figure 3.7: (a) Plot of the discrete spring stiffness profile K_{1zz}, derived using the mode shape method. The values for the spring stiffness at the nodes are all plotted as black dots, which are connected by a light blue line. The vertical axis represents the position relative to the mudline in [m] and the horizontal axis represents the spring stiffness at the node in [N/m]. **(b)** The radial deformations according to the first eigenmode of the wind turbine. The vertical axis represents the position relative to the mudline in [m] and the horizontal axis represents the normalized deformation shape in [m].

The circumferential wavenumber method	The mode shape method
No knowledge of the mode shapes required	Capture non-local effects of the soil
Calculate only once per circumferential wavenumber	
No singularity effects in the stiffness profiles	

Table 3.1: Comparison of the positive aspects governing the circumferential wavenumber method and the mode shape method.

3.2.4 Discussion on the circumferential wavenumber method and the mode shape method

In the previous sections, two distinct methods were discussed which can be used to obtain an equivalent elastic foundation from the FEM model. While the mode shape method will arguably lead to the best approximation of the equivalent elastic foundation, it also has negative aspects. While the mode shape method is able to capture the non-local behaviour of the soil, it also requires the knowledge of the mode shapes beforehand. Additionally, the non-local effects are only taken into account if the resulting displacements from the continuous shell are the same as, or at least similar to, the displacements used to calculate the equivalent elastic foundation. This may lead to a large number of calculations that need to be performed in the augmented FEM model. Additionally, undesirable mathematical anomalies will occur in the obtained stiffness curves in the region where the displacement fields approach zero. On the contrary, the circumferential wave number method does not come with these negative aspects. The only negative aspect governing the circumferential wavenumber method is that the non-local effects of the soil are only partly taken into account. A short overview of the positive and negative aspects governing the circumferential wavenumber method and the mode shape method is presented in tables 3.1 and 3.2. The calculations regarding soil-structure interaction for the remainder of this study will follow the circumferential wavenumber method. The application of this method in the research models is elaborated upon in section 3.3.

The circumferential wavenumber method	The mode shape method
Capture non-local effect partially	Requires knowledge of the mode shapes
	Needs to be calculated for each mode
	Singularity effects in the in the stiffness profiles

Table 3.2: Comparison of the negative aspects governing the circumferential wavenumber method and the modal method.

3.3 Application in the research models: deriving the elastic foundation's characteristics

3.3.1 Overview

A schematic overview of the steps that are taken in order to account for soil-structure interaction in this study is presented in figure 3.8. Using the circumferential wavenumber method, displacement fields are enforced on a set of nodes within the FEM model of the soil. The set of nodes is chosen in correspondence with the monopile under consideration. Through 3 static calculations per n, the nodal reaction forces on the nodes are obtained. At the nodes, equivalent discrete spring stiffness values are obtained by division of the nodal reaction forces through the enforced displacements. The discrete equivalent springs are transformed to a distributed elastic foundation, which is applied to the continuous shell model of the monopile. Based on figure 3.2 a harmonic distribution with wavenumber n over the monopile's circumference is assumed. The monopile within the soil is partitioned in 36 segments in the vertical direction. Each segment is assigned a constant stiffness distribution over the vertical direction, which is based on the stiffness profiles obtained in section 3.2.2. For each shell segment, the terms representing the derived equivalent elastic foundation are given by equation 3.7. In order to obtain the stiffness distributions for the Timoshenko beam model, the stiffness distributions corresponding to $n = 1$ for the shell model are integrated over the circumference of the monopile. It should hereby be noted that the stiffness distribution K_{1xx} will be translated to a stiffness working on the rotational degree of freedom of the Timoshenko beam mode while distributions $K_{1\theta\theta}$ and K_{1zz} are translated to a stiffness working on the deflection of the Timoshenko beam. The indirect stiffness profiles are translated accordingly. The elastic

foundation can enter the equations of motion governing the Timoshenko beam as

$$\rho A\frac{\partial^2 w}{\partial t^2} + c\frac{\partial w}{\partial t} + \frac{\partial}{\partial x}\left[\kappa AG\left(\frac{\partial w}{\partial x} - \phi\right)\right] + K_1\{w,\phi\} = q, \tag{3.8a}$$

$$\rho I\frac{\partial^2 \phi}{\partial t^2} - EI\frac{\partial}{\partial x}\left(\frac{\partial \phi}{\partial x}\right) - \kappa AG\left(\frac{\partial w}{\partial x} - \phi\right) + K_2\{w,\phi\} = 0, \tag{3.8b}$$

where for each segment (s)

$$\begin{bmatrix} K_1^{(s)}\{w,\phi\} \\ K_2^{(s)}\{w,\phi\} \end{bmatrix} = \begin{bmatrix} k_{qw}^{(s)} & k_{q\phi}^{(s)} \\ k_{pw}^{(s)} & k_{p\phi}^{(s)} \end{bmatrix} \begin{bmatrix} w^{(s)}(x) \\ \phi^{(s)}(x) \end{bmatrix}, \tag{3.9}$$

with

$$k_{qw}^{(s)} = \pi a\left(k_{\theta\theta}^{(s)} + k_{zz}^{(s)} - k_{\theta z}^{(s)} - k_{z\theta}^{(s)}\right), \tag{3.10a}$$

$$k_{q\phi}^{(s)} = \pi a^2\left(k_{\theta x}^{(s)} - k_{zx}^{(s)}\right), \tag{3.10b}$$

$$k_{pw}^{(s)} = \pi a^2\left(k_{x\theta}^{(s)} - k_{xz}^{(s)}\right), \tag{3.10c}$$

$$k_{p\phi}^{(s)} = \pi a^3 k_{xx}^{(s)}. \tag{3.10d}$$

In equations 3.10 a different notation for the subscripts was chosen in order to avoid confusion with the stiffness distributions governing the shell equations.

3.3.2 Comparison with the FEM model

For the region within the soil we can mimic the displacements corresponding to the first modeshape of the complete wind turbine using a static analysis. For this purpose, the FEM model of the soil is augmented with the part of the monopile below the mudline. At the mudline, a static lateral load and a static overturning moment are applied to the monopile. It was found that a ratio of force to moment equal to 1:200 gives the best approximation of the first modeshape for the monopile under consideration in this study. It was also found that, using a ratio of 1:200 in the static analysis, the resulting deformation shape of the monopile is dominated by the overturning moment.

As a verification of the obtained stiffness profile by means of the circumferential wavenumber method, a comparison is made with the FEM model. For this purpose, a static analysis is performed which compares the response of the augmented FEM model to the response of the continuous shell and beam model on the elastic foundations for two load cases. For the first and second load case respectively, the monopile

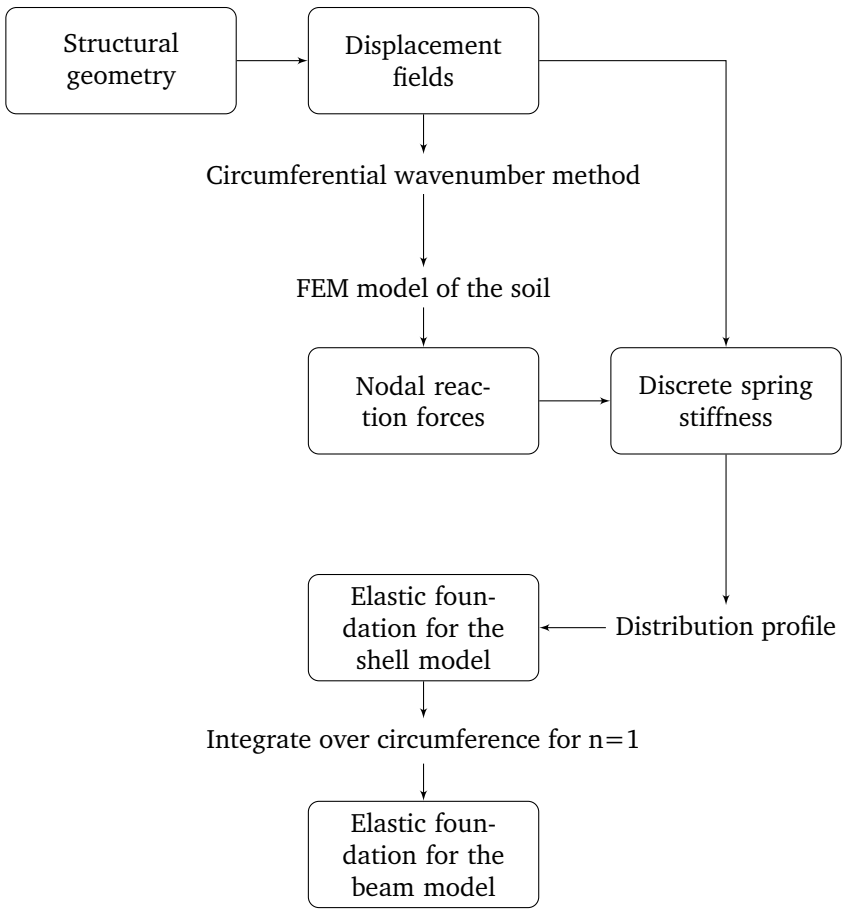

Figure 3.8: Flowchart for the calculation of the elastic foundations for the case study.

is subject to a lateral load of 1 MN and an overturning moment of 1 MNm , which are both applied at the mudline. The resulting deformation shapes of the monopile are shown in figures 3.9 and 3.10. It is observed that the curves that represent the continuous model do not match the curves predicted by the FEM model. Good agreement is found between the continuous shell and beam model, which is to be expected based on the formulation of the stiffness profile and observations made in chapter 2.

Based on previous reasoning it is believed that the continuous shell and beam model will be able to represent the first bending mode of the wind turbine in a matter that is sufficient for the further calculations in this study. While it is obvious that a true equivalent elastic foundation was not derived, it is believed that the soil-structure interaction is still taken into account in a manner which is good enough for the remainder of this study. While not further investigated, it can be argued that the response of the continuous shell model better approximates the behaviour of the augmented FEM model for higher values of n. For $n = 1$ the monopile laterally deforms within the soil, which leads to significant non-local effects in the vertical direction. As for higher values of n, the deformations of the shell are symmetrical in various planes. Therefore, the non-local effects over the vertical direction for $n > 1$ are expected to be of less importance with respect to those corresponding to $n = 1$.

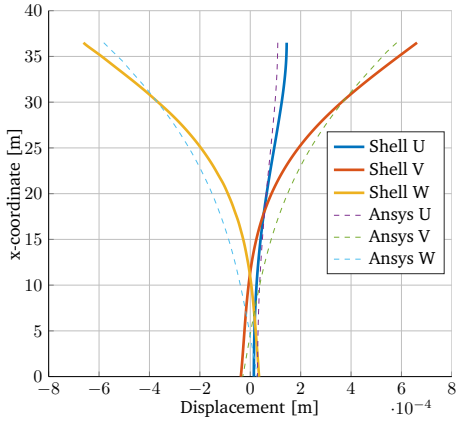

(a) Response to a shear force of 1 MN at the mudline.

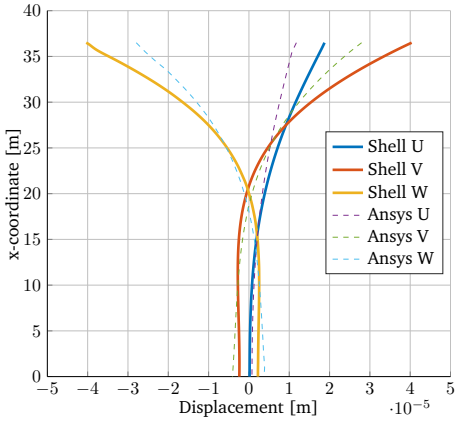

(b) Response to an overturning moment of 1 MNm at the mudline.

Figure 3.9: Comparing the monopile's response predicted by the continuous shell model and the FEM model due to a lateral load and an overturning moment at the mudline. The x-coordinate is defined from the bottom of the monopile, at $x = 0$, until the mudline, at $x = 36.5$. U, V and W represent the axial distributions of the shell deformations.

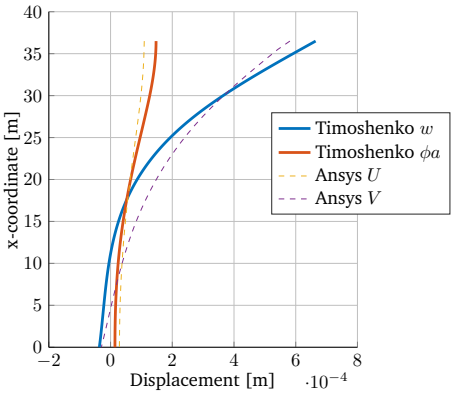

(a) Response to a shear force of 1 MN at the mudline.

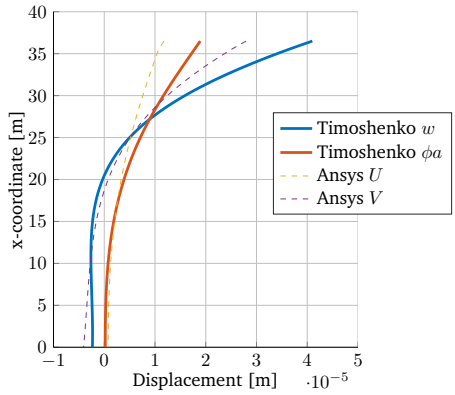

(b) Response to an overturning moment of 1 MNm at the mudline.

Figure 3.10: Comparing the monopile's response predicted by the continuous Timoshenko beam model and the FEM model due to a shear force and an overturning moment at the mudline. The x-coordinate is defined from the bottom of the monopile, at $x = 0$, until the mudline, at $x = 36.5$. U and V represent the axial distributions of the shell deformations while w and ϕ represent the deformations of the beam.

Chapter 4

Analysis by superelements

In this chapter two strategies are presented to describe the mechanics of the monopile support structure using solely continuous and homogeneous beam or cylindrical shell segments. The first strategy involves the coupling of various segments, in order to accommodate for inhomogeneities in the vertical direction, by using interface conditions. The second strategy involves a transformation of the entire model of the monopile into a single superelement. The superelement is expressed in terms of a set of generalized coordinates, which are derived according to the Craig-Bampton substructuring method. The application of the two strategies to the research models of the monopile is also discussed.

4.1 Introduction

In a superelement analysis of a structure, said structure is divided into a set of superelements which each represent a different part of the structure. In literature, several terms are used to refer to these superelements such as components, segments, sections or substructures, depending on the nature of the structure, the selection of the parts and the method of analysis. A location where two or more parts of the total structure are connected to one another is referred to as an interface. This chapter will cover two methods that are based on the superelement concept. In section 4.2 a method is discussed that can be used to simplify the partial differential equations describing a continuous system. The simplification is obtained by analysing the system as a set of interconnected parts, which will be referred to as segments. The behaviour of each individual segment can be expressed by the general solution to

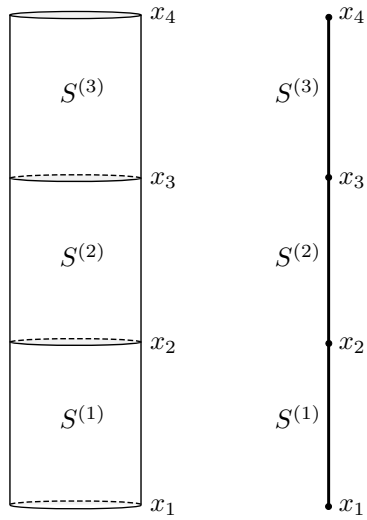

Figure 4.1: A cylinder consisting of three superelements modelled with shell theory (left) and beam theory (right).

the partial differential equations describing only the segment. The general solutions for all of the interconnected segments can then be coupled through boundary and interface conditions in order to describe the behaviour of the total system. In sections 4.3 and 4.4, model reduction and substructuring for dynamic systems is discussed. The term substructuring is used here as a collective term for methods that express the equations of motion of a structure in terms of generalized coordinates and make use of a set of constraint equations to describe the connection between the substructures. These substructures can be seen as superelements. Section 4.5 will discuss the application of the various superelement methods to the research models.

4.2 Coupling of continuous shell and beam segments

Division of a large and complex structure into a set of superelements can be used to simplify the systems of equations describing the structure's behaviour. This division can for example be applied to a beam which consists of several segments, where each segment has unique material properties. Using this method, calculation of the response of a non-homogeneous circular cylindrical shell or beam remains straight

forward and in accordance with chapter 2. Similarly, this method can be used to add ring stiffeners between two cylindrical shell sections or to couple a cylindrical shell element to a shell element with a different type of geometry, such as a conical or spherical section [23, 24].

In this section it is shown how a model of a cylinder can be divided into a set of segments in the axial direction. When using a beam theory, the interface is defined as a point along the axial coordinate x_i. When using a circular cylindrical shell theory, the interface is also defined at an axial coordinate x_i, division along the circumferential coordinate is not required. At the interface, each segment will be a circular cylindrical shell, connected trough a circular line [13]. Once the division into segments is made, the behaviour of the entire cylinder can be described with a piecewise function. For a cylinder with outer boundaries x_1 and x_4, consisting of three segments $S^{(1)}$, $S^{(2)}$ and $S^{(3)}$, where segments $S^{(1)}$ and $S^{(2)}$ are connected to each other at interface x_2 and where $S^{(2)}$ and $S^{(3)}$ are connected with each other at interface x_3, the response $\phi(x,\theta)$ of the cylinder is described by

$$\phi(x,\theta) = \begin{cases} \phi^{(1)}(x,\theta) & \text{if} \quad x_1 \leq x \leq x_2, \\ \phi^{(2)}(x,\theta) & \text{if} \quad x_2 \leq x \leq x_3, \\ \phi^{(3)}(x,\theta) & \text{if} \quad x_3 \leq x \leq x_4, \end{cases} \tag{4.1}$$

where $x_1 < x_2 < x_3 < x_4$ and the response of segment $S^{(i)}$ is described with $\phi^{(i)}(x,\theta)$. The general form of the functions for the segments $\phi^{(i)}(x,\theta)$ can be solved individually from their governing differential equations. The integration constants governing the functions for all segments can be solved trough boundary and interface conditions. Using beam theory, two boundary conditions are used at each end of the cylinder and 4 interface conditions are used at each interface. For two Timoshenko beam segments $S^{(i)}$ and $S^{(i+1)}$ connected at $x_i + 1$ with no additional interface physics, continuity is enforced using the following relations

$$\begin{cases} w^i = w^{i+1} & \text{at} \quad x = x_{i+1}, \\ \phi^i = \phi^{i+1} & \text{at} \quad x = x_{i+1}, \\ V^i = V^{i+1} & \text{at} \quad x = x_{i+1}, \\ M^i = M^{i+1} & \text{at} \quad x = x_{i+1}. \end{cases}$$

For two circular cylindrical shell elements the continuity conditions at the interface would be given by

$$\begin{cases} u^i = u^{i+1} & \text{at} \quad x = x_{i+1}, \\ v^i = v^{i+1} & \text{at} \quad x = x_{i+1}, \\ w^i = w^{i+1} & \text{at} \quad x = x_{i+1}, \\ \phi^i = \phi^{i+1} & \text{at} \quad x = x_{i+1}, \\ M^i_{xx} = M^{i+1}_{xx} & \text{at} \quad x = x_{i+1}, \\ N^i_{xx} = N^{i+1}_{xx} & \text{at} \quad x = x_{i+1}, \\ T^i_x = T^{i+1}_x & \text{at} \quad x = x_{i+1}, \\ S^i_x = S^{i+1}_x & \text{at} \quad x = x_{i+1}. \end{cases}$$

The boundary condition matrix $\boldsymbol{R}$ will be of the following form

$$\boldsymbol{R} = \begin{bmatrix} \boldsymbol{B}_t^{(1)} & . & . & . & . & . \\ \boldsymbol{I}_b^{(1)} & \boldsymbol{I}_t^{(2)} & . & . & . & . \\ . & \boldsymbol{I}_b^{(2)} & \boldsymbol{I}_t^{(3)} & . & . & . \\ . & . & \ddots & \ddots & . & . \\ . & . & . & \boldsymbol{I}_b^{(N-2)} & \boldsymbol{I}_t^{(N-1)} & . \\ . & . & . & . & \boldsymbol{I}_b^{(N-1)} & \boldsymbol{I}_t^{(N)} \\ . & . & . & . & . & \boldsymbol{B}_b^{(N)} \end{bmatrix}, \tag{4.2}$$

where $\boldsymbol{B}$ and $\boldsymbol{I}$ are block matrices that represent boundary and interface conditions respectively. The subscripts b and t denote the top and bottom of the segments. The B matrices are of size $k \times l$ while the I matrices are of size $2k \times l$. When using a beam theory, $k = 2$ and $l = 4$. When using a shell theory, $k = 4$ and $l = 8$.

4.3 Model reduction methods for discrete systems

To represent a structure with a discrete model, often a high spatial resolution is desired in order to analyse the structure's deformation behaviour and stress distributions in high detail. However, a high spatial resolution also comes with a high computational cost, as it requires a many degrees of freedom. Especially in dynamic time simulations of detailed finite element models, computational costs can become unacceptable. Fortunately, procedures to reduce a system's number of degrees of freedom without altering the spatial resolution are available, these methods are known as model reduction methods. A model reduction method makes use of

the following representation:

$$\boldsymbol{u} = \boldsymbol{R}\tilde{\boldsymbol{q}}. \tag{4.3}$$

Where $\boldsymbol{u}$ is a vector containing the original degrees of freedom, $\boldsymbol{R}$ is the reduction basis matrix, describes the transformation to the system's generalized coordinates. The vector $\tilde{\boldsymbol{q}}$ represents the amplitudes of these generalized coordinates. Reduction of the system can be obtained by selection of a set of generalized coordinates which is much smaller then the number of original degrees of freedom. If the system's eigenmodes are chosen as generalized coordinates, then the columns of $\boldsymbol{R}$ contain the deformation shapes of the eigenmodes and $\tilde{\boldsymbol{q}}$ contains the amplitudes of these eigenmodes. This would be equivalent to the modal expansion technique as discussed in section 2.5, but now applied to discrete systems.

When applying the reduction method, the equation of motion governing a discrete dynamic system can be transformed from

$$\boldsymbol{M}\ddot{\boldsymbol{u}} + \boldsymbol{C}\dot{\boldsymbol{u}} + \boldsymbol{K}\boldsymbol{u} = \boldsymbol{p}, \tag{4.4}$$

into

$$\tilde{\boldsymbol{M}}\ddot{\tilde{\boldsymbol{q}}} + \tilde{\boldsymbol{C}}\dot{\tilde{\boldsymbol{q}}} + \tilde{\boldsymbol{K}}\tilde{\boldsymbol{q}} = \tilde{\boldsymbol{p}}, \tag{4.5}$$

where $\boldsymbol{M}$, $\boldsymbol{C}$ and $\boldsymbol{K}$ are the system's mass, damping and stiffness matrices respectively and $\boldsymbol{p}$ denotes the dynamic external load vector. The reduced matrices $\tilde{\boldsymbol{M}}$, $\tilde{\boldsymbol{C}}$ and $\tilde{\boldsymbol{K}}$ and reduced load vector $\tilde{\boldsymbol{p}}$ are given by

$$\tilde{\boldsymbol{M}} = \boldsymbol{R}^T\boldsymbol{M}\boldsymbol{R} \tag{4.6a}$$

$$\tilde{\boldsymbol{C}} = \boldsymbol{R}^T\boldsymbol{C}\boldsymbol{R} \tag{4.6b}$$

$$\tilde{\boldsymbol{K}} = \boldsymbol{R}^T\boldsymbol{K}\boldsymbol{R} \tag{4.6c}$$

$$\tilde{\boldsymbol{p}} = \boldsymbol{R}^T\boldsymbol{p} \tag{4.6d}$$

where $\boldsymbol{A}^T$ denotes the transpose of a given matrix $\boldsymbol{A}$. Note that when using this method, while a high spatial resolution is maintained, only an approximate solution is found as the systems motion is limited to the set of generalized coordinates. In the following section it is shown how the model reduction principle is applied in the Craig-Bampton substructure method.

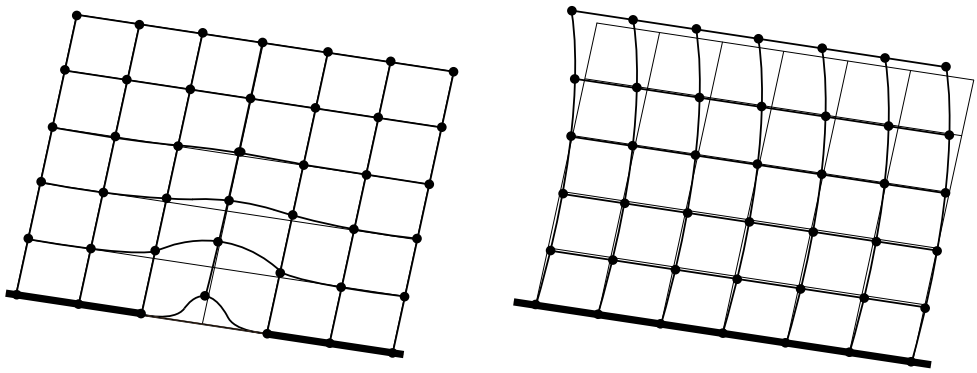

(a) Static constraint mode **(b)** Fixed interface vibration mode

Figure 4.2: A Static constraint mode **(a)** and a fixed interface vibration mode **(b)** of a substructure as used in the Craig-Bampton method.

4.4 The Craig-Bampton substructuring method

4.4.1 Formulation of the reduction basis

Substructuring has found application in the offshore wind industry as it provides a way to analyse complex support structures, such as jackets, in a computationally effective way during time domain simulations [25]. The Graig-Bampton method [26] is a substructuring method that expresses the behaviour of a structure in terms of structural modes. The method is often used in combination with finite element models since it reduces the degrees of freedom of the model to the number of modes taken into consideration. Two types of structural modes are used in the Craig-Bampton method, these are referred to as static constraint modes and fixed interface vibration modes. The two types of modes are visualized in figure 4.2.

Static constraint modes are obtained by enforcing a unit displacement of a single boundary degree of freedom while keeping all other boundary degrees of freedom constrained. The set of static constraint modes includes a mode for each boundary degree of freedom. Fixed interface vibration modes are eigenmodes of the structure determined with all boundary degrees of freedom constrained. The set of fixed interface vibration modes is given by N eigenmodes, where N is the number of modes taken into consideration. The Craig-Bampton method can be seen as an extension of the Guyan-Irons method [27, 28] with the method of modal expansion.

Consider a system as described by equation 4.4. The system is partitioned into internal and boundary degrees of freedom which are denoted with subscripts i and b respectively.

$$\begin{bmatrix} \boldsymbol{M}_{bb} & \boldsymbol{M}_{bi} \\ \boldsymbol{M}_{ib} & \boldsymbol{M}_{ii} \end{bmatrix} \begin{bmatrix} \ddot{\boldsymbol{u}}_b \\ \ddot{\boldsymbol{u}}_i \end{bmatrix} + \begin{bmatrix} \boldsymbol{C}_{bb} & \boldsymbol{C}_{bi} \\ \boldsymbol{C}_{ib} & \boldsymbol{C}_{ii} \end{bmatrix} \begin{bmatrix} \dot{\boldsymbol{u}}_b \\ \dot{\boldsymbol{u}}_i \end{bmatrix} + \begin{bmatrix} \boldsymbol{K}_{bb} & \boldsymbol{K}_{bi} \\ \boldsymbol{K}_{ib} & \boldsymbol{K}_{ii} \end{bmatrix} \begin{bmatrix} \boldsymbol{u}_b \\ \boldsymbol{u}_i \end{bmatrix} = \begin{bmatrix} \boldsymbol{f}_b \\ \boldsymbol{f}_i \end{bmatrix} \tag{4.7}$$

The internal degrees of freedom of the system are approximated as follows using the Craig-Bampton method

$$\boldsymbol{u}_i \approx \boldsymbol{\Psi}_c \boldsymbol{u}_b + \boldsymbol{\Phi}_i \boldsymbol{\eta}_i, \tag{4.8}$$

while the boundary degrees of freedom remain present in the reduced system. The previous approximation leads to the following reduction basis

$$\begin{bmatrix} \boldsymbol{u}_b \\ \boldsymbol{u}_i \end{bmatrix} \approx \begin{bmatrix} \boldsymbol{I} & 0 \\ \boldsymbol{\Psi}_c & \boldsymbol{\Phi}_i \end{bmatrix} \begin{bmatrix} \boldsymbol{u}_b \\ \boldsymbol{\eta}_i \end{bmatrix} = \boldsymbol{R}_{CB} \tilde{\boldsymbol{q}} \tag{4.9}$$

where $\boldsymbol{u}_i$ and $\boldsymbol{u}_b$ are the internal and boundary degrees of freedom of the system respectively, $\boldsymbol{\Psi}_c$ and $\boldsymbol{\Phi}_i$ are the sets of static constraint modes and fixed interface vibration modes respectively, $\boldsymbol{R}_{BC}$ is the Craig-Bampton reduction matrix and $\tilde{\boldsymbol{q}}$ is the set of unknowns of the reduced system. The original system, as described by equation 4.4, can be transformed into a reduced system using equation 4.5 and 4.6 with substitution of $\boldsymbol{R}_{CB}$ as the reduction matrix $\boldsymbol{R}$.

4.4.2 Assembly of substructures

Similar to the assembly of segments in section 4.2, substructures can also be assembled to each other at their interfaces. This is done by enforcing continuity at each interface degree of freedom. A system consisting of multiple substructures can be assembled using a procedure taken from [29]. The equations of motion of a substructure s may be written as

$$\boldsymbol{M}^{(s)} \ddot{\boldsymbol{u}} + \boldsymbol{C}^{(s)} \dot{\boldsymbol{u}} + \boldsymbol{K}^{(s)} \boldsymbol{u} = \boldsymbol{f}^{(s)} + \boldsymbol{g}^{(s)}. \tag{4.10}$$

In this equation $\boldsymbol{M}^{(s)}$, $\boldsymbol{C}^{(s)}$ and $\boldsymbol{K}^{(s)}$ denote the substructure's mass, damping and stiffness matrices respectively, $\boldsymbol{f}^{(s)}$ is the external force vector and $\boldsymbol{g}^{(s)}$ is the vector of connecting forces with the other substructures. The equations of motion of k substructures that are to be coupled, can be written in a block-diagonal format as

$$\boldsymbol{M} \ddot{\boldsymbol{u}} + \boldsymbol{C} \dot{\boldsymbol{u}} + \boldsymbol{K} \boldsymbol{u} = \boldsymbol{f} + \boldsymbol{g} \tag{4.11}$$

where

$$\boldsymbol{M} \triangleq \text{diag}\left(\boldsymbol{M}^{(1)},...,\boldsymbol{M}^{(k)}\right) = \begin{bmatrix} \boldsymbol{M}^{(1)} & . & . \\ . & \ddots & . \\ . & . & \boldsymbol{M}^{(k)} \end{bmatrix},$$

$$\boldsymbol{C} \triangleq \text{diag}\left(\boldsymbol{C}^{(1)},...,\boldsymbol{C}^{(k)}\right),\ \boldsymbol{K} \triangleq \text{diag}\left(\boldsymbol{K}^{(1)},...,\boldsymbol{K}^{(k)}\right)$$

$$\boldsymbol{u} \triangleq \begin{bmatrix} \boldsymbol{u}^{(1)} \\ \vdots \\ \boldsymbol{u}^{(k)} \end{bmatrix}, \qquad \boldsymbol{f} \triangleq \begin{bmatrix} \boldsymbol{f}^{(1)} \\ \vdots \\ \boldsymbol{f}^{(k)} \end{bmatrix}, \qquad \boldsymbol{g} \triangleq \begin{bmatrix} \boldsymbol{g}^{(1)} \\ \vdots \\ \boldsymbol{g}^{(k)} \end{bmatrix}.$$

Continuity is now enforced through the compatibility and equilibrium conditions. The compatibility condition is expressed as

$$\boldsymbol{B}\boldsymbol{u} = \boldsymbol{0} \tag{4.12}$$

where $\boldsymbol{B}$ is a signed Boolean matrix which operates on the interface degrees of freedom. The compatibility condition states that any pair of matching interface degrees of freedom $u^{(k)}$ and $u^{(l)}$ must have the same displacement, i.e., $u^{(k)} - u^{(l)} = 0$. The equilibrium condition is enforced by

$$\boldsymbol{L}^T\boldsymbol{g} = \boldsymbol{0} \tag{4.13}$$

where L is the Boolean matrix localizing the interface degrees of freedom of the substructures in the global dual set of degrees of freedom. The equilibrium condition states that the resultant of the pair of dual connection forces acting on a pair of matching interface degrees of freedom must equal zero. Note that if model reduction is applied to a substructure, the reduced formulation for the mass, stiffness and damping matrices as well as the degrees of freedom can be substituted in the relations presented in this section.

4.5 Application in the research models: modelling the monopile

4.5.1 Overview

A schematic overview of the application of steps related to superelement modelling in the research model is presented in figure 4.3. First, two structural models of the

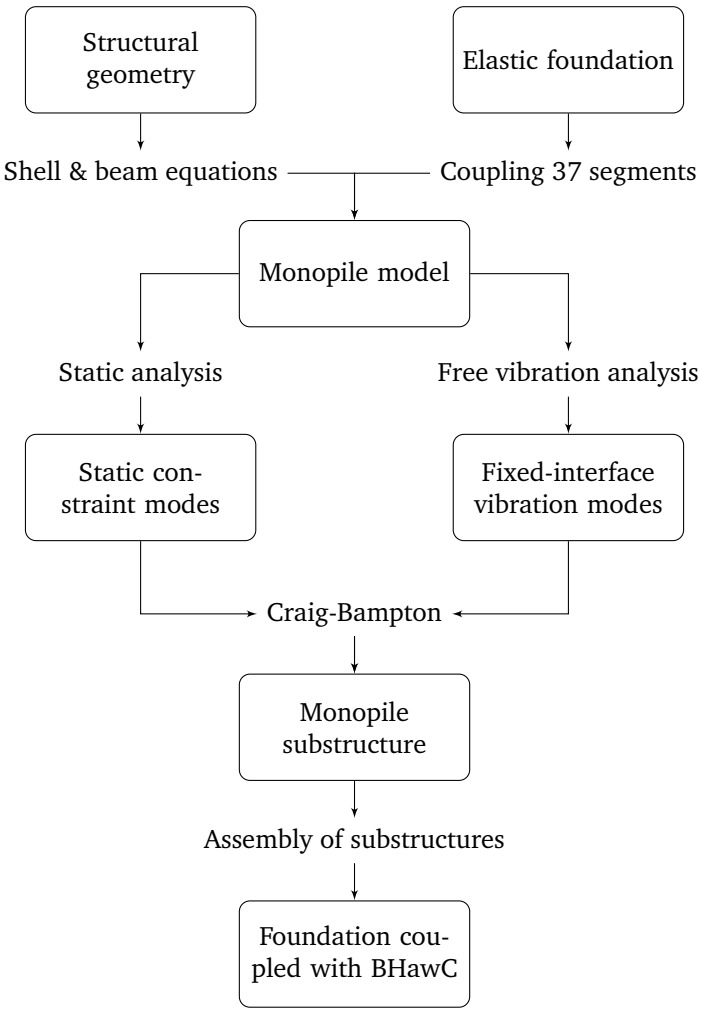

Figure 4.3: Flowchart for the application of superelement modelling for the research models.

monopile are developed using Timoshenko's beam theory and Flügge's circular cylindrical shell theory, as described in chapter 2. The elastic foundation, as derived in chapter 3 is included by dividing the monopile in 37 segments in the axial direction according to section 4.2. The 36 lowest segments represent the part of the monopile embedded within the soil while the top segment represents the part of the monopile from the mudline to the interface level. The monopile support structure will act as a single substructure. Using the Craig-Bampton method, the monopile will be transformed into a superelement which is connected to the tower at the interface level. This superelement can then be coupled to Siemens' BHawC in order to run time-domain simulations of the foundation coupled to the tower and RNA.

The motion of the monopile in a three-dimensional coordinate system is described by 6 degrees of freedom. Similar to the classical application of the Craig-Bampton analysis, these degrees of freedom are contained in a column vector $\boldsymbol{u}$, which now consists of functions of x, θ and t as

$$\boldsymbol{u}_{shell} = \begin{bmatrix} u_a(x,\theta,t) \\ v_a(x,\theta,t) \\ w_a(x,\theta,t) \\ u_b(x,\theta,t) \\ v_b(x,\theta,t) \\ w_b(x,\theta,t) \end{bmatrix}, \qquad \boldsymbol{u}_{beam} = \begin{bmatrix} w_a(x,t) \\ \phi_a(x,t) \\ w_b(x,t) \\ \phi_b(x,t) \\ \Lambda(x,t) \\ \Theta(x,t) \end{bmatrix}, \tag{4.14}$$

where for the displacements of the shell and beam model, the notation as in chapter 2 is used. Λ and Θ denote the vertical and torsional motion in the Timoshenko beam model.[1] The subscripts a and b denote the orientation of the shell and beam model with respect to the axis system as presented in figure 4.4. Subscript a denotes that the positive lateral deflection of the monopile is defined in the $\hat{q}_x$ direction, while subscript b denotes a positive lateral deflection in the $\hat{q}_y$ direction.

4.5.2 Formulation of the reduction basis

The boundary degrees of freedom will be described by six static constraint modes, corresponding to deflections in the directions $\hat{q}_x$ to $\hat{q}_{\alpha z}$. The internal degrees of freedom are represented by $N \times M$ fixed interface vibration modes. Here M represents the axial order of the modes and N the circumferential order. For this study it is expected that $M = 16$ is sufficient to describe the dynamic behaviour of the monopile

[1] In the equations governing the Timoshenko beam, as presented in chapter 2, axial and torsional deformations are not taken into account. Λ and Θ represent dummy variables that describe the motion of the monopile in the vertical and torsional direction. In actual calculations, the shell equations were used to determine the torsional and axial behaviour of the monopile in both models.

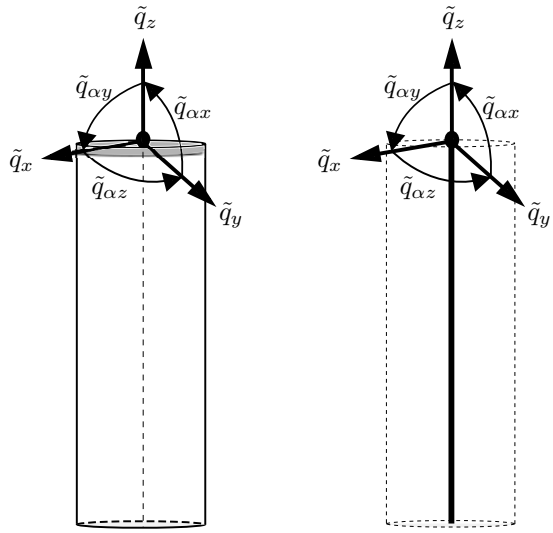

Figure 4.4: The boundary degrees of freedom visualized for the shell (left) and beam (right) model.

in the research models. For the beam model N can only be chosen as 1, while for the shell model N is chosen as 4. To clarify, the first 16 fixed interface vibration modes are taken into consideration for the beam model. For the shell model, the first 16 modes are used for n =1, 2, 3 and 4, resulting in 64 modes. Combination of the fixed interface vibration modes with the static constraint modes and accounting for the orientations of the monopile, given by a and b, leads to the reduced system. This system has 38 degrees of freedom using the beam model and has 134 degrees of freedom using the shell model. The reduction basis matrices $\boldsymbol{R}$ are then formulated as

$$\boldsymbol{R} = \begin{bmatrix} \boldsymbol{R}_G & \boldsymbol{R}_E \end{bmatrix} \tag{4.15}$$

where for the shell model, the static constraint modes are partitioned as

$$\boldsymbol{R}_{G,shell} = \begin{bmatrix} u_{q_x}(x,\theta) & 0 & u_z(x,\theta) & 0 & u_{q_{\alpha y}}(x,\theta) & u_{\alpha z}(x,\theta) \\ v_{q_x}(x,\theta) & 0 & 0 & 0 & v_{q_{\alpha y}}(x,\theta) & v_{\alpha z}(x,\theta) \\ w_{q_x}(x,\theta) & 0 & w_z(x,\theta) & 0 & w_{q_{\alpha y}}(x,\theta) & w_{\alpha z}(x,\theta) \\ 0 & u_{q_y}(x,\theta) & 0 & u_{q_{\alpha x}}(x,\theta) & 0 & 0 \\ 0 & v_{q_y}(x,\theta) & 0 & v_{q_{\alpha x}}(x,\theta) & 0 & 0 \\ 0 & w_{q_y}(x,\theta) & 0 & w_{q_{\alpha x}}(x,\theta) & 0 & 0 \end{bmatrix} \tag{4.16}$$

where for $i = x,\ y,\ z,\ \alpha x,\ \alpha y$ and αz, the functions u_{q_i}, v_{q_i} and w_{q_i} represent the displacement fields of the monopile, due to a unit displacement enforced in the direction $\hat{q}_i$ at interface level, while displacements in all other directions are constrained at the interface. The fixed interface vibration modes are included using

$$\boldsymbol{R}_{E,shell} = \begin{bmatrix} \boldsymbol{R}_{E1} & \boldsymbol{R}_{E2} & \boldsymbol{R}_{E3} & \boldsymbol{R}_{E4} & 0 & 0 & 0 & 0 \\ 0 & 0 & 0 & 0 & \boldsymbol{R}_{E1} & \boldsymbol{R}_{E2} & \boldsymbol{R}_{E3} & \boldsymbol{R}_{E4} \end{bmatrix} \tag{4.17}$$

where for circumferential wavenumber $n = 1$, 2, 3 and 4

$$\boldsymbol{R}_{En} = \begin{bmatrix} u_{n1}(x,\theta) & \dots & u_{nM}(x,\theta) \\ v_{n1}(x,\theta) & \dots & v_{nM}(x,\theta) \\ w_{n1}(x,\theta) & \dots & w_{nM}(x,\theta) \end{bmatrix}. \tag{4.18}$$

For the beam model, similar relations are used.

$$\boldsymbol{R}_{G,beam} = \begin{bmatrix} w_{q_x}(x) & 0 & 0 & 0 & w_{q_{\alpha y}}(x) & 0 \\ \phi_{q_x}(x) & 0 & 0 & 0 & \phi_{q_{\alpha y}}(x) & 0 \\ 0 & w_{q_y}(x) & 0 & w_{q_{\alpha x}}(x) & 0 & 0 \\ 0 & \phi_{q_y}(x) & 0 & \phi_{q_{\alpha x}}(x) & 0 & 0 \\ 0 & 0 & \Lambda(x) & 0 & 0 & 0 \\ 0 & 0 & 0 & 0 & 0 & \Phi(x) \end{bmatrix} \tag{4.19}$$

$$\boldsymbol{R}_{E,beam} = \begin{bmatrix} \boldsymbol{R}_E & 0 \\ 0 & \boldsymbol{R}_E \end{bmatrix} \tag{4.20}$$

$$\boldsymbol{R}_E = \begin{bmatrix} w_1(x,\theta) & \dots & w_M(x,\theta) \\ \phi_1(x,\theta) & \dots & \phi_M(x,\theta) \end{bmatrix} \tag{4.21}$$

4.5.3 Formulation of the reduced system

Once the reduction basis is defined, the reduced system can be derived. The mass and stiffness matrices of the original systems are given by

$$\boldsymbol{M}_{beam} = \begin{bmatrix} \rho A & 0 & 0 & 0 \\ 0 & \rho I & 0 & 0 \\ 0 & 0 & \rho A & 0 \\ 0 & 0 & 0 & \rho I \end{bmatrix}, \tag{4.22}$$

$$\boldsymbol{M}_{shell} = \rho h \boldsymbol{I}_6, \tag{4.23}$$

where $\boldsymbol{I}_6$ is the 6×6 identity matrix, and

$$\boldsymbol{K}_{beam} = \begin{bmatrix} \kappa AG\dfrac{\partial^2}{\partial x^2} & -\kappa AG\dfrac{\partial}{\partial x} & 0 & 0 \\ -\kappa AG\dfrac{\partial}{\partial x} & -EI\dfrac{\partial^2}{\partial x^2} + \kappa AG & 0 & 0 \\ 0 & 0 & \kappa AG\dfrac{\partial^2}{\partial x^2} & -\kappa AG\dfrac{\partial}{\partial x} \\ 0 & 0 & -\kappa AG\dfrac{\partial}{\partial x} & -EI\dfrac{\partial^2}{\partial x^2} + \kappa AG \end{bmatrix}, \quad (4.24)$$

$$\boldsymbol{K}_{shell} = -\begin{bmatrix} L_{11} & L_{12} & L_{13} & 0 & 0 & 0 \\ L_{21} & L_{22} & L_{23} & 0 & 0 & 0 \\ L_{31} & L_{32} & L_{33} & 0 & 0 & 0 \\ 0 & 0 & 0 & L_{11} & L_{12} & L_{13} \\ 0 & 0 & 0 & L_{21} & L_{22} & L_{23} \\ 0 & 0 & 0 & L_{31} & L_{32} & L_{33} \end{bmatrix}. \quad (4.25)$$

Since we are now dealing with a continuous system, the relations presented in section 4.3 and 4.4 are not sufficient. In accordance with section 2.5 and [30, 31], the reduced mass and stiffness matrices can be obtained by

$$\tilde{\boldsymbol{M}} = \int_0^L \int_0^{2\pi} \boldsymbol{R}^T \boldsymbol{M} \boldsymbol{R} dx d\theta = \begin{bmatrix} \boldsymbol{M}_{GG} & \boldsymbol{M}_{GE} \\ \boldsymbol{M}_{EG} & \boldsymbol{M}_{EE} \end{bmatrix} \quad (4.26)$$

and

$$\tilde{\boldsymbol{K}} = \int_0^L \int_0^{2\pi} \boldsymbol{R}^T \boldsymbol{K} \boldsymbol{R} dx d\theta = \begin{bmatrix} \boldsymbol{K}_{GG} & \boldsymbol{K}_{GE} \\ \boldsymbol{K}_{GE} & \boldsymbol{K}_{EE} \end{bmatrix}. \quad (4.27)$$

The matrices are partitioned in four blocks, denoted with subscripts G and E. M_{GG} and K_{GG} contain the contribution of the static constraint modes, these matrices equal the matrices obtained by the Guyan-Irons reduction method and are of size 6×6. M_{EE} and K_{EE} contain the contribution of the fixed interface vibration modes, these matrices equal the matrices as obtained through a classical modal expansion, which is discussed in section 2.5. These matrices are of size $NM \times NM$. Subscripts GE and EG denote the coupling between the two sets of modes. The matrices denoted with GE are of size $6 \times NM$. The matrices denoted with EG are the transpose of the matrices denoted with GE and are thus of size $NM \times 6$.

Since the mass matrix of the original system contains only constants, calculation of the matrix governing the reduced system is straight forward. The stiffness matrix

however, contains partial differential operators which lead to more complex computations. It is therefore worthwhile to rewrite the equations in a simpler manner. During the derivation of the static constraint modes it can be shown that

$$\boldsymbol{K}\boldsymbol{R}_G = \delta(x-L)\boldsymbol{F}_G \tag{4.28}$$

where δ is the Dirac delta function. F_G represents the edge loading, which can enter through the boundary conditions, that results in the static constrain modes. Using equation 4.28 it can be stated that

$$\boldsymbol{K}_{GG} = \int_0^L \int_0^{2\pi} \boldsymbol{R}_G^T \boldsymbol{K}\boldsymbol{R}_G dx d\theta = \int_0^L \int_0^{2\pi} \boldsymbol{R}_G^T \delta(x-L)\boldsymbol{F}_G dx d\theta = \int_0^{2\pi} \left(\boldsymbol{R}_G^T \boldsymbol{F}_G\right)_{x=L} d\theta \tag{4.29}$$

The fixed interface vibration modes are orthogonal on the stiffness matrix and thus both K_{GE} and K_{EG} are zero matrices.

$$\boldsymbol{K}_{EG} = \int_0^L \int_0^{2\pi} \boldsymbol{R}_E^T \boldsymbol{K}\boldsymbol{R}_G dx d\theta = \boldsymbol{0} \tag{4.30}$$

$$\boldsymbol{K}_{GE} = \int_0^L \int_0^{2\pi} \boldsymbol{R}_G^T \boldsymbol{K}\boldsymbol{R}_E dx d\theta = \boldsymbol{0} \tag{4.31}$$

Equation 4.30 is true due to equation 4.28. It can be argued that, due to symmetry, K_{GE} is also zero. Alternatively, this is shown by rewriting equation 4.28 as

$$\boldsymbol{R}_G = \boldsymbol{K}^{-1}\delta(x-L)\boldsymbol{F}_G, \tag{4.32}$$

therefore,

$$\boldsymbol{K}_{GE} = \int_0^L \int_0^{2\pi} \delta(x-L)\boldsymbol{F}_G^T \left(\boldsymbol{K}^{-1}\right)^T \boldsymbol{K}\boldsymbol{R}_E dx d\theta, \tag{4.33}$$

which, since $\boldsymbol{K}$ is symmetric, equals

$$\boldsymbol{K}_{GE} = \int_0^L \int_0^{2\pi} \delta(x-L)\boldsymbol{F}_E^T \boldsymbol{R}_E dx d\theta = \boldsymbol{0}. \tag{4.34}$$

Equations 4.34 and 4.30 equal zero since the normal modes are constrained at $x = L$. M_{GE} and M_{EG} are not zero matrices due to the presence of both static constraint modes and fixed interface vibration modes. It is additionally worthwhile to note that, if the fixed interface vibration modes are normalized on the original system's mass matrix, then

$$\boldsymbol{M}_{EE} = \boldsymbol{I}, \tag{4.35}$$

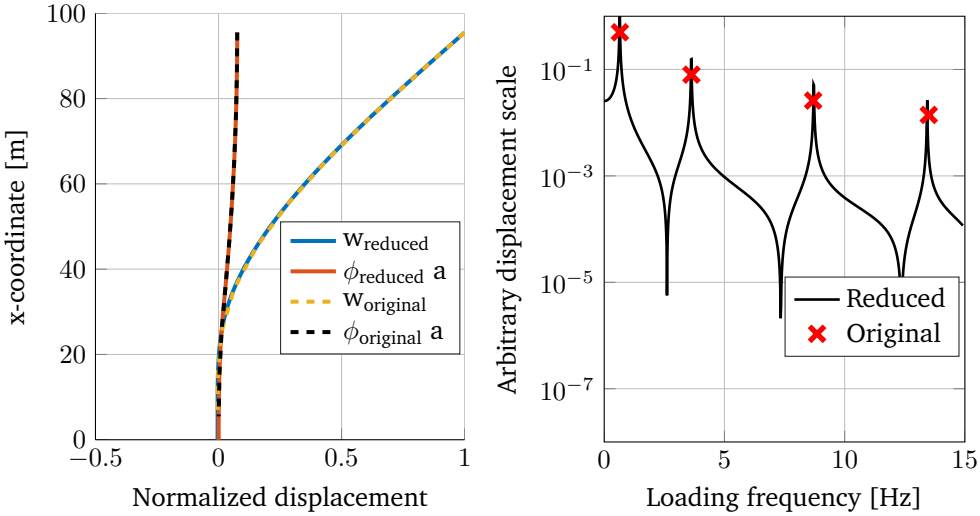

Figure 4.5: In the left figure, the static response of the reduced system and original beam model due to a static lateral load are visualised. In the right figure, the dynamic undamped response to a harmonic lateral loading of the reduced system is visualized, the eigenfrequencies of the original system are shown for comparison.

where $\boldsymbol{I}$ is the identity matrix and

$$\boldsymbol{K}_{EE} = \boldsymbol{\omega}_n^{\circ 2} \boldsymbol{M}_{EE} \tag{4.36}$$

where $\boldsymbol{\omega}_n^{\circ 2}$ denotes the Hadamard, or piecewise, square of vector $\boldsymbol{\omega}_n$.

The static and dynamic response of the undamped reduced system is compared with the original system. This is done for both the shell and the beam model, which yields comparable results. The comparison for the beam model can be observed in figure 4.5. The static response of the reduced systems due to loading at the interface shows an exact match with the original system up to calculation precision, this is expected based on the reduced system's formulation. The eigenfrequencies of the original system show a minor deviation from resonance frequencies of the undamped reduced system. The maximum deviation for the first 6 eigenfrequencies was found to be~0.5%. A small deviation in the reduced system's eigenfrequencies is to be expected as only a limited number of modes are taken into consideration, this is found to be acceptable for further calculations.

The reduced systems damping matrix is determined directly from the reduced

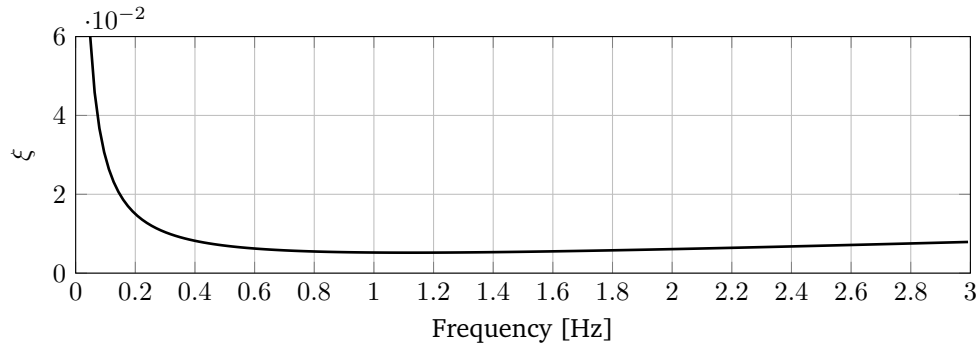

Figure 4.6: Damping ratio as a function of frequency.

mass and stiffness matrices, assuming Rayleigh damping. Therefore,

$$\tilde{\boldsymbol{C}} = \alpha\tilde{\mathbf{M}} + \beta\tilde{\boldsymbol{K}} \tag{4.37}$$

where α and β are tunable parameters. As a function of frequency, the damping on the monopile in the research models is defined as in figure 4.6, where ξ is the ratio of the system's damping relative to the critical damping. Wave loading is incorporated as

$$\tilde{\boldsymbol{p}} = \int_0^L \int_0^{2\pi} \boldsymbol{R}^T \boldsymbol{p} x d\theta, \tag{4.38}$$

where $\boldsymbol{p}$ is determined as in chapter 5.

Chapter 5

Environmental loading

In this chapter the relevant theoretical background of environmental load analysis on offshore wind turbine support structures is provided. Furthermore, the implementation of the environmental loading within the research models is outlined. In this study two types of environmental loads are considered: water wave loads and wind loads, which are determined using diffraction theory and blade element momentum theory, respectively.

5.1 Theoretical background of wave loading

5.1.1 Introduction

This section provides the theoretical framework of ocean waves and their action on offshore monopile support structures. Waves cause time-varying loading on offshore structures. The assessment of wave action is essential in the determination of the lifetime loading on an offshore wind turbine. The energy distribution over frequency and period of ocean water waves originating from various sources is shown in figure 5.1. In order to determine the lifetime loading on an offshore wind turbine, waves generated by the interaction between the wind and the free water surface are most important [32]. These types of waves are, in short, referred to as wind waves. Wind waves are important because a high amount of energy is present in the frequency range between 0.1-1 Hz, which typically coincides with the first eigen-frequency of an offshore wind turbine. Wind waves can be further classified in the following manner. Waves with periods longer then 1/4 s are dominated by gravity

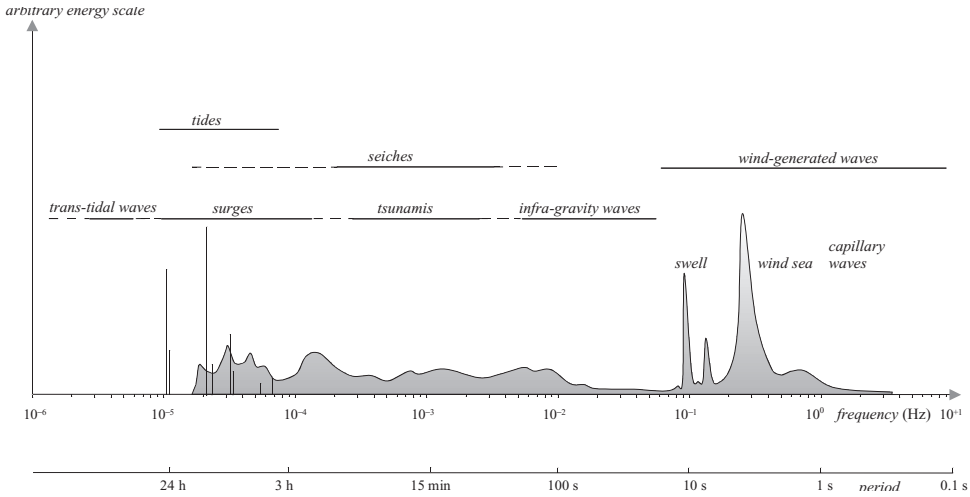

Figure 5.1: Frequencies and periods of the vertical motion of the ocean surface [33].

and referred to as surface-gravity waves. If the waves are generated by the local wind, they are irregular, short crested and are called wind sea waves. When the waves leave their area of creation, they take on a regular and long crested appearance and are called swell waves. Waves with periods shorter then 1/4 s are affected by surface tension and referred to as capillary waves. Capillary forces generate small ripples and cause sea spray on wave impact but are generally considered to be negligible when dealing with large offshore structure.

5.1.2 Harmonic wave components

While waves may be irregular in nature, they can be seen as a superposition of regular harmonic wave components [34]. Each harmonic wave component has it's own direction of propagation, amplitude, period and length. The set of components necessary to model a sea state at a certain location can be derived from a wave spectrum. A harmonic wave with length λ, height H, and period T, which propagates over the free water surface in positive x direction at a distance d from the mudline, is visualized in figure 5.2. The surface elevation $\zeta(x,t)$ of the wave is described by

$$\zeta(x,t) = \zeta_a \sin(kx - \omega t), \tag{5.1}$$

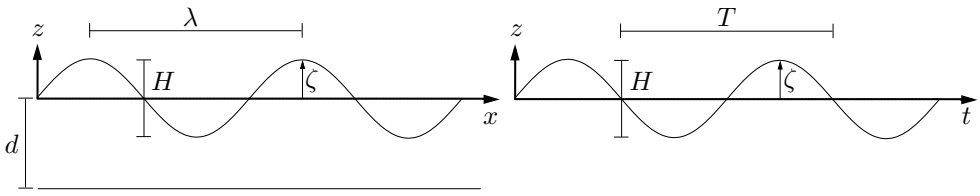

(a) Harmonic wave in space **(b)** Harmonic wave in time

Figure 5.2: Harmonic wave definitions

where the wave's amplitude, wave number and frequency are respectively given by

$$\zeta_a = \frac{H}{2}, \tag{5.2a}$$

$$k = \frac{2\pi}{\lambda}, \tag{5.2b}$$

$$\omega = \frac{2\pi}{T}. \tag{5.2c}$$

Now that the components of a harmonic wave are defined, it is shown how they can be used in order to obtain a wave field based on a statistical description.

5.1.3 Statistical description of water movements

In the design process of offshore wind turbines it is assumed that, during the entire life span of the structure, the water movement can be split up in a number of stationary periods of 3-6 hours. These periods are called sea-states. For each sea-state the vertical water movement at a given position is schematised as a stationary Gaussian process with a mean equal to zero [35]. In practice, for locations in the North Sea, often an energy distribution according to the JONSWAP spectrum [36] is adopted [5]. The JONSWAP spectrum is given by

$$S(\omega) = \frac{\alpha g^2}{\omega^5} \exp\left(-\frac{5}{4}\frac{\omega_p^4}{\omega^4}\right) \gamma^{\exp\left(-\frac{1}{2}\left(\frac{\omega-\omega_p}{\sigma\omega_p}\right)^2\right)}, \tag{5.3}$$

where the generalized Philips' constant α, wave frequency f, spectral peak frequency f_p and spectral width parameter σ are given by

$$\alpha = 5\pi^4 \left(\frac{H_s^2 \omega_p^4}{(2\pi)^4 g^2} \left(1 - 0.287 \ln(\gamma)\right) \right), \tag{5.4a}$$

$$\omega_p = \frac{2\pi}{T_p}. \tag{5.4b}$$

The peak enhancement factor γ is chosen between 1 and 5, depending on the ratio of T_p to $\sqrt{H_s}$, where H_s is the significant wave height. If γ is chosen equal to 1, the JONSWAP spectrum reduces to the Pierson-Moskowitz spectrum [37]. The difference between both spectra is in the development stage of the sea. The JONSWAP spectrum is used for young sea states, while the Pierson-Moskowitz spectrum is used for fully developed sea states. Both the JONSWAP and the Pierson-Moskowitz spectrum are single peaked spectra and account for wind generated waves. A double peaked spectrum such as the Ochi-Hubble spectrum [38] or the Torsethaugen spectrum [39] can be considered when a significant swell contribution is expected.

5.1.4 Velocity potential of an undisturbed wave

Wind waves are often described using a velocity potential function Φ. This velocity potential is defined such that the derivative of Φ in a spatial direction equals the particle velocity in that direction. In this study Airy wave theory [40] is used to describe the propagation of water waves. This theory assumes that the fluid layer has a uniform depth and that the fluid flow is non-viscous, incompressible, irrational and that the fluid is homogeneous. Since the fluid is incompressible, the velocity potential function must satisfy the Laplace equation.

$$\nabla^2 \Phi = 0 \tag{5.5}$$

The velocity potential function must also satisfy additional boundary conditions. For an undisturbed wave, two boundary conditions are specified, one at the sea bed and one at the free surface. At the seabed, the velocity potential in the vertical direction must equal zero.

$$\frac{\partial \Phi}{\partial z} = 0 \quad \text{at} \quad z = -d \tag{5.6}$$

The free surface boundary condition is derived from the linearised Bernoulli's equation and states that the pressure in the fluid at the free surface must equal the atmospheric pressure. The atmospheric pressure can be omitted from the equation,

which results in

$$\frac{\partial \Phi}{\partial t} + g\zeta = 0 \quad \text{at} \quad z = 0, \tag{5.7}$$

assuming that ζ is small relative to d. Resulting from equations 5.5-5.7, the velocity potential of an undisturbed wave can be written as

$$\Phi^{(i)} = \Re\left(-\frac{g\zeta_a}{\omega} \frac{\cosh(k(d+z))}{\cosh(kd)} e^{\mathrm{i}(kx-\omega t)} \right). \tag{5.8}$$

5.1.5 Diffraction theory

Diffraction theory will be used to determine the pressure on the offshore monopile support structure induced by incident and radiated waves in this study. A solution for the theoretical problem of harmonic water waves diffraction from a circular cylinder is presented and experimentally verified in [41]. In this solution the assumptions of Airy's wave theory were used. An overview of the solution is presented in the following.

Consider a cylinder with radius a which extends from the bottom through the free surface of a fluid domain as visualized in figure 5.3. The cylinder is subjected to wave action originating from a single direction. Locations in the fluid domain and on the cylinder can be expressed in two coordinate systems. The first coordinate system is Cartesian and consists of the x, y and z axis, where the x and y axes coincide with the zero plane of the free surface, the x axis points in the propagation direction of the waves, the y axis points in outward direction from the figure and the z axis coincides with the centreline of the cylinder. The second coordinate system is polar and consist of the z, θ and r coordinates. Here r is the radial distance from the cylinder's centreline and θ is the angle to the negative x axis. The velocity potential of the incident wave is given by equation 5.8. In order to solve the radiation problem, the expression for the velocity potential function of the incident wave, given by equation 5.8, is transformed to polar coordinates by means of the following infinite series:

$$\Phi^{(i)} = \Re\left(-\frac{g\zeta_a}{\omega} \frac{\cosh(k(d+z))}{\cosh(kd)} \left[\mathrm{J}_0(kr) + 2\sum_{n=1}^{\infty} \mathrm{i}^n \mathrm{J}_n(kr)\cos(n\theta) \right] \right), \tag{5.9}$$

where J_α denotes the Bessel function of first kind. The radiated wave is assumed to move in outward direction r, symmetrically with respect to θ:

$$\Phi_n^{(r)} = \Re\left(C_n e^{-\mathrm{i}\omega t} \left[\mathrm{J}_n(kr) + \mathrm{i}\mathrm{Y}_n(kr) \right] \cos(n\theta) \right), \tag{5.10}$$

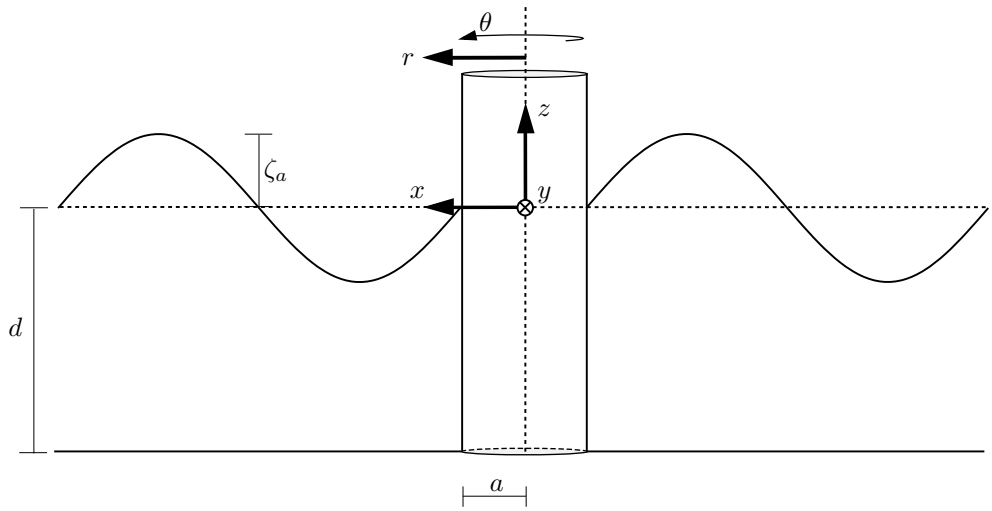

Figure 5.3: Cylinder subjected to wave action.

where Y_α is the Bessel function of the second kind. Note that the wave vanishes at $r = \infty$. The total velocity potential can be taken by superposition of the incident wave potential $\Phi^{(i)}$ and an infinite series of radiated waves $\Phi^{(r)}$. The coefficients C_n are determined such that the fluid velocity normal to the cylinder equals zero at the cylinder's surface. The resulting formulation of the total potential function, as derived in [42], can be written as

$$\Phi = \Re\left(\frac{g\zeta_a}{\omega}e^{-\mathrm{i}\omega t}\frac{\cosh(k(d+z))}{\cosh(kd)}\left[\mathrm{J}_0(kr) - \frac{\mathrm{J}_0'(ka)}{\mathrm{H}_0^{(2)\prime}(ka)}\mathrm{H}_0^{(2)}(kr)\right.\right. \tag{5.11}$$
$$\left.\left. +2\sum_{n=1}^{\infty}\mathrm{i}^n\left(\mathrm{J}_n(kr) - \frac{\mathrm{J}_n'(ka)}{\mathrm{H}_n^{(2)\prime}(ka)}\mathrm{H}_n^{(2)}(kr)\right)\cos(n\theta)\right]\right),$$

where $\mathrm{H}_\alpha^{(2)}$ is the Hankel function of the second kind, which equals $\mathrm{J}_\alpha - \mathrm{i}\mathrm{Y}_\alpha$.

A contour plot of an example calculation of different components of the velocity potential at the free surface around a cylinder is given in figure 5.4. In the example calculation the cylinder is situated in the center of the xy-plane and has a diameter of 3.9 m. The wave is travelling in negative x direction, has a wave number of 2 m^{-1}

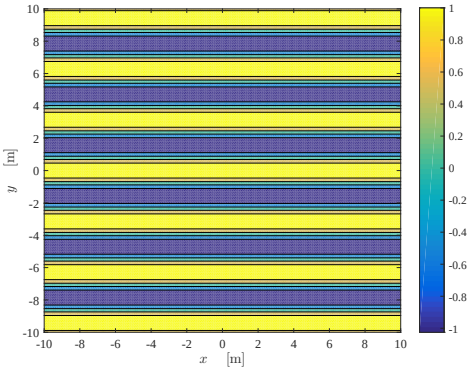

(a) Velocity potential of the incident wave.

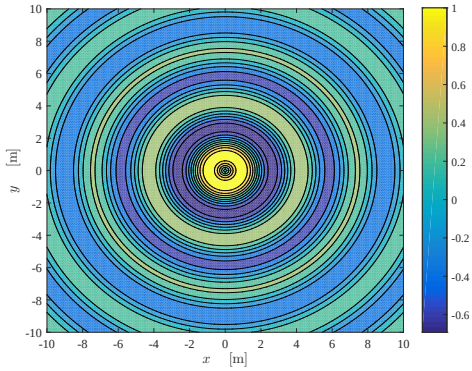

(b) Velocity potential of a single radiated wave.

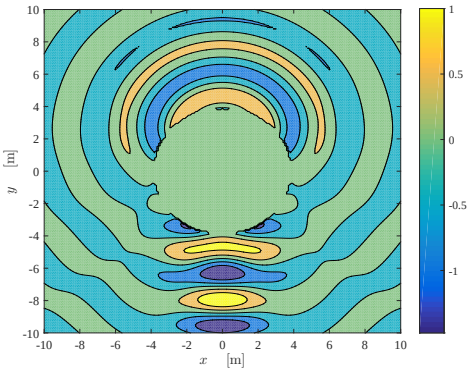

(c) Velocity potential of all radiated waves around a cylinder.

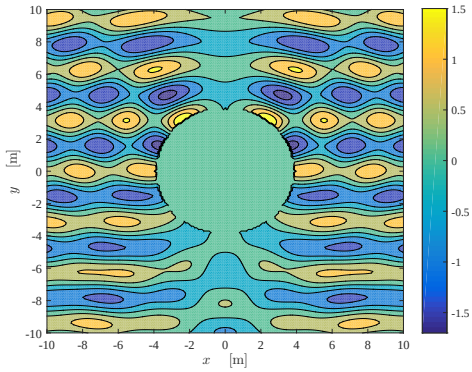

(d) Total velocity potential around a cylinder.

Figure 5.4: Contour plots of the velocity potential of: **(a)** an incident wave, **(b)** a single radiated wave, **(c)** all radiated waves around a cylinder and **(d)** the incident and all radiated waves around a cylinder. For this calculation a cylinder with a radius of 3.9 m, located in the center of the xy-plane and an incident wave with a wave number equal to 2 m^{-1}, which is travelling in negative x direction are used.

and an amplitude of 1 m.

The pressure distribution on the cylinder can be calculated using the linearised Bernoulli equation.

$$p = \rho \frac{\partial \Phi}{\partial t} + \rho g \zeta \tag{5.12}$$

5.2 Theoretical background of wind action

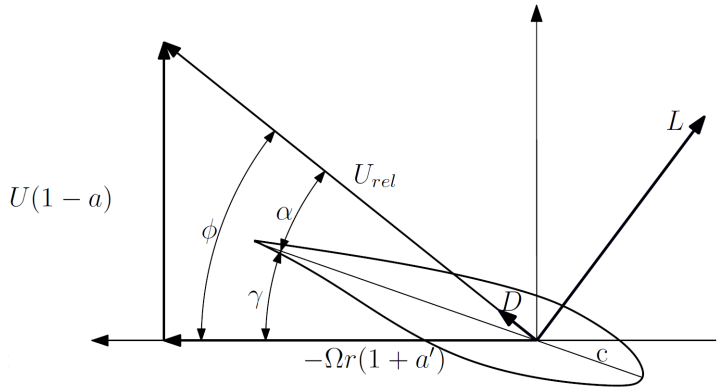

Figure 5.5: Local forces on an aerofoil [43].

In the industry, wind loading on the rotor of a wind turbine is calculated by means of the Blade Element Momentum (BEM) theory, which is extensively described in [44] and is a combination of momentum theory and blade element theory. The change in momentum of a wind flow through the rotor plane is calculated using momentum conservation. It is hereby assumed that the flow is incompressible and the rotor acts as an actuator disk. The later assumption is generally only valid near the blade tip but is used for the entire rotor plane nevertheless. On each blade element, the lift and drag forces can be calculated based on the relative wind velocity

$$dF_L = \frac{1}{2}\rho_a C_L U_{rel}^2 c, \tag{5.13a}$$

$$dF_D = \frac{1}{2}\rho_a C_D U_{rel}^2 c, \tag{5.13b}$$

$$dF = dF_L cos\phi + dF_D sin\phi, \tag{5.13c}$$

where ρ_a is the density of air, C_L and C_D are the lift and drag constants respectively, U_{rel} is the relative wind velocity, c is the length of the cord and ϕ is the inflow angle. The relative wind velocity is calculated by

$$U_{rel} = \sqrt{\big(U(1-a)\big)^2 + \big(\Omega r(1+a')\big)}, \tag{5.14}$$

where U is the ambient wind velocity at the location of the aerofoil, a and a' are axial and tangential induction factors, Ω is the angular velocity and r is the distance from the hub. Note that the induction factors should not be confused with the radius of a cylinder or monopile, which is also denoted with a throughout the rest of this thesis. A schematic overview of local forces on an aerofoil can be observed in figure 5.5.

5.3 Application in the research models: Calculating wave and wind loading

5.3.1 Calculation of wave loading

The calculation process of wave loading for this study can be observed in figure 5.6. For the various design load cases considered in this thesis, wave loads on the monopile surface are calculated. First a wave generation tool, SWAG, which abbreviates for Siemens WAve Generator, is used to generate an undisturbed wave field. SWAG calculates a JONSWAP wave spectrum based on H_s and T_p. From this wave spectrum the complex amplitudes of K harmonic wave contributions are determined in space and time, where K depends on the simulation but roughly equals 10000. From SWAG, the amplitude, frequency and wave number of the velocity potential function of each contributing wave is extracted at a point A. The point A represents the point on the circumference of the monopile where the undisturbed wave makes first contact with the monopile and is positioned at $\theta = 0$, $r = a$ and $z = 0$ in the polar coordinate system defined in section 5.1.5. The location of A is visualized in figure 5.7. According to diffraction theory, the total velocity potential is calculated using the data extracted from SWAG for each incoming wave contribution. Note that the monopile is considered to be rigid when the velocity potential functions are determined.

For convenience, the velocity potential function and the pressure on the cylinder are split up in terms of n. As derived from equation 5.11 this can be done as

$$\Phi_0 = \Re\left(\frac{g\zeta_a}{\omega} e^{-\mathrm{i}\omega t} \frac{\cosh(k(d+z))}{\cosh(kd)} \left[\mathrm{J}_0(ka) - \frac{\mathrm{J}_0'(ka)}{\mathrm{H}_0^{(2)\prime}(ka)} \mathrm{H}_0^{(2)}(ka)\right]\right) \tag{5.15}$$

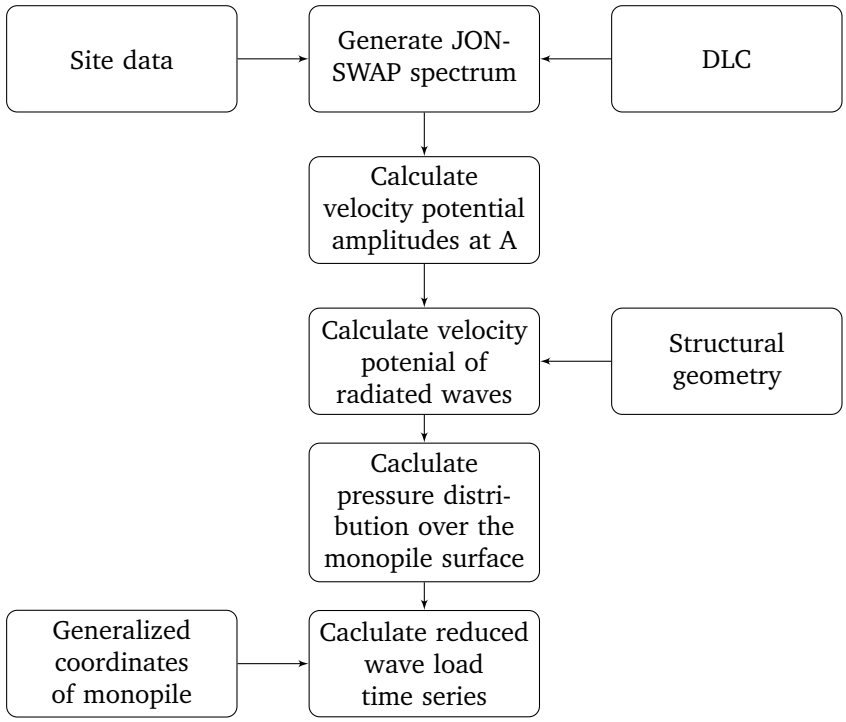

Figure 5.6: Flowchart for the generation of wave loading for the research models.

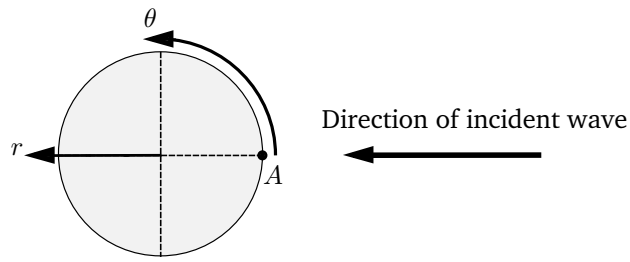

Figure 5.7: Position of point A.

and for $n > 0$

$$\Phi_n = \Re\left(2\mathrm{i}^n \frac{g\zeta_a}{\omega} e^{-\mathrm{i}\omega t} \frac{\cosh(k(d+z))}{\cosh(kd)} \left[\mathrm{J}_n(ka) - \frac{\mathrm{J}'_n(ka)}{\mathrm{H}^{(2)\prime}_n(ka)} \mathrm{H}^{(2)}_n(ka)\right] \cos(n\theta)\right). \tag{5.16}$$

When using a circular cylindrical shell description of the monopile, for all n, the radial loading p_{nz} is determined using

$$p_{nz} = \rho \frac{\partial \Phi_n}{\partial t} + \rho g \zeta. \tag{5.17}$$

When using a beam model to describe the monopile, only the term with $n = 1$ results in a non-zero resultant force on the cylinder. The total resultant force is thus given by

$$F = \int_0^{2\pi} p_{1z} \cos(\theta) a d\theta. \tag{5.18}$$

For both descriptions of the monopile a time series of the water wave loading is created. The loading is then projected onto the monopiles generalized coordinates following section 4.5, which creates a time series of reduced load vectors. These reduced load vectors will be input for the numerical time-domain analyses of the wind turbine support structure using Siemens' BHawC.

In this study three sea states are considered, using $H_s = 1.13$ and $T_p = 5.89$ for the first sea state, $H_s = 3.08$ and $T_p = 8.45$ for the second sea state and $H_s = 6.02$ and $T_p = 9.64$ for the third sea state. The third sea state obviously contains more energy then the first sea state, however, the energy distribution as a function of frequency differs between the sea states. This is shown in figure 5.8 where the normalized variance density of the three spectra is calculated. From figure 5.8 it is noted that the majority of the wave energy is located below the first eigenfrequency of the offshore wind turbine. Regardless of the wave spectrum, the distribution of the wave loading over the various circumferential wave numbers n can be determined based on the monopile's geometry. In figure 5.9 the wave height independent norm of the pressure at the free water surface was calculated for $n = 1$ to 6 using

$$\hat{p}_n = \left\| 2\rho \mathrm{i}^n \left[\mathrm{J}_n(ka) - \frac{\mathrm{J}'_n(ka)}{\mathrm{H}^{(2)}_n(ka)} \mathrm{H}^{(2)}_n(ka)\right] \right\|. \tag{5.19}$$

Figure 5.9 on its own suggests a significant wave loading on the modes $n > 1$. However, from figure 5.8 it can be observed that notably more wave energy is present

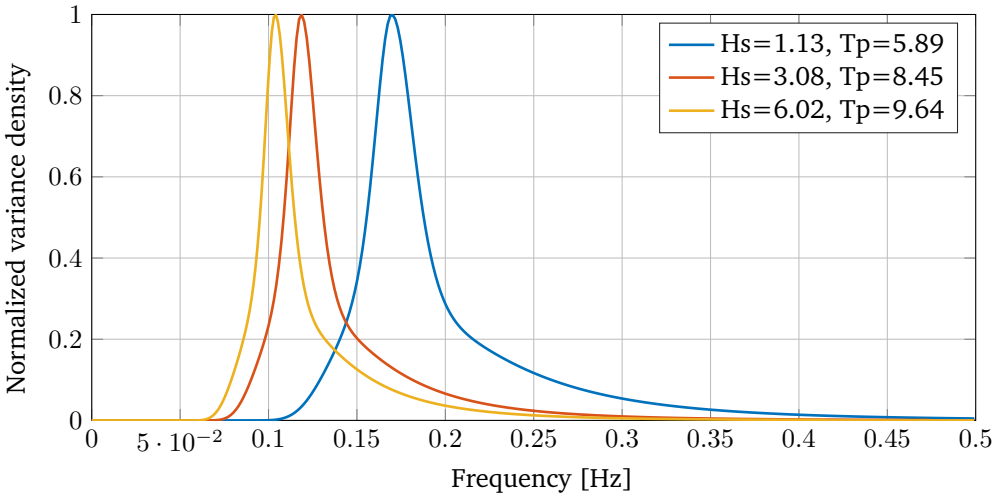

Figure 5.8: Three normalized variance density spectra for various values of H_s and T_p.

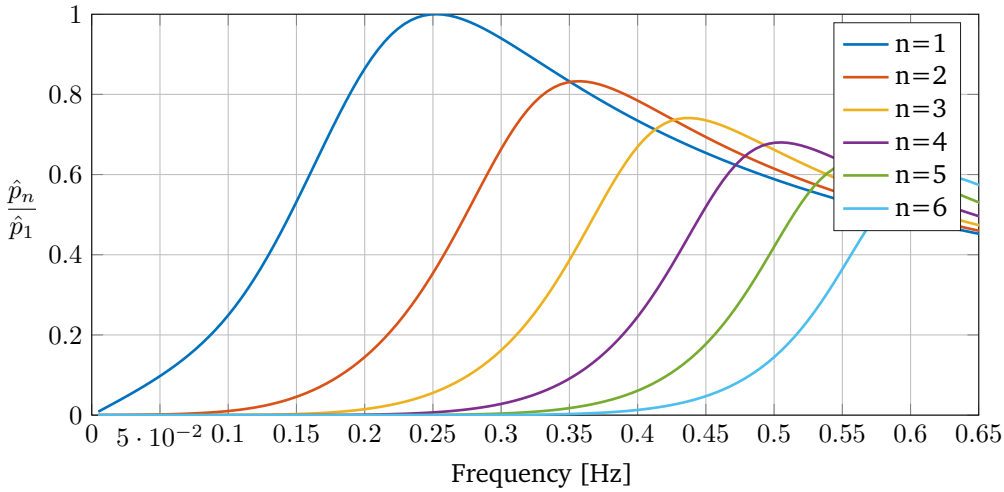

Figure 5.9: Distribution of the wave loading over the circumferential wave numbers as a function of frequency.

in the region where $\hat{p}_1$ peaks, which equals 0.25 Hz, compared to the regions where $\hat{p}_2$ to $\hat{p}_6$ peak, which are approximately 0.35 Hz, 0.43 Hz, 0.5 Hz 0.57 Hz and 0.6 Hz. Therefore, it is expected that the beam modes, with $n = 1$, will be significantly more excited then the self balancing modes, with $n > 1$, by the wave loading.

5.3.2 Applicability of diffraction theory

In practice, the Morison equation [45] is often used to calculate wave loading on offshore wind turbines [5]. The Morison equation displays an empirical relationship, in terms of a mass coefficient C_M and a drag coefficient C_D, to calculate wave forces on a small submerged cylinder. This relationship involves an inertia force and a viscous drag force on the submerged cylinder and assumes that the object is small such that it does not disturb the incident wave field. However, as the diameter of the cylinder becomes large compared to the incident wavelength, the Morison equation does not apply and a diffraction theory must be used. In this case, viscous drag forces are assumed to be insignificant for smooth cylinders and the inertia forces predominate [46]. The dominance of the inertia force over the drag force can be expressed in terms of the Keulegang Carpenter number KC, which is defined as

$$KC = 2\pi \frac{x_a}{D}, \tag{5.20}$$

where x_a is the horizontal water displacement amplitude and D is the diameter of the cylinder. For low values of $KC\,(KC < 3)$, the inertia force is dominant and drag can be neglected [47]. For cylinders with small values of $D/\lambda\,\big(D/\lambda < 0.2\big)$ the wave's total force on the cylinder can be calculated with the Morison equation using $C_M = 2$. For higher values of D/λ the Morison equation does not suffice and a diffraction theory is required [48]. Note that for low values of D/λ a diffraction theory is also applicable, with an added benefit that the pressure distribution along the circumference is also predicted.

For the wave loading considered in this study, the dominance of the inertial force over the drag force is shown through calculation of the overturning moment at the mudline of the monopile by means of the Morison equation. The relative contribution of inertia and drag to the total overturning moment as a function of time can be observed in figure 5.10. While the drag component is arguably not negligible, especially for the third sea state, it is assumed that for the purpose of this study, diffraction theory will suffice when calculating the wave loading.

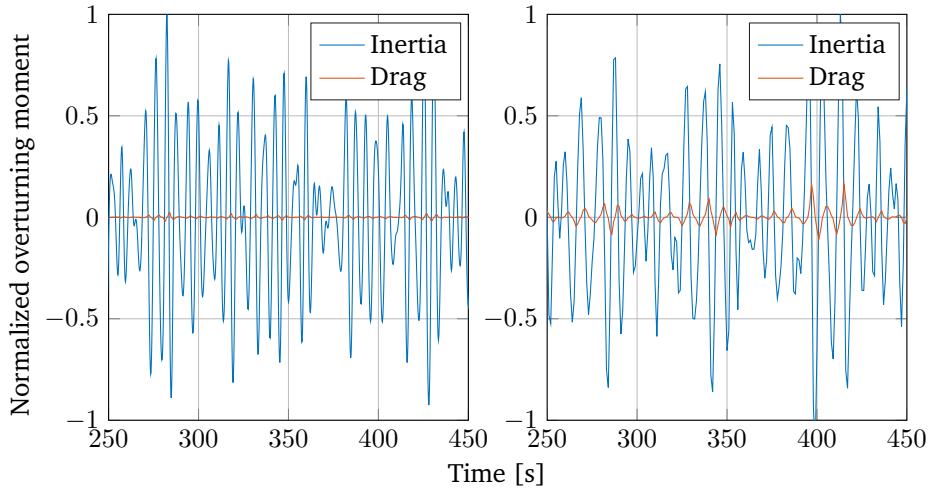

Figure 5.10: The inertia and drag component of the overturning moment at the mudline for the first (left) and third (right) sea state, as predicted by the Morison equation.

5.3.3 Calculation of wind loading

In this study, wind loading is calculated using Siemens' BHawC. Using BEM theory, BHawC calculates the aerodynamic loading originating from a mean wind velocity and a turbulence model. Without further elaboration it is stated that BHawC is able to incorporate controller effects, can deal with a skewed and unsteady inflow, will account for dynamic stall and tower shadowing effects, corrects for high induction values and includes a correction for Prandtl's tip loss. The wave spectra, as presented in figure 5.8 are resulted from a mean wind speed at hub height of 7, 16 and 21 m/s respectively. The fast Fourier transform (FFT) of the force in the turbine's shaft due to the wind loading and controller effects can be observed in figure 5.11. It is observed that the peaks between 0.13 Hz and 0.17 Hz, depending on the mean wind speed. A weak decreasing trend in the force as a function of frequency can be observed in the higher frequency bands.

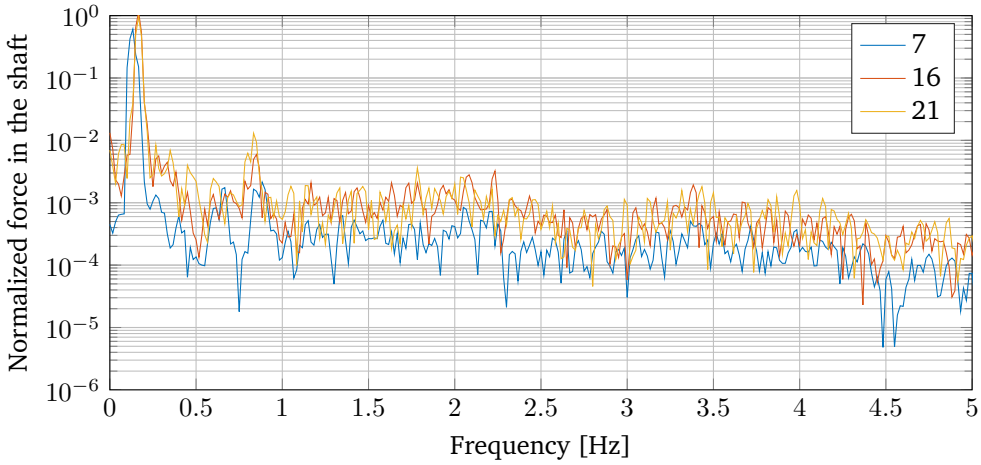

Figure 5.11: FFT of the force in the turbine's shaft due to wind loading and controller dynamics.

Chapter 6

Time-domain simulations

In order to gain insight in the first research objective, several time-domain simulations are performed with the beam and shell models coupled to Siemens' BHawC. The dynamic behaviour of both models is analysed for various design load cases. It is then identified how much the shell deformations affect the stress levels within the monopile's shell.

6.1 Overview of the models, load cases and limitations

In the preceding chapters, all relevant theory governing the research models has been discussed. The implementation of the theory in the models was also presented. Both foundation models are coupled to BHawC, in which the tower and RNA are described with Timoshenko beam elements. The monopile foundation is included as a superelement, which is connected to the lowest node of the tower, located at the interface level. For the first model, which is referred to as the beam model, the monopile foundation is represented by a superelement derived using Timoshenko's theory for beams. In the second model, which is referred to as the shell model, Flügge's relations for circular cylindrical shells are used to define the superelement monopile foundation. In both models, the monopile is assumed to be of uniform diameter and wall-thickness, which are respectively given by 7.8 m and 0.086 m. This represents a monopile with a flange connection to the tower instead of a transition piece. The monopile's embedded length within the soil is 36.5 m, the water depth is 40 m and the interface level is located at 17 m above the mean sea

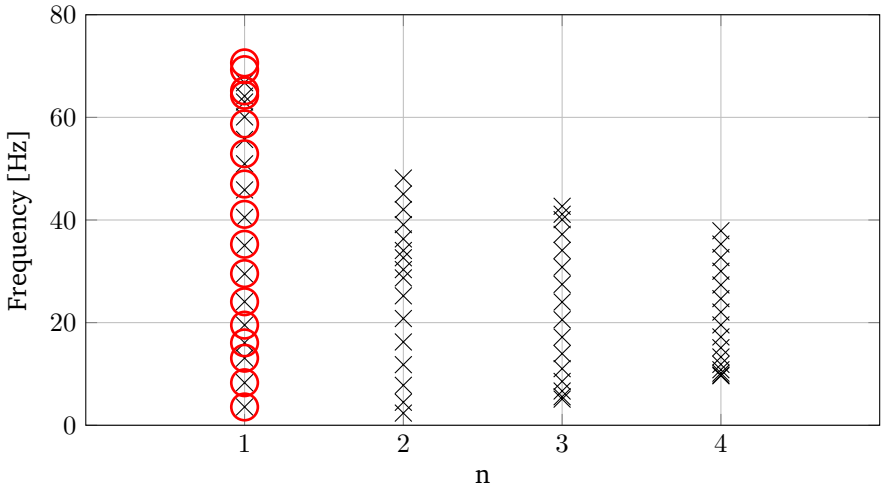

Figure 6.1: Comparison of the eigenfrequencies of the fixed-interface vibration modes. The eigenfrequencies governing the shell model are given by black $\times$'s while for the beam model the eigenfrequencies are visualised as red circles.

level. Soil-structure interaction characteristics are derived using the circumferential wavenumber method as per chapter 3.

In the foundation models, added mass has been accounted for by increasing the monopile's density. This is a significant simplification. Nevertheless, this method is generally accepted by the industry. In this method, the mass of all the fluid contained within the monopile and the fluid outside the monopile within a certain radius is effectively added to the mass of the monopile. This is believed to be less realistic when dealing with shell deformation behaviour as (i) added mass is frequency dependant and shell deformation behaviour is excited by a different frequency band then the global bending deformations, and (ii) the modes governing the shell deformations do not displace the cylinder's centreline. A more formal approach to this problem is to take note of the Helmholtz equation as in [49], however this is not considered in this study.

The substructuring approach, where the tower is connected to the monopile at a single node, effectively eliminates all coupling of the wind loading and controller effects to the monopile's shell deformations. It can be argued that the energy available in the higher frequency bands of the loading spectrum due to the wind and controller dynamics is able to excite shell deformations in the monopile. A spectrum

	u_{mean} [ms^{-1}]	H_s [m]	$T_p[s]$
Condition 1	7	1.13	5.89
Condition 2	16	3.08	8.45
Condition 3	21	6.02	9.64

Table 6.1: Summary of environmental conditions.

can be observed in figure 5.11. As is concluded in chapter 2, the shell modes will only be excited by loading which has a corresponding circumferential wave number. It is assumed that the loading terms originating from the wind field and controller dynamics with circumferential wavenumbers of $n > 1$ are relatively small to those corresponding to $n = 1$. Since several stiff flanges are present between hub height and connection of the tower to the monopile, it is assumed that no loading with a circumferential order of $n > 1$ will act on the monopile at the interface level.

A visual overview of the eigenfrequencies of the fixed-interface vibration modes is given in figure 6.1, their nummerical values are listed in appendix C. The orthogonality of the modes is checked by means of a Modal Assurance Criterion, which can be observed in appendix D. The lowest three eigenfrequencies of the modes with $n > 1$ are given by 2.37 Hz for $n = 2$, 4.49 Hz for $n = 2$ and 5.10 Hz for $n = 3$. It is noted that these frequencies are significantly higher than the first eigenfrequency governing the entire wind turbines global bending behaviour, which equals 0.255 Hz. It additionally is observed that, for increasing n, the lowest eigenfrequencies per n are spaced more closely together and that, for increasing m (numbering of the eigenfrequencies for a given n), the lowest eigenfrequency per m shifts towards higher n. Both observations are in agreement with literature [12, 17].

The two design load cases that are typically most governing with respect to the fatigue limit state are given as a turbine in power production and a turbine which is idling. The difference between the two load cases is in the behaviour of the rotor. In the case of power production, the rotor will be rotating which introduces aerodynamic damping to the wind turbine's motion in the fore-aft direction. In the idling load case, the rotor idles and thus little additional damping is introduced. It is therefore expected that more global bending deformations will be present for the idling load case. This implies that the shell deformations will be relatively less pronounced. Hence, the design load case under investigation is chosen as a wind turbine in power production. For this load case it is assumed that the wind and waves are aligned, which is again chosen based on the aerodynamic damping. Three environmental conditions, defined by the mean wind speed at hub height and the sea state, are

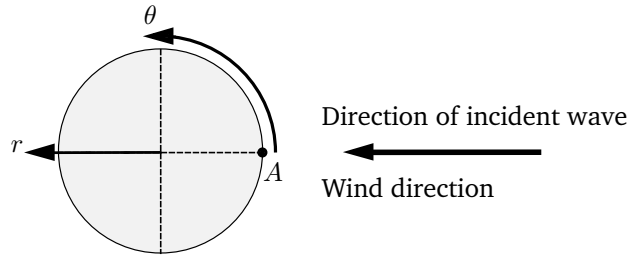

Figure 6.2: Position of circumferential coordinate A.

considered. These were previously discussed in section 5.3, the relevant parameters are summarised in table 6.1.

6.2 Results

It was found that due to all three conditions, the relative influence of the shell deformations on the monopile's stress levels was comparable. Here, the response to condition 2 will be discussed in detail. This is done by (i) analysis of the resulting axial stress at the mudline in the time and frequency domain, (ii) analysis of the envelopes of the axial stress distributions over the axial coordinate, and (iii) analysis of the resulting von Mises stresses over the monopile's entire surface, based on the standard deviation of the monopile's generalized coordinates. If was found that the predicted motion perpendicular to the loading direction was at least an order of magnitude smaller then the predicted motion in the direction aligned with the loading. Additionally the torsional and vertical degree of freedom had a negligible influence on the monopile's internal stresses.

Axial stress near the mudline

The maximum total stress levels predicted by both models occur near the mudline at a circumferential coordinate A. The position of A relative to the loading direction on the circumference of the monopile is visualised in figure 6.2. Here primarily stresses in the axial direction occur. In the following, the axial stress σ_{xx} at the centreline of the monopile's shell at this location is analysed. This is done separately for the beam model, as well as the contribution of the modes governing the different circumferential wavenumbers n for the shell model. Figure 6.3 shows σ_{xx} as a function of time for $n = 1$ to $n = 4$ as predicted by the shell model. In figure 6.4,

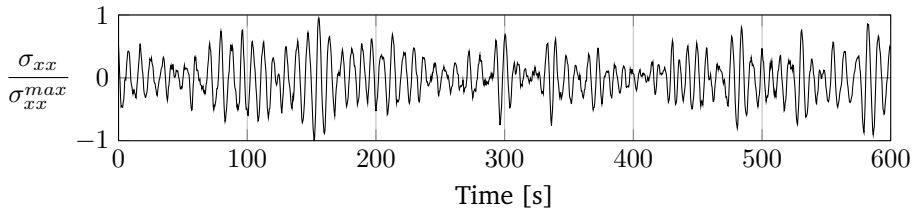

(a) Shell $n = 1$

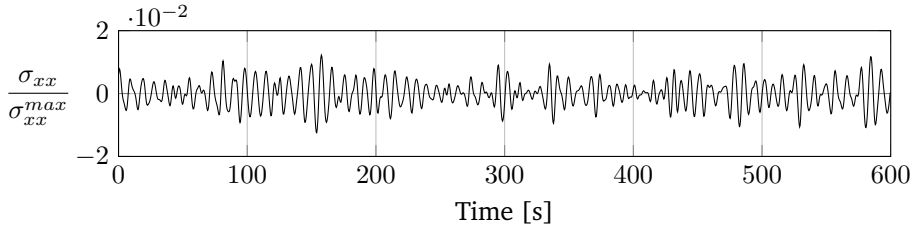

(b) Shell $n = 2$

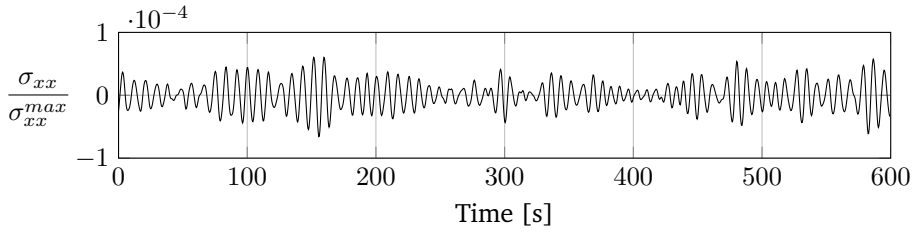

(c) Shell $n = 3$

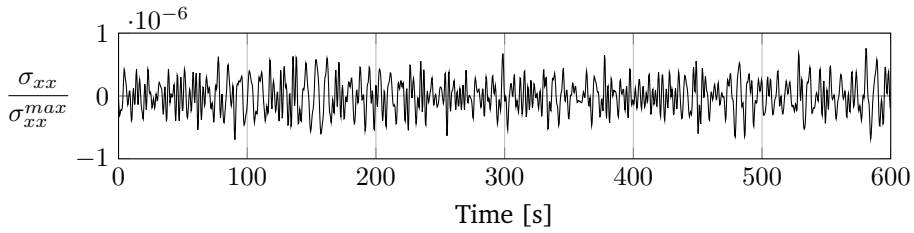

(d) Shell $n = 4$

Figure 6.3: Time signals of the shell model's predictions of the axial stress at location A in the centre of the shell due to condition 2. All values are presented relative to the maximum axial stress as obtained for $n = 1$.

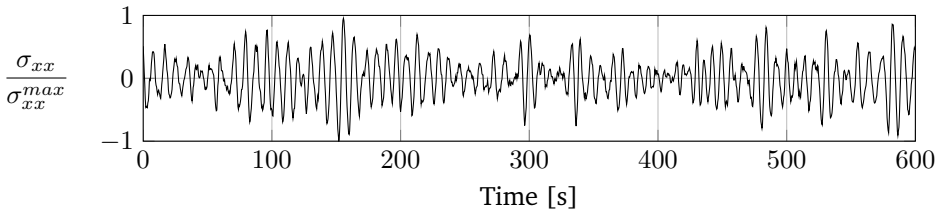

(a) Beam

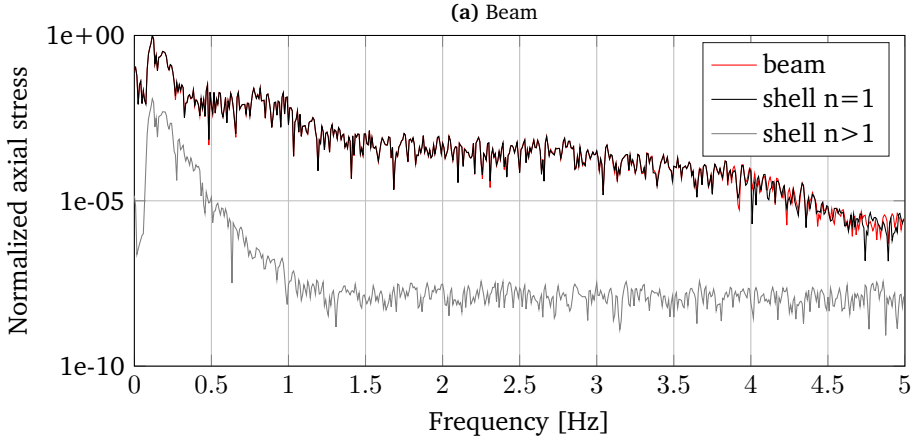

(b) Shell, beam

Figure 6.4: Time signal **(a)** of the stress as predicted by the beam model. FFT of the predicted stress by both the shell and beam model **(b)**. All predictions are made at location A in the centre of the shell due to condition 2 and are presented relative to the maximum axial stress as found for $n = 1$ using the shell model.

the predictions by the beam model are shown, while additionally the FFT's of (i) σ_{xx} as predicted by the beam model, (ii) σ_{xx} due to all modes with $n = 1$, as predicted by the shell model, and (iii) σ_{xx} due to all modes with $n > 1$, as predicted by the shell model are shown. Note that all values are normalised with respect to the maximum stress that occurred for the shell model due to the modes corresponding with $n = 1$. For the beam model and for the modes governing $n = 1$ for the shell model, it was found that the stresses do not oscillate around zero. This is due to the, somewhat, constant wind loading on the rotor. Since for the fatigue limit state the stress oscillations are governing, the mean has been subtracted from all time signals.

In figures 6.3 and 6.4 it is visible that the shell model and the beam model are in excellent agreement on the stress levels governing the global bending behaviour of the monopile. It can additionally be seen that the contribution of the shell deformations to the stresses in the axial direction at the investigated location are minor. Due to condition 2, the contribution of shell deformations to the total axial stress levels at the investigated location is in the order of 1%.

On an additional note, the presence of the first fore-aft global bending mode is hardly noticeable in figure 6.4 (b) due to the contribution of significant aerodynamic damping. However, in the side-to-side direction, a substantial peak is observed at the 0.25-0.26 Hz frequency band, this can be observed in figure 6.5. It is therefore expected that, if a load case with a misalignment between the incident wind and wave direction or a load case in which the turbine is idling is investigated, the contribution of shell deformations to the stress in the monopile will be of less relative importance.

Axial stress envelopes

It was found that, over the vertical direction, the maximum stresses corresponding to the shell deformations are found at different locations than the maxima of the total axial stress. Nevertheless, it is still true that, for all n, a maximum value of the axial stress due to shell modes with a circumferential wave number n is found at the same circumferential coordinate as A. Note that, for each n, there are $2n$ locations which contain the maximum axial stress amplitudes due to the corresponding modes. These locations, with the exception of circumferential coordinate A, will vary per n and follow the same circumferential distributions as the mode shapes. To keep the comparison transparent, all stresses will remain analysed at circumferential coordinate A, at the centreline of the monopile's shell. In figure 6.6 the envelopes of the axial stress due to condition 2, as predicted by the shell model, are visualised for $n = 1$ and $n = 2$. The stress as predicted by the beam model can additionally be observed. These envelopes are obtained by calculation

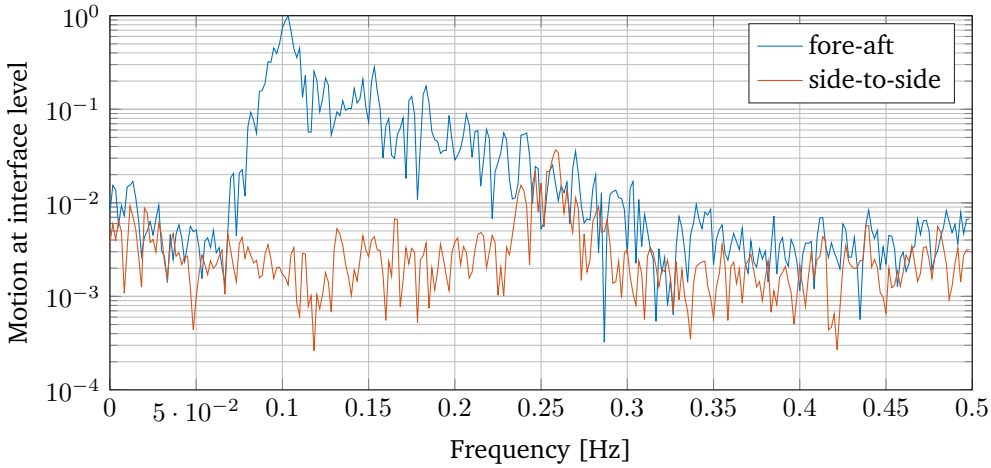

Figure 6.5: Normalized FFT of the motion at interface level in the fore-aft and side-to-side direction for the shell model under loading condition 2.

of the stress profile over the entire axial direction at circumferential coordinate A for each time step. The envelopes are then given by the extreme occurred stresses at each x-coordinate. Once again, close agreement between the beam model and the $n = 1$ modes of the shell model is found.

For $n = 2$, maxima in the stress envelope appears near the free water surface, where the wave loading is of the highest magnitude. Additionally a maximum is found at the interface level, where the modes with $n > 1$ experience a constrained boundary. It can be observed that at these locations the modes governing $n = 2$ show a higher relative contribution towards the total axial stress levels then at the location under previous investigation. At the interface level and the free water surface respectively, this contribution is in the order of 9% and 4% with respect to the axial stress due to the $n = 1$ modes at both locations.

The solutions for the modes with $n > 2$ show a much wider spread in the standard deviation of the modal participation factors, as is shown in figure 6.7. This is possibly caused by the more localized distribution of the wave loading near the free water surface. As can be observed from figure 5.9, these modes are subject to wave loading in a higher frequency band. This is due to the balance of the pressure along the monopile's circumference which is related to the wave length. For increasing

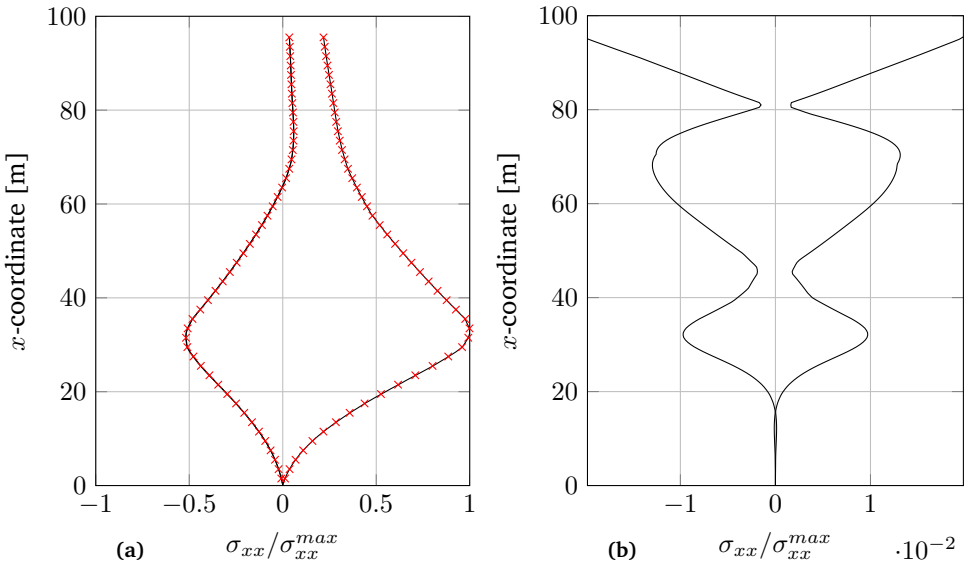

Figure 6.6: Envelopes of the axial stress distribution over the axial direction at circumferential coordinate A in the centre of the monopile's shell due to condition 2. The stress as predicted by the shell model is represented in black for $n = 1$ **(a)** and $n = 2$ **(b)**. The prediction following from the beam model is shown in red. All values are normalised with respect to the maximum axial stress for $n = 1$ as given by the shell model.

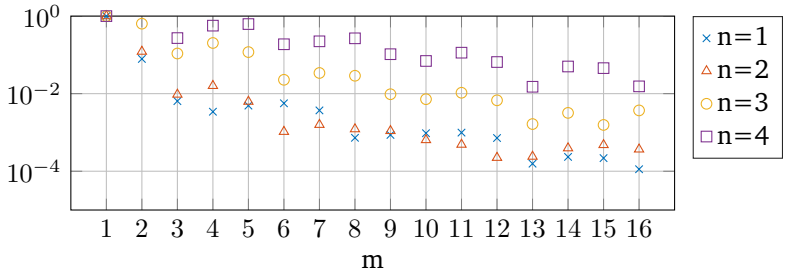

Figure 6.7: Standard deviation of the fixed-interface vibration modes' modal participation factors as predicted by the shell model due to condition 2 for n =1, 2, 3 and 4. All values are normalized to the first mode per n.

frequency, the wave loading at greater depths will significantly decrease as can be seen from equation 5.16, noting that k increases for higher values of ω. The waves therefore induce a more centralised pressure field, which is more likely to equally distribute it's energy over a wider set of axial mode distributions. It should also be noted that since the linearised Bernoulli equation is used to determine the pressure on the cylinder, the position of the applied pressure does not fluctuate with the free water surface and remains at the mean sea level. While the fluctuation of the free water surface can have a minor influence on monopile's response if the wave pressure is distributed over a significant depth, this is clearly not the case for the predicted wave loading on the shell modes with a higher circumferential wavenumber. For the modes with $n > 2$, it is believed that the solution was not converged using 16 modes per n. Especially near the interface level, the stress envelopes can not be predicted accurately. Since the stresses due to the $n > 2$ modes are at least an order of magnitude lower then the stresses governing the $n = 2$ modes, they are from here on left out of the comparison. On an additional note, it was found that the modes with corresponding to $n > 2$ behave quasi-statically. Therefore, their response to the wave loading for these modes can be determined by solely the reduced stiffness matrix and the reduced wave loading in a static analysis.

It is observed that the predicted stresses, especially near the interface level, by the modes corresponding to $n = 2$ are heavily influenced by the constrained boundary at the interface level. It should therefore be noted that, if a traditional monopile with a transition piece and a grouted connection is considered, the stress envelopes may vary significantly. Additionally it is stated that, while here for each circumferential wavenumber n the stress envelopes are considered separately, fatigue of the monopile's steel is driven by the cycles of the total stress levels. Moreover, the fatigue damage is not linearly dependant on the increase in stress amplitudes. The influence of the shell deformations on the monopile's fatigue life may therefore be very different from the observed difference between the investigated stress envelopes. These envelopes can however be used to estimate how much detail in a stress analysis may be lost if one is to neglect shell deformations all together. The translation to fatigue damage is not considered in this work.

Axial stress at the inner and outer edge of the monopile's shell

In the previous, only the stress at the centre of the monopile's shell was considered. A circular cylindrical shell theory is also able to predict the stress at the outer and inner edge of the monopile's shell. These stresses vary from the stress at the centre of the shell due to the presence of the membrane moments. These membrane moments are highly sensitive to constraints and thus show a significant edge disturbance at

the interface level and around the mudline. In figure 6.8 the distribution of the axial component of the axial stress envelopes is shown at both the outer and inner edge of the monopile's shell. The highest relative contribution of the shell deformations to the axial stresses was found at the free water surface and at the interface level. At the outer edge of the monopile's shell these contributions were found to be in the order of 3% and 4% respectively, relative to the maximum axial stress, also at the monopile's inner and outer edge, as predicted using the $n = 1$ modes in the shell model.

Von Mises stress distribution
In the previous sections, only a selected portion of the stress was analysed. In figure 6.9 the distribution of the equivalent tensile stress, or von Mises stress, over the entire surface of the monopile due to condition 2 is presented. Here the von Mises stress σ_v is given by

$$\sigma_v = \sqrt{\sigma_{xx}^2 - \sigma_{xx}\sigma_{\theta\theta} + \sigma_{\theta\theta}^2 + 3\sigma_{x\theta}}, \tag{6.1}$$

where σ_{xx}, $\sigma_{\theta\theta}$ and $\sigma_{x\theta}$ were calculated based on the standard deviation of the amplitudes of the generalized coordinates. The absolute values of the normalized total von Mises stress, as calculated using all modes, can be observed in figure 6.9. The circumferential coordinate A is located at $\theta = 0$. The difference between the total von Mises stress and the von Mises stress calculated using only the $n < 2$ modes is also visualised. A maximum difference in the order of 5% was found.

6.3 Variations to the simulations

Two variations to the simulations previously presented are performed. In variation 1, a monopile with an increased diameter is considered while in variation 2 the influence of breaking waves is explored. The goal of these variations is to explore situations in which the shell deformations could have a more significant relative impact on the monopile's stress levels. Whether these variations are also realistic is rather questionable, conclusions drawn from this section should therefore be treated with great caution. The results for these simulations can be observed in appendix E.

6.3.1 Variation 1: Monopile with an increased diameter

For this variation the diameter of the monopile is increased by a factor 1.5 while the monopile is additionally slightly more thin-walled. The embedded length of

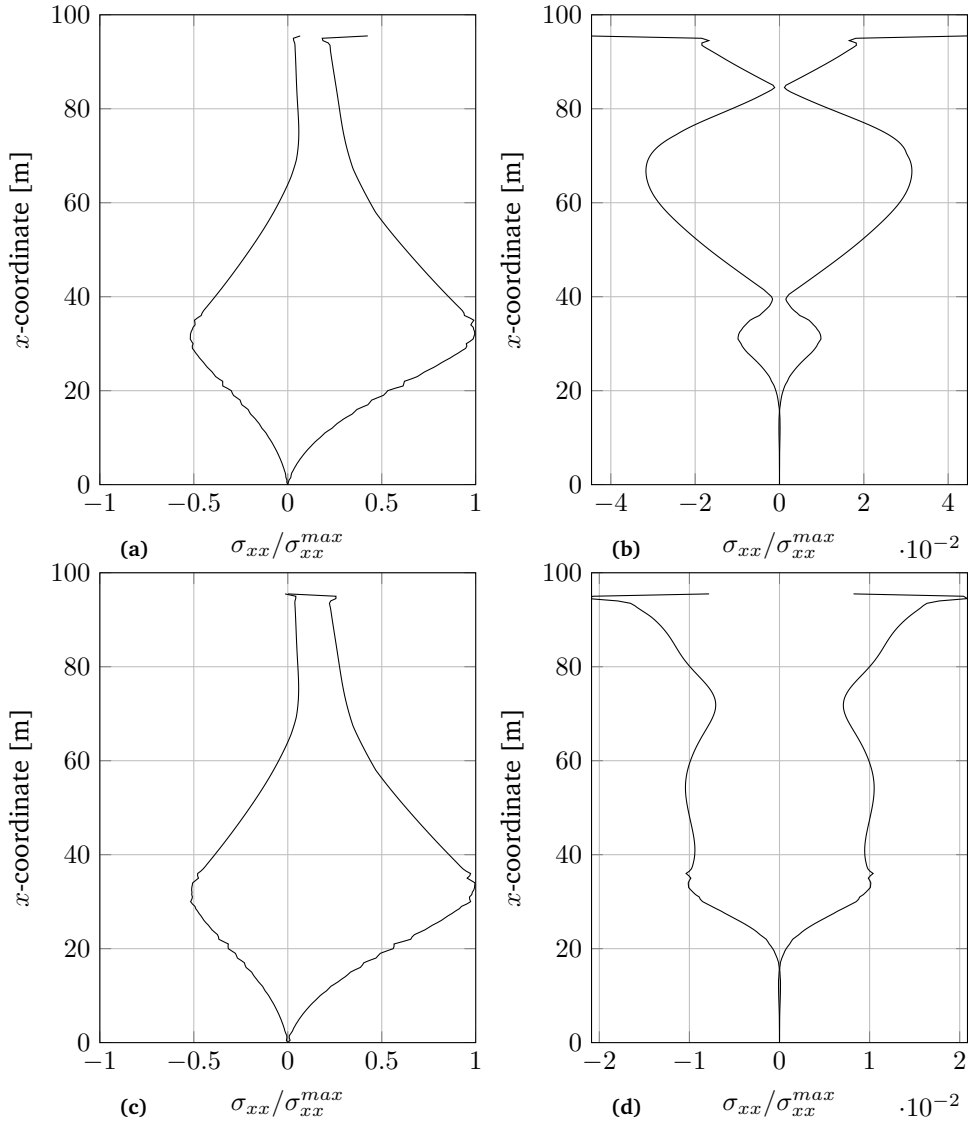

Figure 6.8: Axial stress distribution over the axial direction at circumferential coordinate A at the outer edge for $n = 1$ **(a)** and $n = 2$ **(b)**, as well as the inner edge for $n = 1$ **(c)** and $n = 2$ **(d)**. All values are calculated due to condition 2 and are normalised with respect to the largest axial stress for $n = 1$ as given by the shell model for either the inner or outer edge of the monopile's shell.

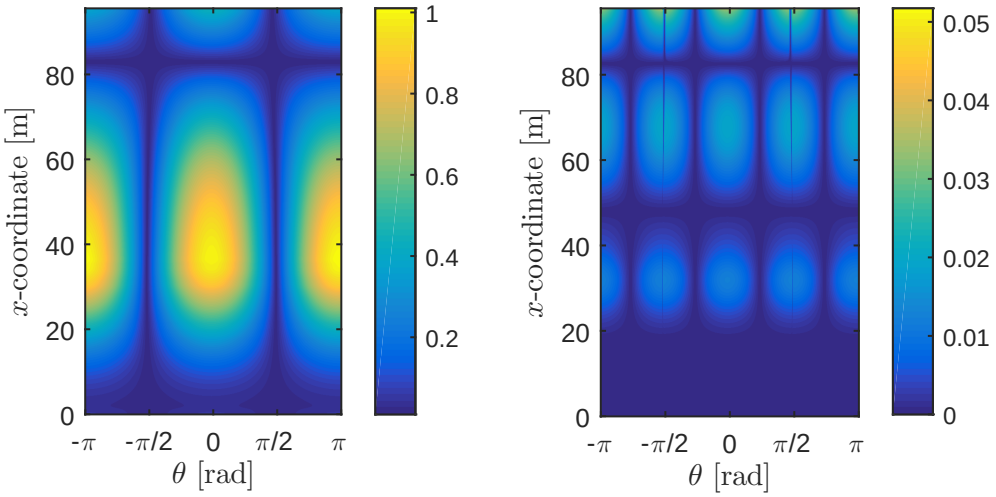

Figure 6.9: Absolute value for the total von Mises stress (left) and the difference between the total von Mises stress and the von Mises stress due to solely the modes corresponding to $n < 2$ (right). Both figures are normalized to the maximum value of the von Mises stress and are calculated for the centre of the shell due to condition 2.

the monopile within the soil remains unchanged, while the distance above the free water surface is increased such that the first eigenfrequency of the monopile's fixed-interface vibration modes governing global bending remains unchanged from the previously considered model. The monopile's density and characteristics of the elastic foundation also remain unaltered. For this variation only loading condition 2 is considered and calculations were solely performed using the shell model. For the locations under previous investigation, an increase of roughly a factor 3 can be seen in the relative contribution of shell deformations to the total axial stress. Two possible explanations for the increase in stress are given: (i) the monopile's first eigenfrequency corresponding to $n = 2$ is significantly lowered to 1.84 Hz due to the change in geometry, and (ii) the wave loading increases relative to the unchanged wind loading due to significantly larger diameter.

6.3.2 Variation 2: Monopile subjected to breaking waves

In all the previous simulations, Airy's theory was assumed to describe the incident wave field. Additionally, when the waves are translated to a force acting on the structure, they were assumed to remain harmonic. In reality, both assumptions can be considered questionable, especially if one is interested in wave loading at high frequency bands. As shown in [50], the impact of a breaking wave on a monopile structure can excite a response in a wide frequency range. Here an attempt was made to capture this behaviour, while still applying Airy's wave theory and diffraction theory to derive the resultant wave forcing. For this purpose, the wave spectrum governing condition 2 has been artificially enhanced to include an additional peak which is located around the first eigenfrequency of the modes governing $n = 2$, as can be seen in figure 6.10. The maximum value of this peak equals roughly 1/5 of the peak in the variance density spectrum corresponding to condition 2. Due to this variation no significant change in the relative contribution of shell deformations on the axial stresses was found. This is most likely explained by the way that diffraction theory distributes the wave loading over the modes governing various n, as can be observed from figure 5.9.

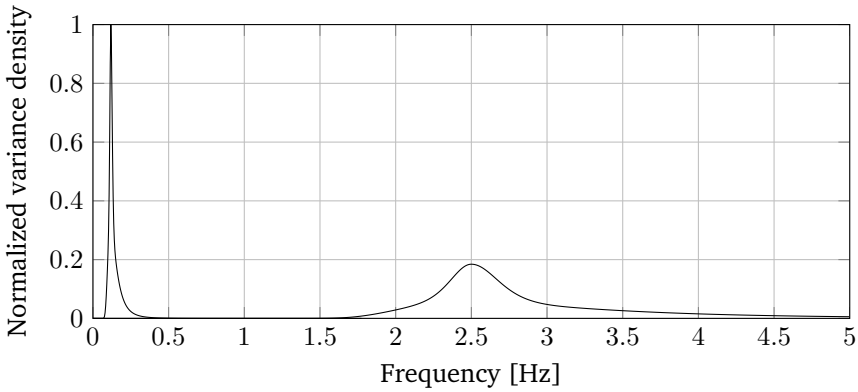

Figure 6.10: Normalized variance density spectrum of the incident waves for the variation mimicking breaking waves.

Chapter 7

Conclusions and recommendations

7.1 Introduction

A contribution towards the reduction of the levelized costs of offshore wind electricity is made. Over-dimensioning, redundant conservatism and excessive use of safety factors in the design process can be reduced by means of increasingly accurate structural models and more comprehensive knowledge on the governing structural behaviour. In this study, an advanced modelling method that accounts for shell deformations in monopile support structures is proposed with an additional focus on the implementation of the model in aero-elastic simulations. Furthermore, the effect of the more rigorous modelling method on the prediction of the monopile's internal stresses was investigated.

Two objectives for this study were defined in chapter 1, the first is given by the following.

Gain insight in the contribution of shell deformation on the internal stresses, with respect to the stresses caused by global bending, in a large diameter monopile.

The secondary objective of this study was to provide a method to incorporate the effect of the shell deformation in the assessment of the life-time loading of offshore monopile foundations. For this purpose, a model was to be developed which satisfied three criteria: (i) the model accounts for both global bending and shell deformations,

(ii) the model is computationally effective when assessing the structure's life-time loading, and (iii) the model takes into account the distribution of the wave loading and the soil reaction forces over the circumference of the monopile.

Obviously, several simplifications and assumptions were made in this study and thus we were unable to capture all involved mechanisms in their entirety. Nevertheless, it is believed that an important step towards the understanding and evaluation of shell deformation behaviour in offshore wind turbine monopile foundations is made.

7.2 Conclusions

From the time-domain simulations, several conclusions can be drawn directly related to the first research objective. Note that these conclusions are based on observations from a limited amount of simulations using a simplified and idealised model. Additionally, these conclusions relate solely to the accuracy of stress calculations, a translation to resulting fatigue damage was not made. In all cases considered, the turbine was in power production and there was assumed to be no misalignment between the wind and wave loading. The monopile under investigation had a diameter of 7.8 m.

- Stress was analysed over the entire surface of the monopile. The maximum stresses were predicted around the mudline at the location where direction of the normal to the shell's circumference is exactly opposite to the direction of the incident loading. Here the axial stresses were found to be dominant. A contribution to the axial stresses in the order of 1% due to the shell deformations was observed in the centre of the monopile's shell at this location.

- It was found that the influence of the modes corresponding to $n > 2$ on the stresses in the monopile was at least an order of magnitude lower then the influence of the modes corresponding to $n = 2$.

- Shell deformation behaviour induces a different stress distribution as opposed to global bending behaviour. This is due to the difference in the boundary condition at the interface level and a different circumferential distribution of the governing displacement functions. The form of the stress distribution therefore varies for each circumferential wavenumber n.

- Due to the presence of the membrane moments, the stress on the outer edges of the monopile's shell differs from the stress at the centre of the shell. The

maximum contribution of shell deformations to the axial stresses was analysed at the outer edge of the shell at the interface level. This contribution was in the order of 4% of the maximum axial stress at the monopile's outer edge.

- Incorporating the effect of stress in all directions, by analysing the von Mises stresses in the structure, a difference in the order of 5% between the stress due to the global bending response of the shell model and the stress due to the total response was observed in the centre of the monopile's shell.

- Following diffraction theory, the predicted loading distribution over the monopile's circumference follows a similar Fourier decomposition as the structural response of circular cylindrical shells. Waves in slightly higher frequency bands become more dominant in the loading for increasing circumferential wavenumber n. In this study it is found that these frequency bands move away from the energy peak in the JONSWAP spectrum, leading to less energy in the wave loading, for increasing n. Additionally it was found that the lowest eigenfrequencies for the first three self-balancing shell modes are significantly higher than the frequency bands in which the wave loading terms with the corresponding circumferential wavenumbers are dominant.

- The influence of the monopile's diameter has been explored. It was found that, for a monopile with a diameter that increased by a factor of 1.5, the relative contribution of shell deformations on the axial stresses in the shell increased roughly by a factor of 3. This is thought to be explained by either the lowering of the lowest eigenfrequency for the modes corresponding to $n = 2$, the increase in thin-walledness of the monopile or the increased dominance of the wave loading with respect to the wind loading.

Several additional conclusions were drawn from the other topics that were addressed in this study. These conclusions are related to the evaluation of shell deformations using the method proposed in this study.

- Using a circular cylindrical shell theory, the shell deformations of a monopile support structure can be analysed. By means of a Fourier decomposition, the monopile's shell deformation behaviour can be decoupled from its global bending response, under the assumption of a perfect cylinder.

- Flügge's theory for circular cylindrical shells and Timoshenko's theory for beams are in excellent agreement with each other with respect to the global bending response of an offshore monopile foundation. This was verified by means of a static analysis, an eigenvalue analysis, and aero-elastic simulations.

- The circumferential wavenumber method was unable to derive true equivalent soil-structure interaction characteristics from the FEM model of the soil. While the obtained elastic foundation was considered sufficient for this study, representation of the particular soil under investigation was unsuccessful.
- The superelement methods were able to provide a coupling between numerical and analytical modelling. Model reduction techniques can be used to simplify analytical problems or reduce the degrees of freedom of discrete systems, the application follows the same procedures in both situations.

7.3 Recommendations

In this study two strategies related to the analysis of shell deformations in monopile support structures were applied. On the one hand, the analysis of shell deformation behaviour was integrated in a numerical aero-elastic code which is able to perform time-domain simulations of the entire wind turbine structure in a wide variety of load cases. On the other hand, the shell deformation behaviour was isolated from the global bending behaviour of the monopile and decoupled from all the dynamic effects above the interface level. The incorporation of both strategies may seem contradicting at first glance. However, it is believed that valuable insight was obtained in a wide variety of relevant mechanisms due to the broad scope of this study. For the further development of knowledge on shell deformation behaviour in large diameter offshore monopile's two paths are proposed. It is believed that both paths can be explored independently of each other.

- The first path focusses on a more detailed modelling of the monopile and fluid-structure interaction. CFD simulations can aid in the realistic assessment of the coupling between the fluid domain and the monopile, a focus on the added mass for shell deformation is expected to be of importance. The assessment of wave loading in higher frequency bands, such as the analysis of breaking waves against the structure, can also be performed in more detail. Inhomogeneities to the here considered ideal cylinder can also be introduced if a FEM model of the monopile is used. These can be appurtenances, a transition piece, or a monopile of varying diameter. The greater level of detail allows for a more proper assessment of edge disturbances, which can be significant in the calculation of resulting stresses in a shell-like structure. Additionally, the monopile can now be directly coupled to more advanced soil models which incorporate non-local soil-structure interaction characteristics. For this assessment, the coupling with the tower can be omitted. Instead, a time-domain simulation

using a simpler model can be used to obtain equivalent lateral reaction forces and overturning moments at the interface level, which can be used as input for the high detail monopile model. The coupling with an aero-elastic code hereby becomes irrelevant.

- In the second path, attention is paid to the interaction with the shell deformation behaviour and the dynamics of the entire turbine. The resulting loading on the self-balancing shell modes due to aero- and controller dynamics can be incorporated. Additionally, the effect of coupling between eigenmodes governing global bending and eigenmodes governing shell deformation behaviour can be analysed. This was neglected in this study under the assumption of an ideal cylinder. Due to the significant presence of the wind loading in this assessment, it is advisable that time-domain simulations should be performed for a wide variety of load cases. For this purpose, a similar semi-analytical integrated model, as presented here, can be developed. The model is to be augmented such that it can incorporate the previously mentioned phenomena. If the dynamic behaviour of the monopile is analysed in the modal domain, which may be an effective method from a computational point of view, the implementation of soil-structure interaction by means of a modal expansion can additionally be explored.

Other, more general, recommendations can also be made. Perhaps the most obvious one is the validation of all assumptions made during this study. The ones considered most imported are mentioned within the various recommendations in this section. Other recommendations that are not captured in the previous statements are given below.

Model validation using measurements. In this study, the predicted shell deformation behaviour is purely based on a theoretical and idealised structural model. Experimental validation of the eigenmodes and eigenfrequencies governing $n > 1$ can provide insight in the correctness of the presented calculations.

Generalising the results and translation to fatigue damage. Generalising the results obtained in this study by means of an extended amount of simulations for a wide variety of load cases may prove valuable. Ideally, the translation to fatigue damage at governing design location should also be made. The incorporation of statistics thus becomes important.

Quasi-static estimation of shell deformations. In this study it was found that the response of the shell modes corresponding to $n > 2$ to the wave loading can be treated quasi-statically. It can be investigated for which situations this remains true.

Appendix A

Translation from the discrete spring stiffness profiles to a distributed elastic foundation

This appendix is a direct extension of chapter 3. It is shown how the discrete spring stiffness profiles, as obtained using the circumferential wavenumber method and the mode shape method, can be translated to a distributed elastic foundation. This is done in two steps. First, it is shown how the discrete nodal reaction forces can be distributed over the axial and circumferential direction of S_{MP}. Second, it is shown how the same formulations can be used to directly translate the obtained discrete spring stiffness profiles into a distributed elastic foundation.

A.1 Distributing the discrete forces over a surface

Distribution of the reaction forces in the circumferential direction

It was found that the discrete reaction forces of the soil in the FEM model can be described by

$$F^q_{nx} = \hat{F}_{nx}(x)\cos(n\theta), \tag{A.1a}$$

$$F^q_{n\theta} = \hat{F}_{n\theta}(x)\sin(n\theta), \tag{A.1b}$$

$$F^q_{nz} = \hat{F}_{nz}(x)\cos(n\theta), \tag{A.1c}$$

where q denotes the number of a node, $F_{ni}(x)$ is the amplitude of the reaction forces at x, which is equal to the reaction force at $\theta = 0$ for $i = x$ or $i = z$, and is equal to the reaction force at $\theta = \frac{\pi}{2}$ for $i = \theta$. The translation to a distribution of the forces along the circumference of S_{MP} is given by

$$F_{nx}(x,\theta) = \tilde{F}_{nx}(x)\cos(n\theta), \tag{A.2a}$$

$$F_{n\theta}(x,\theta) = \tilde{F}_{n\theta}(x)\sin(n\theta), \tag{A.2b}$$

$$F_{nz}(x,\theta) = \tilde{F}_{nz}(x)\cos(n\theta). \tag{A.2c}$$

Where for $j = x$, θ and z

$$\tilde{F}_{nj} = \alpha_n \hat{F}_{nj}. \tag{A.3}$$

Here α_n corrects for the discreteness in the circumferential direction in the FEM model. α_n can be determined using

$$\int_{\theta_1}^{\theta_2} F_{nj}(x,\theta) = \hat{F}_{nj}(x), \tag{A.4}$$

with

$$\theta_1 = -\frac{2\pi}{2N}, \qquad \theta_2 = \frac{2\pi}{2N}, \qquad \text{if} \quad i = x, z, \tag{A.5a}$$

$$\theta_1 = -\frac{2\pi}{2N} + \frac{\pi}{2}, \qquad \theta_2 = \frac{2\pi}{2N} + \frac{\pi}{2}, \qquad \text{if} \quad i = \theta, \tag{A.5b}$$

where N is the number of nodes on S_{MP} in the horizontal plane. Resulting from this, α_n is given by

$$\alpha_n = a\frac{\cos\left(\frac{\pi}{2N}\right)\sin\left(\frac{\pi}{2N}\right)N + \pi}{2N}, \qquad \text{if} \quad n = 1, \tag{A.6a}$$

$$\alpha_n = a\frac{(n+1)\sin\left(\pi\frac{n-1}{2N}\right)n + (n-1)\sin\left(\pi\frac{n+1}{2N}\right)}{(n-1)(n+1)}, \qquad \text{if} \quad n \neq 1. \tag{A.6b}$$

Distribution of the reaction forces in the axial direction

In this section it is assumed that between any two successive nodes on any vertical line in S_{MP} the force distribution is constant. Consider a beam as visualized in figure A.1. The beam consists of two segments. Each segment has a length, denoted by L_s, and is subjected to a constant distributed load, denoted with q_s. In the translation to a discrete system, such as a finite element description with beam

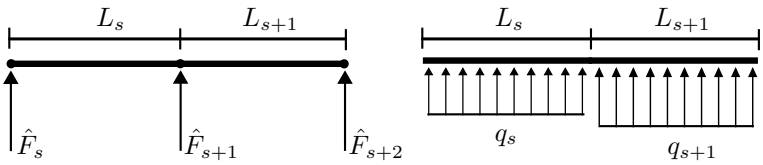

Figure A.1: A schematization of a discrete beam (left) and a continuous beam (right).

elements, the distributed force is lumped to the nodes of the beam. This can be done by integrating the loading over the shape functions of the beam. However, when the loading is constant between each node, the forces at each node can alternately be found as

$$\hat{F}_s = \frac{q_s}{2L_s}, \tag{A.7a}$$

$$\hat{F}_{s+1} = \frac{q_s}{2L_s} + \frac{q_{s+1}}{2L_{s+1}}, \tag{A.7b}$$

$$\hat{F}_{s+2} = \frac{q_{s+1}}{2L_{s+1}}. \tag{A.7c}$$

If a beam with more then three nodes is considered, a relation similar to A.7b can be added for each additional internal node. If the problem is reversed and the translation has to be made from a discrete beam to a continuous beam, the values for q_i and q_{i+1} can be found by

$$q_s = 2\hat{F}_s L_s, \tag{A.8a}$$

$$q_{s+1} = 2\hat{F}_{s+1} L_{s+1} - 2\hat{F}_s L_{s+1}. \tag{A.8b}$$

Again, if a beam with more then three nodes is considered, a relation similar to A.8b can be added for each additional internal node. Using the relations similar to A.8 the reaction forces can be transformed to a distribution of the forces over the axial direction.

A.2 Direct translation from a discrete spring stiffness profile to a distributed elastic foundation

In section 3.2.1 it was shown how equivalent discrete spring stiffness constants at the locations of N_{MP}, can be determined as

$$\tilde{k}_{ij}^q = F_i^q / u_j^q \tag{A.9}$$

where $\tilde{k}_{ij}^{q}$ is the stiffness constant of an elastic spring, exerting a force F_i upon node $q \in N_{MP}$ in direction i due to a displacement u_j of q in direction j.

In the following it is shown how the discrete springs are translated into distributions which are described with harmonic functions over the circumferential direction of S_{MP} and stepwise functions over the axial direction of S_{MP}. This is done by taking the spring stiffness constants at a single vertical line in S_{MP}. For $i = x$, z the line at $\theta = 0$ has to be taken, while if $i = \theta$, the line at $\theta = \frac{\pi}{2}$ has to be taken. These lines represent the maxima of the spring stiffness constants. If a segment is defined between each node on the vertical line, the characteristics of the elastic foundation on each segment can be defined by

$$\begin{bmatrix} K_1^{(s)}\{u,v,w\} \\ K_2^{(s)}\{u,v,w\} \\ K_3^{(s)}\{u,v,w\} \end{bmatrix} = \begin{bmatrix} k_{nxx}^{(s)} & k_{nx\theta}^{(s)} \frac{1}{n} \frac{\partial}{\partial \theta} & k_{nxz}^{(s)} \\ -k_{n\theta x}^{(s)} \frac{1}{n} \frac{\partial}{\partial \theta} & k_{n\theta\theta}^{(s)} & -k_{n\theta z}^{(s)} \frac{1}{n} \frac{\partial}{\partial \theta} \\ k_{nzx}^{(s)} & k_{nz\theta}^{(s)} \frac{1}{n} \frac{\partial}{\partial \theta} & k_{nzz}^{(s)} \end{bmatrix} \begin{bmatrix} u^{(s)}(x,\theta) \\ v^{(s)}(x,\theta) \\ w^{(s)}(x,\theta) \end{bmatrix}, \tag{A.10}$$

where, for the first and successive segments s

$$k_{nij}^{(1)} = \alpha_n 2 \tilde{k}_{nij}^{(1)} L_1, \tag{A.11a}$$

$$k_{nij}^{(s)} = \alpha_n 2 L_s \left(\tilde{k}_{nij}^{(s)} - \tilde{k}_{nij}^{(s-1)} \right). \tag{A.11b}$$

Appendix B

Calculation of matrix products

This appendix shows how the calculation of matrix products can be performed per entry of the resulting matrix. Let $\boldsymbol{A}$, $\boldsymbol{B}$ and $\boldsymbol{C}$ be matrices of sizes $n \times n$, $n \times m$ and $m \times n$ respectively. If

$$\boldsymbol{G} = \boldsymbol{A}\boldsymbol{B}, \tag{B.1}$$

then $\boldsymbol{G}$ is thus of size $n \times m$. The individual entries $\boldsymbol{G}_{i,j}$ of $\boldsymbol{G}$ can alternatively be found as

$$\boldsymbol{G}_{i,j} = \sum_{k=1}^{n} \boldsymbol{A}_{i,k}\boldsymbol{B}_{k,j}, \tag{B.2}$$

for $i = 1, 2, ..., n$ and $j = 1, 2, ..., m$. Here i denoted a row number while j denotes a column number. Similarly for

$$\boldsymbol{H} = \boldsymbol{C}\boldsymbol{A}\boldsymbol{B} \tag{B.3}$$

the individual entries $\boldsymbol{H}_{i,j}$ of $\boldsymbol{H}$ can be calculated from

$$\boldsymbol{H}_{i,j} = \sum_{l=1}^{n} \boldsymbol{C}_{i,l} \sum_{k=1}^{n} \boldsymbol{M}_{l,k}\boldsymbol{B}_{k,j}, \tag{B.4}$$

where now $i = 1, 2, ..., m$ and $j = 1, 2, ..., m$.

This method was applied in the derivation of the reduced matrices for the beam and shell model. These reduced matrices were a result of multiplication of matrices which consisted of functions rather then numerical values. Furthermore, each entry in the resulting reduced matrix was to be integrated over one or several coordinates. The entry wise calculation procedure as present above allowed to identify which

functions were present in each integral, which was beneficial for the calculation process.

Appendix C

Eigenfrequencies of the fixed-interface vibration modes

Beam	Shell $n = 1$	Shell $n = 2$	Shell $n = 3$	Shell $n = 4$
3.5694	3.5707	2.3733	5.0982	9.6425
8.2893	8.2949	4.4853	5.5516	9.7954
13.066	13.087	7.7874	6.6739	10.154
16.056	16.066	11.808	8.5411	10.820
19.509	19.532	16.233	11.027	11.865
24.066	24.092	20.797	13.956	13.304
29.555	29.509	25.221	17.177	15.108
35.275	35.043	28.716	20.564	17.215
41.107	40.516	30.332	24.017	19.556
47.013	45.861	32.635	27.456	22.063
52.905	50.947	34.057	30.820	24.676
58.722	55.705	36.314	34.080	27.342
64.315	60.090	39.099	37.205	30.020
65.165	62.992	42.036	40.066	32.682
69.297	64.141	45.051	41.125	35.311
70.617	66.748	48.175	42.676	37.899

Appendix D

Modal Assurance Criterion for the fixed-interface vibration modes

In this appendix the Modal Assurance Criterion is calculated for the fixed-interface vibration modes in the shell model. The Modal Assurance Criterion is used for the comparison of two eigenvectors ϕ_a and ϕ_b as

$$\text{MAC} = \frac{\left(\phi_a^T \phi_b\right)^2}{\left(\phi_a^T \phi_a\right)\left(\phi_b^T \phi_b\right)}. \tag{D.1}$$

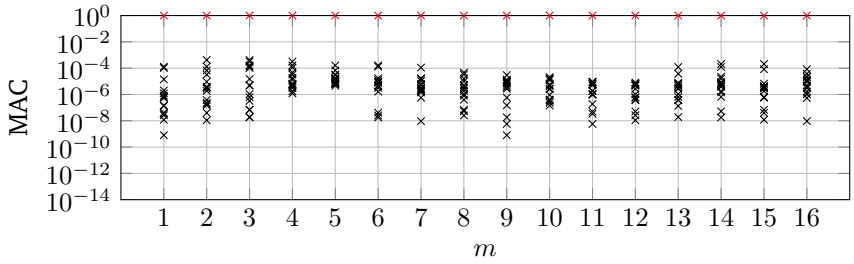

Figure D.1: MAC for the fixed-interface vibration modes governing $n = 1$.

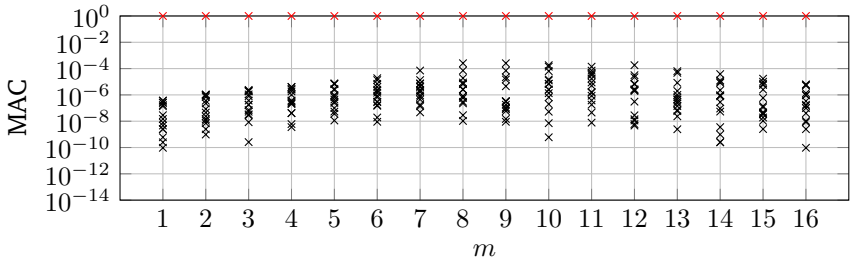

Figure D.2: MAC for the fixed-interface vibration modes governing $n = 2$.

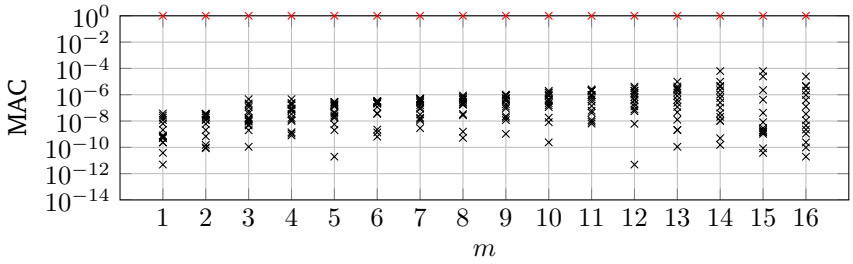

Figure D.3: MAC for the fixed-interface vibration modes governing $n = 3$.

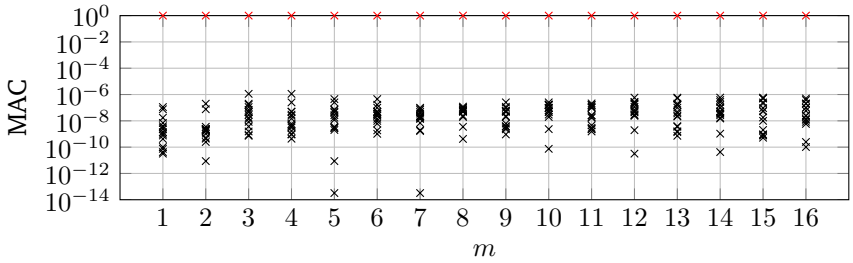

Figure D.4: MAC for the fixed-interface vibration modes governing $n = 4$.

Appendix E

Addtional results from the time-domain simulations

This appendix is a direct extension of chapter 6. Figures E.1 and E.2 present the time signals for the axial stress at the mudline at circumferential coordinate A while the stress envelopes of the axial stress at circumferential coordinate A are additionally shown. The data corresponds to simulations according to variation 1 and 2, as described in section 6.3.

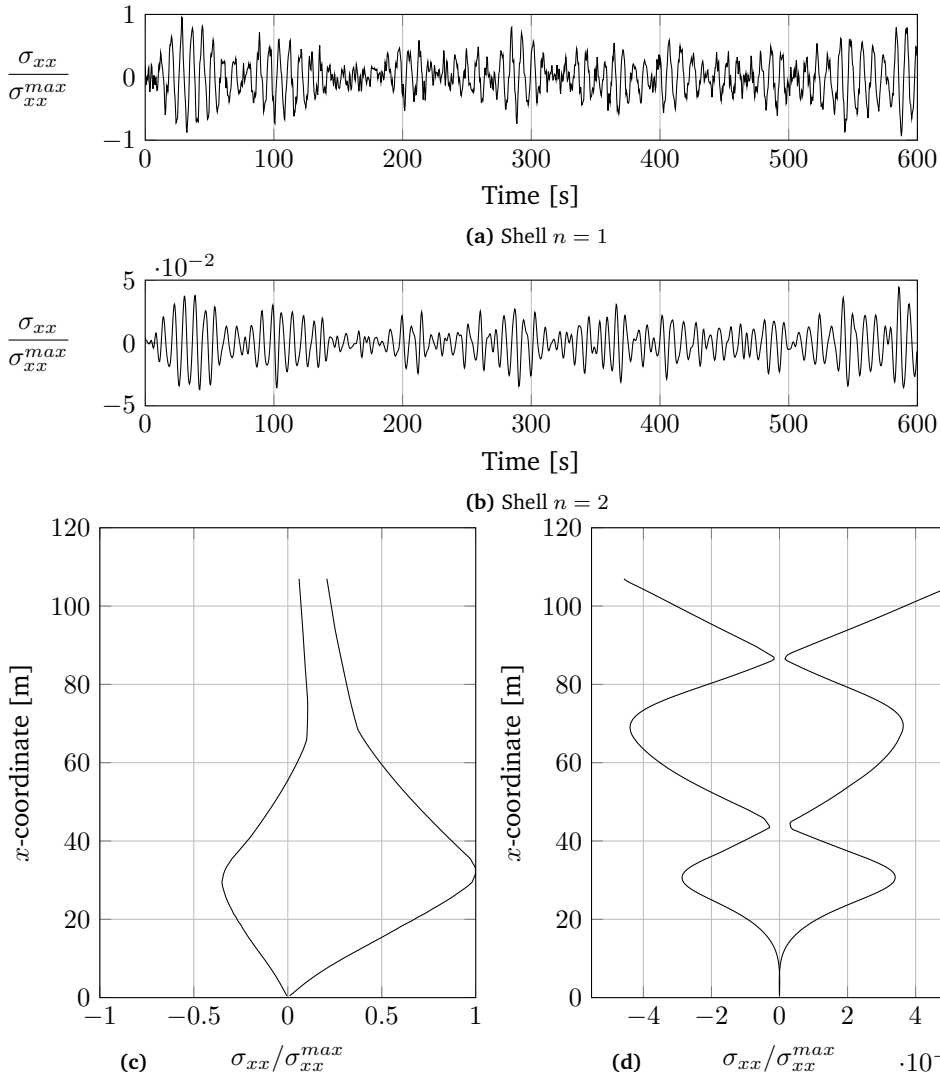

(a) Shell $n = 1$

(b) Shell $n = 2$

(c)

(d)

Figure E.1: Time signals of the shell model's predictions of the axial stress for $n = 1$ **(a)** and $n = 2$ **(b)**. Envelopes of the axial stress distribution in the axial direction for $n = 1$ **(c)** and $n = 2$ **(d)** . All values are calculated for the increased diameter pile at circumferential coordinate A in the centre of the monopile's shell and are normalised with respect to the maximum axial stress for $n = 1$.

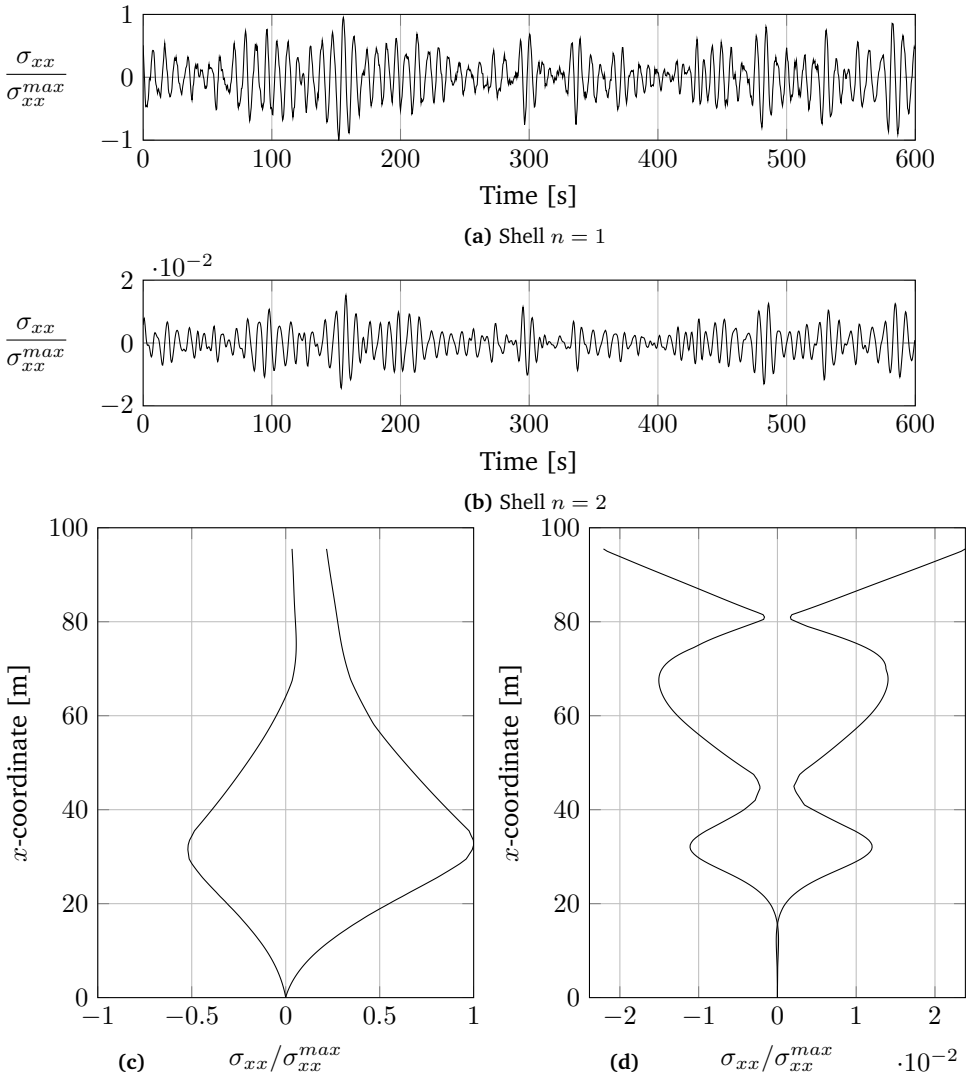

(a) Shell $n = 1$

(b) Shell $n = 2$

(c)

(d)

Figure E.2: Time signals of the shell model's predictions of the axial stress for $n = 1$ **(a)** and $n = 2$ **(b)**. Envelopes of the axial stress distribution in the axial direction for $n = 1$ **(c)** and $n = 2$ **(d)**. All values are calculated for the breaking waves variation at circumferential coordinate A in the centre of the monopile's shell and are normalised with respect to the maximum axial stress for $n = 1$.

Bibliography

[1] Sociaal-Economische Raad. Energieakkoord voor duurzame groei. Technical report, 2013.

[2] European Wind Energy Association. Deep water, the next step for offshore wind energy. Technical report, 2013.

[3] EEW Special Pipe Constructions GmbH. XL monopiles up to 120 m length, 10 m diameter and 1.500 ton weight are coming ! *Wind-Kraft, German Offshore Journal*, 2014.

[4] R. Engels. Superelement modeling of offshore wind turbine support structures. Master thesis, University of Twente, 2013.

[5] Det Norske Veritas AS. *Offshore Standard DNV-OS-J101, Design of Offshore Wind Turbine Structures*, 2013.

[6] S. P. Timoshenko. On the correction for shear of the differential equation for transverse vibrations of prismatic bars. *Philosophical Magazine*, 41(245):744–746, 1921.

[7] S. P. Timoshenko. On the transverse vibrations of bars of uniform cross-section. *Philosophical Magazine*, 43(253):125–131, 1922.

[8] A. Simone. An introduction to the analysis of slender structures. Lecture notes, 2011.

[9] G. R. Cowper. The shear coefficient in Timoshenko's beam theory. *Journal of Applied Mechanics*, 33(2):335–340, 1996.

[10] W. Leissa. *Vibration of shells*. The Ohio State University, 2nd edition, 1973.

[11] A. E. H. Love. *A treatise on the mathematical theory of elasticity*. Cambridge university press, 1st edition, 1892.

[12] W. Flügge. *Stresses in Shells*. Springer-Verlag, 2nd edition, 1973.

[13] J. Blauwendraad and J. H. Hoefakker. *Structural Shell Analysis, Understanding and Application*, volume 200 of *Solid Mechanics and Its Applications*. Springer, 2014.

[14] W. Soedel. *Vibrations of shells and plates*. Marcel Dekker, 2nd edition, 1993.

[15] P. Farshidianfar, P. Oliazadeh, and M. H. Farshidianfar. Exact analysis of resonance frequencies of simply supported cylindrical shells. *International Journal of mechanical, Aerospace, Industrial and Mechatronics Engineering*, 7(4):335–341, 2013.

[16] A. Ludwig and R. Krieg. An analytical quasi-exact method for calculating eigenvibrations of thin circular cylindrical shells. *Journal of Sound and Vibration*, 74(2):155–174, 1981.

[17] J. Callahan and H. Baruh. A closed-form solution procedure for circular cylindrical shell vibrations. *International Journal of Solids and Structures*, 36:2973–3013, 1999.

[18] M. Zehsaz, M. H. Sadeghi, and A. Ziaei Asl. Dynamics response of railway under a moving load. *Journal of Applied Sciences*, 9(8):1474–1481, 2009.

[19] S. Kramer. Soil-structure interaction: basic concepts. University seminar.

[20] S. P. H. Soerensen, L. B. Ibsen, and A. H. Augustesen. Effects of diameter on initial stiffness of p-y curves for large-diameter piles in sand, numerical methods in geotechnical engineering. In *Proc. of the 7th European Conference, Trondheim/Norway*, volume 2, 2010.

[21] W. G. Versteijlen, K.N. van Dalen, and A.V. Metrikine. *UNDER REVIEW* prediction of the fundamental natural frequency of offshore wind turbines based on in-situ measured small-strain soil stiffness and 3d modelling. *Engineering Structures*, 2015.

[22] A. Tsouvalas and A. V. Metrikine. A three-dimensional vibroacoustic model for the prediction of underwater noise from offshore pile driving. *Journal of Sound and Vibration*, 333(8):2283–2311, 2013.

[23] M. Caresta and N. Kessissoglou. Free vibrational characteristics of isotropic coupled cylindrical-conical shells. *Journal of Sound and Vibration*, 329:733–751, 2010.

[24] Y. Qu, H. Hua, and G. Meng. Vibro-acoustic analysis of coupled spherical-cylindrical-spherical shells stiffened by ring and stringer reinforcements. *Journal of Sound and Vibration*, 355:345–359, 2015.

[25] P. L .C. van der Valk. *Coupled simulations of wind turbines and offshore support structures. Strategies based on the dynamic substructuring paradigm*. PhD thesis, Delft University of Technology, 2014.

[26] R. R. Craig and M. C. C. Bampton. Coupling of substructures for dynamic analyses. *AIAA Journal*, 6(7):1313–1319, 1968.

[27] R. J. Guyan. Reduction of stiffness and mass matrices. *AIAA Journal*, 3(2):380–380, 1965.

[28] B. Irons. Structural eigenvalue problems - elimination of unwated variables. *AIAA Journal*, 3(5):961–962, 1965.

[29] D. de Klerk, D. J. Rixen, and S. N. Voormeeren. General framework for dynamic substructuring: history, review, and classification of techniques. *AIAA Journal*, 46(5):1169–1181, 2008.

[30] W. C. Hurty. Vibrations of structural systems by component mode synthesis. *Journal of the Engineering Mechanics Division*, 86(4):51–71, 1960.

[31] W. C. Hurty. Dynamic analysis of structural systems using component modes. *AIAA Journal*, 3(4):678–685, 1965.

[32] J. H. Vugts. The offshore wave and current environment and hydrodynamic loading. Technical report, Delft University of Technology, 2002.

[33] L. H. Holthuijsen. *Waves in oceanic and coastal waters*. Cambridge university press, 2007.

[34] M. St. Denis and W. J. Pierson. On the motions of ships in confused seas. Technical Report 61, SNAME, 1953.

[35] A. C. W. M. Vrouwenvelder. Random vibrations: CT5145. Lecture notes, 2004.

[36] K. Hasselman. measurements of wind-wave growth and swell decay during the Joint North Sea Wave Project (JONSWAP). *Deutsches Hydrographisches Zeitschrift*, Reihe A (8^0)(12), 1973.

[37] W. J. Pierson and L. Moskowitz. A proposed spectral form for fully developed wind seas based on the similarity theory of S. A. Kitaigorodskii. *Journal of Geophysical Research*, 69(24):5181–5190, 1964.

[38] M. K. Ochi and E. N. Hubble. Six-parameter wave spectra. In *Proc 15th Coastal Engineering Conference*, volume 15, pages 301–328, 1976.

[39] K. Torsethaugen. Model for a doubly peaked wave spectrum. Sintef report stf22 a96204, 1996.

[40] G. B. Airy. Tides and waves. In *Encyclopaedia Metropolitana*, 1845.

[41] R. C. MacCamy and R. A. Fuchs. Wave forces on piles: A diffraction theory. Technical Report Technical memorandum 69, Beach erosion board corps of engineers, 1954.

[42] T. H. Havelock. The pressure of water waves upon a fixed obstacle. *Proceedings of the Royal Society of London*, 175(A):409–421, 1940.

[43] Marit Irene Kvittem. *Modelling and response analysis for fatigue design of a semi-submersible wind turbine*. PhD thesis, NTNU, Norway, 2014.

[44] Tony Burton, David Sharpe, Nick Jenkins, and Ervin Bossanyi. *Wind energy handbook*. John Wiley & Sons, 2001.

[45] J. R. Morison, M. P. O'Brien, J. W. Johnson, and S. A. Schaaf. The force exerted by surface waves on piles. *Petroleum transactions, AIME*, 189:149–154, 1950.

[46] M. Rahman, H. Mousavizadegan, and D. Bhatta. Nonlinear diffraction of water waves: a classical perturbation method. In M. Rahman and C. A. Brebbia, editors, *Advances in fluid mechanics IX*, volume 74 of *WIT Transactions on engineering sciences*, pages 3–13, 2012.

[47] J. M. J. Journée and W. W. Massie. Offshore hydromechanics. Lecture notes, 2001.

[48] M. H. Patel. *Dynamics of offshore structures*. Butterworths, 1998.

[49] F. Bérot and B. Peseux. Vibro-acoustic behaviour of submerged cylindrical shells: analytical formulation and nummerical model. *Journal of Fluids and Structures*, 12:959–1003, 1998.

[50] Zang J., Taylor P. H., Tello M., Morgan G., Stringer R., Orszaghova J., and Grice J. Steep wave and breaking wave impact on offshore wind turbine foundations - Ringing re-visited. Technical report.


SIEMENS